

# Laser Radar Tomography: The Effects of Speckle

by

Bradley Thomas Binder

B.S. Electrical Engineering, University of Nebraska  
(1983)

S.M. Electrical Engineering, Massachusetts Institute of Technology  
(1987)

E.E., Massachusetts Institute of Technology  
(1987)

Submitted to the Department of Electrical Engineering and Computer Science  
in partial fulfillment of the requirements for the Degree of

Doctor of Philosophy

at the Massachusetts Institute of Technology

August 1991

© Bradley T. Binder, 1991

Signature of Author \_\_\_\_\_  
Department of Electrical Engineering and Computer Science  
August 29, 1991

Certified by \_\_\_\_\_  
Professor Jeffrey H. Shapiro  
Thesis Supervisor

Accepted by \_\_\_\_\_  
Professor Campbell L. Searle  
Chair, Department Committee on Graduate Students

MASSACHUSETTS INSTITUTE  
OF TECHNOLOGY

NOV 04 1991

LIBRARIES

ARCHIVES

# **Laser Radar Tomography: The Effects of Speckle**

by

**Bradley Thomas Binder**

Submitted to the Department of Electrical Engineering and Computer Science  
on August 29, 1991 in partial fulfillment of the requirements for the  
Degree of Doctor of Philosophy in Electrical Engineering

## **Abstract**

Recent experiments have used tomographic techniques to reconstruct images of rotating targets from either range-resolved or Doppler-resolved laser radar data. In the range-time-intensity (RTI) imaging approach, a series of  $N$  range projections of the target reflectivity is collected throughout the target rotation period by direct detection of a short-duration laser illumination pulse. In the companion Doppler-time-intensity imaging (DTI) technique, a set of  $N$  Doppler-resolved target reflectivity projections is recorded over the target rotation by an optical heterodyne laser radar receiver. The resulting two-dimensional image formed from either set of  $N$  projections is corrupted by detector shot-noise and optical speckle effects.

This thesis theoretically models and analyzes the statistical performance of both RTI and DTI imaging systems. Performance predictions are made in terms of radar-target geometry, electromagnetic propagation, target characteristics, coherent or incoherent detection, post-detection processing and tomographic image reconstruction. The derived image signal-to-noise ratios (SNR's) and point spread functions (PSF's) are used to compare the two approaches to existing experimental data.

Thesis Supervisor: Professor Jeffrey H. Shapiro

Title: Professor of Electrical Engineering

## Acknowledgements

The completion of this dissertation would not be possible without the help of many people. I am very grateful to my research advisor, Professor Jeffrey Shapiro, for his keen insight, patience and encouragement during the course of this research. I also appreciate the suggestions and viewpoints offered by the two other members of my Ph.D. committee, Professor Alan Willsky of the M.I.T. Dept. of Electrical Engineering and Computer Science and Dr. Alan Kachelmyer of the Laser Radar Measurements Group at the M.I.T. Lincoln Laboratory. I thank Drs. William Keicher, Brian Edwards and Richard Marino of the M.I.T. Lincoln Laboratory Laser Radar Measurements Group for their expertise and gracious support.

I am thankful for the friends I have made while attending M.I.T. The support and friendship of Tom Green and Robert Mentle of the Optical Propagation and Communication Group and David Nordquist and Mike Reiley of Lincoln Laboratory made my schooling much more special. I am also very grateful for the encouragement and prayers of my friends at the Waltham Evangelical Free Church.

Finally, I thank my fiancée, Joellen DiRusso, for her commitment, love and understanding.

This thesis was sponsored by the Department of the Navy. This support is appreciated.

*To my parents, Robert and Claudette Binder*

# Contents

<b>Abstract</b>	<b>2</b>
<b>Acknowledgements</b>	<b>3</b>
<b>1 Introduction</b>	<b>9</b>
1.1 Optical Radar . . . . .	12
1.2 Research Program . . . . .	14
<b>2 The Mathematics of Tomography</b>	<b>21</b>
2.1 The Radon Transform . . . . .	23
2.2 Backprojection Image Reconstruction . . . . .	26
2.3 The Inverse Radon Transform . . . . .	26
2.4 Sampling and Resolution . . . . .	27
2.5 Reconstruction Example . . . . .	29
<b>3 Two-Dimensional Speckle Field Tomography</b>	<b>33</b>
3.1 Tomographic Speckle Model . . . . .	33
3.2 Projection Statistics . . . . .	37
3.3 Backprojection Image Statistics . . . . .	42
3.4 Backprojection Image Signal-to-Noise Ratio . . . . .	46
3.5 Filtered Backprojection Image Statistics . . . . .	50
3.6 Filtered Backprojection Signal-to-Noise Ratio . . . . .	53
<b>4 RTI Tomographic Imaging Performance</b>	<b>59</b>
4.1 RTI Tomographic Imaging Model . . . . .	61
4.1.1 Transmitter Beam Propagation . . . . .	61
4.1.2 Target Characterization . . . . .	66
4.1.3 Direct Detection . . . . .	73
4.1.4 Post-Detection Image Processing . . . . .	75
4.2 Projection Statistics . . . . .	76
4.3 Reconstructed Image Performance . . . . .	84

<b>5</b>	<b>DTI Tomographic Imaging Performance</b>	<b>95</b>
5.1	DTI Tomographic Imaging Model . . . . .	96
5.1.1	Transmitter Beam Propagation . . . . .	96
5.1.2	Target Characterization . . . . .	98
5.1.3	Heterodyne Mixing Integral . . . . .	99
5.1.4	Post-Detection Image Processing . . . . .	102
5.2	Projection Statistics . . . . .	104
5.3	Reconstructed Image Performance . . . . .	111
<b>6</b>	<b>Comparison with Experimental Results</b>	<b>117</b>
<b>7</b>	<b>Conclusions</b>	<b>121</b>
<b>A</b>	<b>Appendix</b>	<b>125</b>
<b>B</b>	<b>Appendix</b>	<b>129</b>
B.1	RTI Mean Projection Formulation . . . . .	129
B.2	RTI Second Moment Projection Derivations . . . . .	134
B.2.1	Projection Covariance . . . . .	135
B.2.2	Filtered RTI Projection Variance . . . . .	146
<b>C</b>	<b>Appendix</b>	<b>151</b>
C.1	Heterodyne Signal Correlation . . . . .	151
C.2	DTI Projection First Moment Derivation . . . . .	155
C.3	DTI Second Moment Projection Derivations . . . . .	158
C.3.1	Projection Covariance . . . . .	159
C.3.2	Filtered DTI Projection Variance . . . . .	163
	<b>Bibliography</b>	<b>165</b>
	<b>Biographical Note</b>	<b>170</b>

# List of Figures

1.1	Radar Operation . . . . .	10
1.2	Optical Heterodyne Detection . . . . .	13
1.3	Laser Radar Imaging Example . . . . .	15
1.4	A Range–Time–Intensity Imaging Example . . . . .	17
2.1	Computerized Tomography Geometry. . . . .	22
2.2	Phantom Reconstructions: (a) Original Phantom, (b) Backprojection Reconstruction, (c) Filtered Backprojection Reconstruction. . . . .	30
3.1	Two–Dimensional Speckle Tomography Geometry. . . . .	36
3.2	Covariance Calculation Geometry. . . . .	40
3.3	Normalized Mean Backprojection Image PSF, $G_{bp}(x, y : 4)$ . . . . .	43
3.4	Backprojection SNR Performance . . . . .	49
3.5	Filtered Backprojection Mean Image PSF (a) $g_f(r)$ , (b) $G_{fbp}(x, y : 4)$ . . . . .	52
3.6	Filtered Backprojection SNR Performance . . . . .	55
3.7	SNR Performance Comparison . . . . .	56
4.1	Laser Radar RTI Imaging Model Geometry . . . . .	62
4.2	Fraunhofer Diffraction Formula Geometry . . . . .	64
4.3	Photodetector Model . . . . .	74
4.4	(a) Construction of the Orthographic Projection of a Sphere (b) Normal Orthographic Projection of the Globe (c) Transverse Orthographic Projection of the Globe . . . . .	86
4.5	(a) PSF Reconstruction for $N = 144$ Projections. (b) PSF Orientation. . . . .	90
5.1	Laser Radar DTI Imaging Model Geometry . . . . .	97
5.2	Post–Detection Image Processing . . . . .	103
5.3	(a) PSF Reconstruction for $N = 144$ Projections. (b) PSF Orientation. . . . .	113
6.1	Comparison of RTI and DTI Reconstructions . . . . .	118

A.1	Placement of the $(x, y)$ , $(x'_1, y'_1)$ , $(x''_1, y''_1)$ , and $(x'''_1, y'''_1)$ Coordinate Systems with respect to the Scan Lines. . . . .	126
-----	---	-----



# Chapter 1

## Introduction

For measuring the range and bearing of a distant object, no instrument outperforms radar. Since before WWII, **RA**dio **D**etection **A**nd **R**anging has been applied successfully to a number of location, tracking, discrimination and remote sensing applications [1, 2]. Even after 50 years, the frontiers are being pushed forward with the development of storm sensitive Doppler-weather radar [3, 4], the testing of an over-the-horizon tracking radar in Maine [5, 6] and the operation of a high-resolution terrain mapping radar platform in orbit about the planet Venus [7, 8].

Radar operation diagrammed in Figure 1.1. The radar transmitter sends a pulse of electromagnetic radiation out into space toward a distant target. When the pulse reaches the target, some of the pulse energy is reflected back to the radar set. The radar receiver measures the direction of the arriving echo and computes the target range from the round-trip flight time of the transmitted pulse.

While radar is primarily designed to measure range and bearing, a number of secondary target characteristics can be gleaned from the target echo. For instance, the target size, shape and composition affect the magnitude of the received echo. Short-pulse radars can find the range-resolved cross-section of an extended target by recording the return echo created by the transmission pulse traveling over the

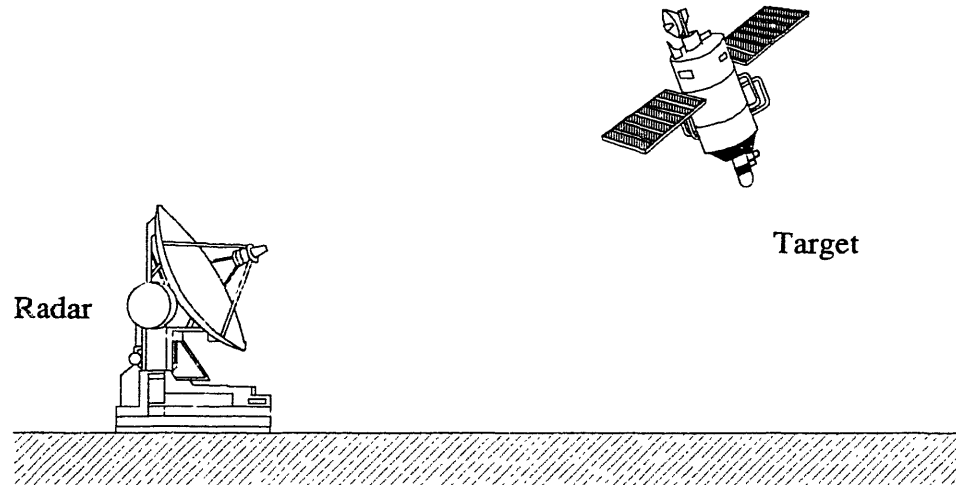


Figure 1.1: Radar Operation

target surface. Any gross Doppler frequency shift within the received return indicates target motion along the radar's line-of-sight. Furthermore, spectral broadening of the received echo shows relative motion between the components of an extended target even if the target is unresolved by the radar transmitter beam. For example, an *approaching* helicopter will exhibit a large echo shifted upward in frequency due to the moving airframe, but the motion of the whirling blades relative to the aircraft body will broaden the received spectrum about this gross frequency shift. In fact, this effect can be used by radar set operators to classify airborne targets by measuring the Doppler spread caused by aircraft blade rotation [2, p. 18.36].

Of course, target imaging provides the most straightforward means of identification. Radar imaging can be approached two different ways. In the first approach, the distant target can be raster scanned by a tightly focused beam which resolves the target at the detail level of interest. Alternatively, the evolution of the target's radar cross-section, projected onto either the range or cross-range axis, can be recorded

as the target exposes all surface aspects to the radar through rigid body rotation. The unique contribution of each target surface feature to each projection can then be exploited to reconstruct an image of the target.

To see how these “projections” are produced in the second imaging scenario, consider the return from a rotating target. For a short-pulse radar employing a broadband receiver, the cross-sectional range projections are found by simply recording the return echo over the total range extent of the target. A number of these range-resolved projections, each of a different target aspect, are then used to reconstruct the target image.

The measurement of the complement cross-range target projections is a bit more complicated. From the point of view of the radar transmitter, all areas on the rotating target surface with identical longitudinal velocity share the same return Doppler frequency shift. In other words, the return spectrum corresponds to a profile of the regions on the exposed surface with the same line-of-sight velocity. As with the range-resolved measurements, this resulting set of velocity “projections” of the rotating target can also be combined via tomographic techniques to form an image of the target.

High-resolution raster scan imaging at radio and microwave frequencies requires huge antennas or the application of interferometry, and projection-based imaging requires a very large broadband transmitter/receiver pair or a very sensitive Doppler receiver. At standard radar frequency bands these requirements can be difficult to meet. But, by switching to optical wavelengths, targets may be imaged by systems with relatively small apertures.

## 1.1 Optical Radar

Radars have been constructed which utilize pulse carrier frequencies from the tens of megahertz up to the hundreds of terahertz, in the realm of optical frequencies [2, §1.4]. In the optical regime, radar set transmitters use lasers to generate and control the intense pulses required for target interrogation. By virtue of their small working wavelength, these laser radars can be compact, high-resolution systems.

Laser radar set receivers use photodetectors to convert the target echo into an electronic signal. These photon sensitive devices respond to the optical power falling on the detector surface. Specifically, in the absence of excess noise sources, such as speckle, etc. (see below), photons strike the detector with Poisson distributed interarrival times at a rate proportional to the received optical power. Since the detector output is a superposition of the responses of individual photons impinging the detector surface, the detector response is essentially a shot noise process. This means the detector output will have a noise component which cannot be separated from the signal and is dependent upon the received signal strength. The requirements for the range-resolved imaging scheme described in the previous section can be met by employing a photodetector with a very fast response time.

A Doppler-imaging laser radar system, built according to the principle described earlier, must have a receiver capable of discerning small frequency shifts of the optical carrier frequency. This requirement is met by employing optical heterodyne detection within the receiver. Heterodyne detection has the added advantage of being highly sensitive to signals near the desired carrier frequency but relatively unresponsive to any extraneous background light. Figure 1.2 shows a block diagram of the heterodyne detection scheme. The target echo riding on an optical carrier of  $\nu_o$  Hz and the back-

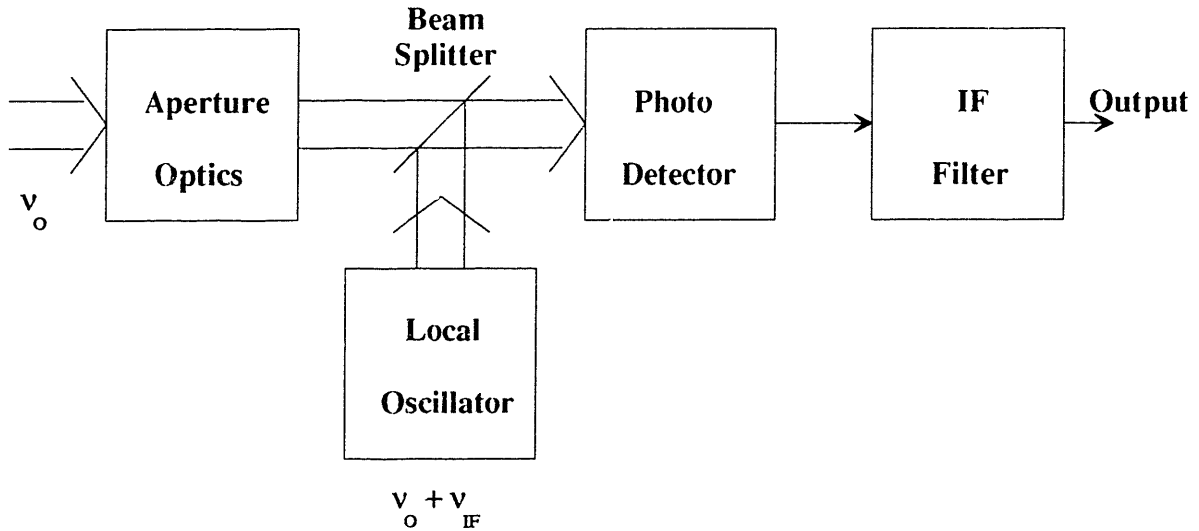


Figure 1.2: Optical Heterodyne Detection

ground light are gathered by the receiver aperture optics and fall on the photodetector through a beam splitter. Light from the local oscillator at a frequency of  $\nu_o + \nu_{IF}$  Hz is combined with the light collected at the receiver aperture. The electric fields of the aperture- and local oscillator-light are mixed on the surface of the intensity sensitive (square-law) photodetector. The  $\nu_{IF}$  beat-frequency component of the photodetector output is separated from the other output signals by the intermediate frequency (IF) filter. Therefore, the IF filter output is proportional to the received target echo and the local oscillator field strengths. If the local oscillator power is much greater than the received signal power, then the IF noise level is dominated by the local oscillator shot noise [9].

The above heterodyne detection description assumed perfect wavefront alignment and field polarization between the target echo and local oscillator. In fact, this is almost never the case. As the coherent laser light travels from the transmitter, it strikes targets often characterized by surface roughness much greater than the laser

wavelength. As seen from the receiver, the returning echo is composed of the light reflected from the target with seemingly random phase fluctuations distributed over the exposed surface of the target. The spatial coherence of the transmitted beam has been destroyed by microscopic surface variations along the line-of-sight. This random wavefront distortion causes constructive and destructive wave interference at the receiver aperture. The target looks mottled or speckled to the receiver [10, 11, 12, 13]. This effect is exacerbated by turbulence-induced refractive index changes in the atmosphere [14, 15]. Since the field at the aperture is the superposition of the echo returns from all the independent randomly phased scattering centers on the target surface, the net field will exhibit circular-complex Gaussian statistics. Thus, the speckle phenomenon is a fading process which is exponentially distributed after intensity detection.

It should be noted that the earlier proposed range-resolved scheme, which uses direct detection, may also be prone to from the effects of speckle. Since the photodetector intercepts the return intensity field across the receiver aperture, the direct detector output shot-noise signal will be driven by the spatial distribution of the random speckle process.

## 1.2 Research Program

Because of their high-resolution capabilities, laser radars have been employed in imaging radar research. For relatively close targets, which can be resolved by the tightly collimated beams produced by lasers, images can be readily formed by raster scan angle-angle laser radars [10, 16, 17, 18, 19]. However, due to effects of diffraction, many interesting targets lie beyond the range at which beam collimation can be maintained. Therefore, to perform target imaging at extreme ranges we must switch from

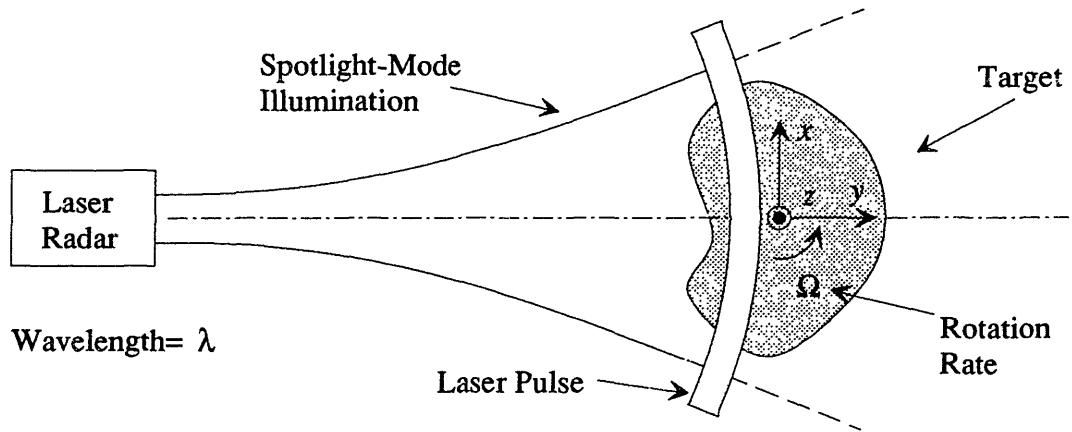


Figure 1.3: Laser Radar Imaging Example

the raster scan approach to either the range-resolved or Doppler-resolved imaging techniques introduced earlier [20, 21].

Consider the following laser radar imaging scenario. Suppose the three-dimensional stationary target in Figure 1.3 is undergoing rigid body rotation about an axis perpendicular to the plane of the page ( $z$ -axis). First, let the target be spotlight-mode illuminated by a broadband direct detection laser radar with a transmission pulse which is appreciably shorter than the target extent (e.g., super range resolution). The pulse train interrogation of the target results in a set of one-dimensional reflectance projections along the  $y$ -axis which is called the range-time-intensity (RTI) record.

Likewise, cross-range projections can be formed by continuously illuminating the target with a heterodyne laser radar in spotlight-mode. Due to the relative motion between the radar and the rotating target, each return from an illuminated point on the target surface will have an associated Doppler frequency shift. In fact, points on the exposed surface and in the two-dimensional plane  $x = a$  will all have returns

with a  $2a\Omega/\lambda$  Doppler frequency shift. This means that the magnitude of the signal spectrum at the output of the IF filter at a frequency of  $\nu_{IF} + 2a\Omega/\lambda$  corresponds to the total *line-of-sight* target reflectivity within the  $x = a$  plane. In other words, the magnitude of the receiver output spectrum centered at  $\nu_{IF}$  Hz is proportional to the one-dimensional projection of the line-of-sight target reflectivity onto the cross-range axis (i.e., the  $x$ -axis in Figure 1.3) . A series of Doppler-resolved projections taken over the target revolution is called the Doppler-time-intensity (DTI) record.

Can either set of RTI or DTI projections be used to reconstruct an image of the target? The answer is yes. Image reconstruction from projections is the basis of tomography. This technique has been successfully used to create cross-section images of the human body from x-ray attenuation projections. Researchers have experimentally applied these tomographic techniques to laser radar RTI and DTI recordings to produce two-dimensional images of three-dimensional objects [22, 23, 24, 37].

Figure 1.4 shows a typical near-field RTI data set gathered<sup>1</sup> from an optically diffuse cone slowly rotating perpendicular to the target central axis. On the right-hand-side, the return intensity is plotted on a grey scale versus both the range- and projection angle-axes. At a fixed projection angle, the intensity vs. range profile is a projection of the laser radar target cross-section onto the range-axis. In this example, the projection angle axis begins with a target nose-on view at  $0^\circ$ , progresses to a broadside view at  $90^\circ$ , a base view at  $180^\circ$ , and finally a second broadside view at  $270^\circ$  before completing the circle. Since target surfaces normal to the line-of-sight will reflect the greatest amount of energy back to the radar, peak returns are recorded for the two target broadside views. The left-hand-side of the figure shows three range

---

<sup>1</sup>This example was provided by Dr. Richard M. Marino of the Laser Radar Measurements Group at the M.I.T. Lincoln Laboratory.



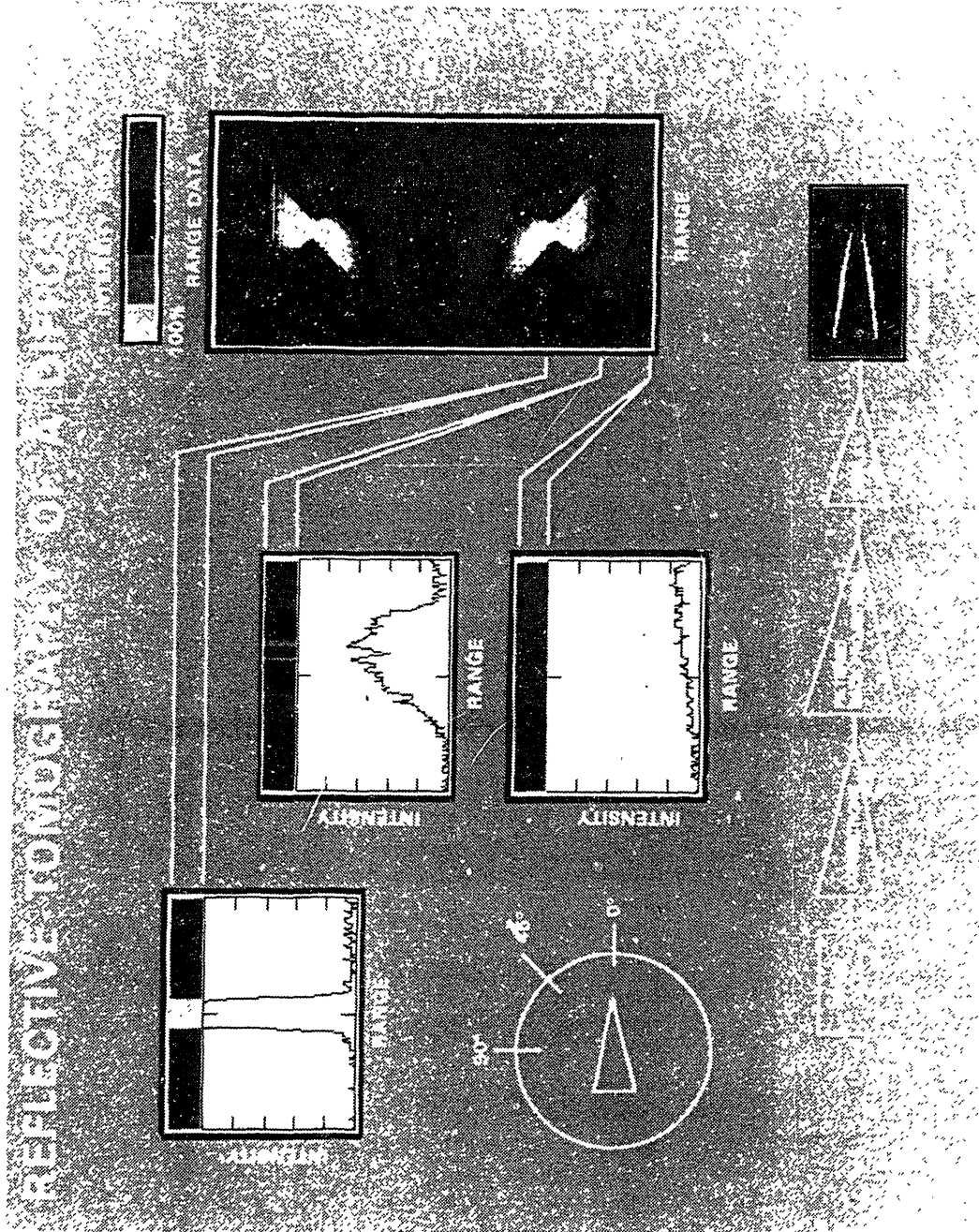


Figure 1.4: A Range-Time-Intensity Imaging Example

projection examples. Even though the direct detection intensity data was averaged, each projection still exhibits the corrupting effects of speckle, shot-noise and receiver front-end noise. The bottom right-hand-side presents the two-dimensional image of the cone recovered via tomographic reconstruction techniques applied to the RTI data. In general, researchers have noted that RTI reconstructions emphasize the outline of the target, leaving the interior unfilled, while the companion DTI technique produces silhouette-type images which have smoothed and softened target outlines [37].

The goal of this doctoral research program is to extend the above RTI and DTI tomographic work to a theoretical analysis of the performance of both laser radar imaging systems.

First, a realistic model will be developed of a both the RTI and DTI tomographic imaging systems which includes the effects of operating wavelength, radar-target geometry, target characteristics, coherent and direct detection, projection processing and extraction, and finally tomographic reconstruction. Next, the first and second moment projection statistics will be derived in a manner which takes into account speckle, photodetector shot-noise and any excess receiver front-end noise. Finally, these results will be woven together to produce two measures of image reconstruction quality: the image point spread function (PSF) and the image signal-to-noise (SNR). These quantities will be the used to interpret previous experimental results.

This dissertation is outlined as follows. The second chapter introduces the reader to the methods and mathematics of tomography. In preparation for the full laser radar problem, the third chapter discusses a simple two-dimensional speckle field tomography problem. Here, we explore the reconstructed image's first and second moment behavior as well as the image signal-to-noise ratio and resolution. To the author's knowledge, these results for projections corrupted by speckle noise have not

been investigated in the literature. The fourth and fifth chapters present the RTI and DTI analysis, respectively. As was the case for chapter three, the results of the RTI and DTI analysis have not previously appeared in the laser radar literature. Chapter six compares the theoretical results with previous experiment and simulation. The final chapter summarizes this research and suggests future work.



## Chapter 2

# The Mathematics of Tomography

Researchers are often faced with representing the characteristics of two- or three-dimensional objects in image form. For example, a medical doctor searching for a tumor will find cross-section images of the human body produced by non-invasive techniques a valuable diagnostic tool. Likewise, the rocket engineer wishing to ensure the proper distribution of propellant within a solid fuel motor will examine a three-dimensional representation of motor propellant density. The astronomer may be interested in imaging the x-ray emission from a supernova remnant or mapping the electron density of the Sun's corona over the entire solar surface. In all of the above cases, the two- or three-dimensional image of the object of study cannot be obtained with conventional photographic or electronic raster scan techniques. Rather, in all these cases and others, the technique of image reconstruction from projections has been successfully applied [25]. In this chapter we will study these techniques from a mathematical perspective. However, we will first overview these techniques by examining one of the above applications in detail.

The classic illustration of the application of these techniques comes from medical science, where mathematics, computer science and radiology were combined to

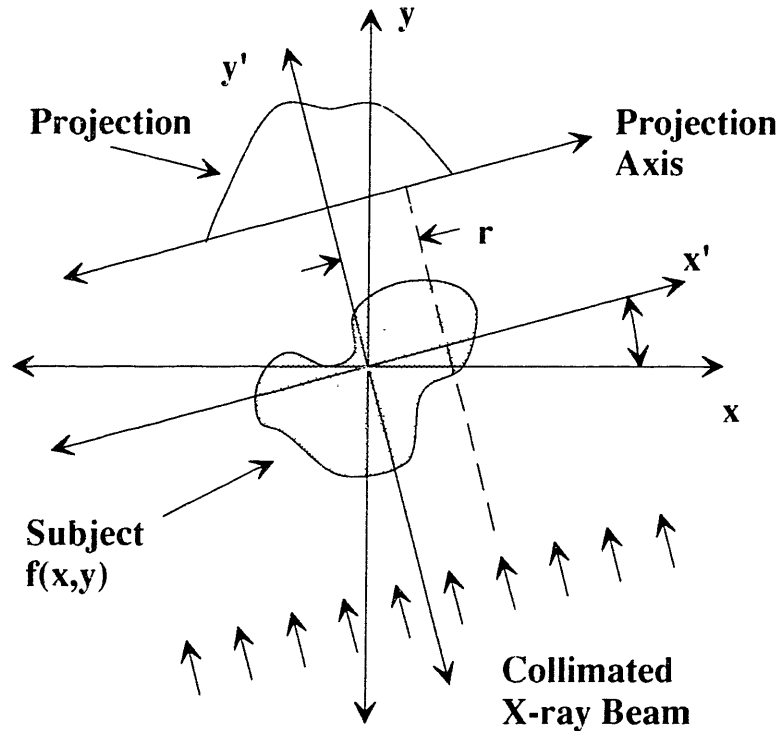


Figure 2.1: Computerized Tomography Geometry.

develop the technology called computerized tomography<sup>1</sup> (CT)<sup>2</sup>. The elementary principles behind CT are demonstrated in Figure 2.1 [26]. The subject is illuminated with a collimated sheet of penetrating radiation, usually x-rays. A row of closely spaced detectors on the far side of the subject measures the amount of radiation exiting the subject. Assuming that radiation travels in straight lines, the response at any point on the detector array is an estimate of the radiation transmission from that point back along a line passing through the subject to the radiation source. The line integral of the attenuation coefficient  $f(x,y)$  over the line  $L$  can be extracted from this

<sup>1</sup>The word *tomography* is derived from the Greek word meaning “slice.” It is used in the context of medical radiology to describe various methods to image cross-sections of the human body.

<sup>2</sup>Computer *assisted tomography*, computer *aided tomography* or computed *axial tomography* (CAT) is also used, as in the term “CAT scanner.”

transmission profile via the relation

$$\text{Transmission} = \exp \left\{ - \int_L f dl \right\} \quad (2.1)$$

In other words, this measurement corresponds to a line integral of the instantaneous radiation attenuation coefficient. For the given source-detector orientation angle,  $\theta$ , the detector array response estimates the collection of line integrals of the instantaneous attenuation coefficient  $f(x, y)$  lying in the cross-section plane. For this fixed orientation  $\theta$ , this response, denoted as  $p_\theta(r)$ , is called the *projection* of  $f(x, y)$ ; it is a function of the cross-range distance,  $r$ . The challenge is to reconstruct the “image” of the instantaneous attenuation coefficient  $f(x, y)$  from the set of projections  $p_\theta(r)$  over all values of the angle  $\theta$ .

The collection of all line integrals of a function  $f(x, y)$  is called the Radon transform of  $f$ . The problem of finding  $f$  given the Radon transform of  $f$  was solved mathematically by Radon in his 1917 paper<sup>3</sup>. Computer based signal processing algorithms based upon Radon’s solution have been applied to the CT problem and others like it with great success. Motivated by this work, we will survey the mathematical foundations of the Radon transform and derive its inverse in order to apply the results to Doppler laser radar imaging.

## 2.1 The Radon Transform

We begin our discussion of the two-dimensional Radon transform by first building a geometrical framework for this operator. Consider the line in the  $x$ - $y$  plane specified by  $r = x \cos \theta + y \sin \theta$ . By rewriting this equation as the dot product  $r = (x, y) \cdot$

---

<sup>3</sup>Radon, J. (1917). Über die Bestimmung von Funktionen durch ihre Integralwerte längs gewisser Mannigfaltigkeiten. *Berichte Sachsische Akademie der Wissenschaften, Leipzig, Math.-Phys. Kl.*, **69**, 262-267.

$(\cos \theta, \sin \theta)$  we see that this line is perpendicular to the vector  $\vec{\theta} = (\cos \theta, \sin \theta)^T$  and falls a distance  $r$  from the origin. This formulation allows us to easily specify any line in  $R^2$  by choosing  $r$  and  $\theta$  in an appropriate manner. If we restrict  $\theta \in [0, \pi]$  and allow  $r \in R$  then the space  $P = R \times [0, \pi]$  containing the ordered pairs  $(r, \theta)$  naturally represents the set of all lines in the  $x$ - $y$  plane. Note that  $P$  cannot be taken as the familiar polar form because  $r$  can be negative.

The two-dimensional Radon transform uses the line integral to map a function on the  $x$ - $y$  plane to a function on the space  $P$ . Using the symbol  $\mathfrak{R}$  to denote the Radon transform operator, the Radon transform of  $f(x, y)$  is

$$[\mathfrak{R}f](r, \theta) = \int \int dx dy \delta(r - x \cos \theta - y \sin \theta) f(x, y). \quad (2.2)$$

For a fixed  $(r, \theta)$ ,  $\mathfrak{R}f$  is simply the line integral of  $f(x, y)$  over the line  $r = x \cos \theta + y \sin \theta$ . Thus, the Radon transform decomposes a two-dimensional function into the set of all line integrals. Note that  $\mathfrak{R}f$  obeys  $[\mathfrak{R}f](r, \theta) = [\mathfrak{R}f](-r, \theta + \pi)$  because these transform values are line integrals traversing the same line in opposite directions, cf. Figure 2.1.

A few words about notation are in order. We will often consider instances in which  $\theta$  is fixed and  $r$  is an independent variable. It will be convenient to represent these cases as  $[\mathfrak{R}_\theta f](r)$ , emphasizing the  $r$  dependence. This is equivalent to our notion of the tomographic projection  $p_\theta(r)$  in Figure 2.1. Furthermore, all single dimensional Fourier and convolution operations on Radon transforms are understood to apply *only* with respect to the variable  $r$ . With this convention in mind, we write

$$[\mathcal{F}\mathfrak{R}f](\varrho) = \int dr e^{-2\pi j\varrho r} [\mathfrak{R}_\theta f](r),$$

and

$$[g \star \mathfrak{R}f](r) = g(r) \star [\mathfrak{R}_\theta f](r)$$



$$= \int d\tau g(r - \tau)[\mathfrak{R}_\theta f](\tau).$$

To familiarize ourselves with these concepts and explore the connection between the Radon and the Fourier transforms we prove the following theorem known in the literature as the Fourier slice theorem or projection theorem [27, §II.1].

**Theorem:** If  $\varrho \in R$  then  $[\mathcal{F}\mathfrak{R}_\theta f](\varrho) = [\mathcal{F}f](\varrho\vec{\theta})$

This theorem states that the single-dimensional Fourier transform of projection  $\mathfrak{R}_\theta f$  with respect to the variable  $r$  is the cross-section of the two-dimensional Fourier transform  $\mathcal{F}f$  in the direction of  $\vec{\theta} = (\cos \theta, \sin \theta)^T$ . We begin our proof with the left hand side.

$$\begin{aligned} [\mathcal{F}\mathfrak{R}_\theta f](\varrho) &= \int dr e^{-2\pi j\varrho r} [\mathfrak{R}_\theta f](r) \\ &= \int dr e^{-2\pi j\varrho r} \int \int dx dy \delta(r - x \cos \theta - y \sin \theta) f(x, y) \\ &= \int \int dx dy e^{-2\pi j\varrho(x \cos \theta - y \sin \theta)} f(x, y) \\ &= [\mathcal{F}f](\varrho \cos \theta, \varrho \sin \theta) \\ &= [\mathcal{F}f](\varrho\vec{\theta}). \end{aligned}$$

The reader will recognize that this theorem offers a path to inverting the Radon transform. The function  $f(x, y)$  can be recovered from  $\mathfrak{R}f$  by applying the two-dimensional inverse Fourier transform to  $\mathcal{F}f$  reconstructed from the Fourier slices  $\mathcal{F}\mathfrak{R}_\theta f$  for all  $\theta$ . However, in practical sampled-data tomographic systems this approach is not highly accurate and produces image artifacts [27, §V.2]. Rather, in the context of these systems, researchers have pursued the inverse problem by using the backprojection operator [27, ch. V]. We now turn our attention to this operator.

## 2.2 Backprojection Image Reconstruction

To motivate our study of the backprojection operator let us appeal to our earlier tomography example illustrated in Figure 2.1. Suppose we wish to construct a cross-sectional image of our subject using the set of projections  $p_\theta(r)$ . For a given point  $(x, y)$  in the plane, we realize that each projection  $p_\theta(r)$  at  $r = x \cos \theta + y \sin \theta$  must contain information about the value of  $f(x, y)$ . We might try to extract this information about  $f(x, y)$  from our projections by summing over  $\theta$  the values of  $p_\theta(r)$  such that  $r = x \cos \theta + y \sin \theta$ . In essence, we are forming an image by propagating or “backprojecting” the values of each projection  $p_\theta(r)$  along the lines  $r = x \cos \theta + y \sin \theta$  across the  $x$ - $y$  plane and then summing over  $\theta$ . This backprojection operation maps functions from the space  $P$  to the  $x$ - $y$  plane ( $R^2$ ). For the continuous transmission-tomography case, the backprojection operator  $\mathcal{B}$  is defined by [25, §2.2.3]

$$[\mathcal{B}p](x, y) = \int_0^\pi d\theta p_\theta(x \cos \theta + y \sin \theta). \quad (2.3)$$

Note that this operator is a dual to the Radon transform in the sense of line-integral geometry: the Radon transform sums all values of a function  $f(x, y)$  along a fixed line while the backprojection operator sums the values of a function associated with all lines  $(r, \theta)$  passing through a fixed point.

## 2.3 The Inverse Radon Transform

The reconstructed images produced by backprojection incur a smearing-type of distortion. More specifically, by applying the backprojection operator to the Radon transform of function  $f(x, y)$ , it can be shown that  $[\mathcal{B}\mathcal{R}f](x, y) = \frac{1}{\sqrt{x^2+y^2}} \star f(x, y)$  where  $\star$  signifies two-dimensional convolution [27, Theorem 1.5]. This result, however, suggests an alternative method for inverting the Radon transform. Taking  $f_x$

and  $f_y$  as spatial frequencies, we have via the two-dimensional Fourier transform

$$\begin{aligned} [\mathcal{FB}\mathcal{R}f](f_x, f_y) &= \mathcal{F} \left[ \frac{1}{\sqrt{x^2 + y^2}} * f(x, y) \right] \\ &= \frac{1}{\sqrt{f_x^2 + f_y^2}} [\mathcal{F}f](f_x, f_y). \end{aligned}$$

The backprojected image suffers from a multiplicative radially-dependent distortion in the frequency domain. Every radial cross-section in the spatial frequency domain or Fourier slice of the backprojected image has been distorted by a  $1/|\varrho|$  filtering process where  $\varrho$  is the radial spatial frequency variable. Applying the Fourier slice theorem, we see that this distortion can be eliminated by prefiltering projections  $p_\theta(r)$  with the radial spatial frequency function  $|\varrho|$ . That is, applying the backprojection operator to  $\mathcal{F}^{-1}[|\varrho| \times \mathcal{F}[p_\theta(r)]]$  recovers  $f(x, y)$  with perfect fidelity. This formulation of the inverse Radon transform is called filtered backprojection in the literature [26, ch. 7]. Good accuracy and moderate computation requirements make filtered backprojection a favored starting point for developing algorithms in practical tomographic systems.

## 2.4 Sampling and Resolution

Modern tomographic systems are sampled-data machines employing digital signal processing [25, ch. 2]. The above theory must be recast in discretized form to be relevant. In the semi-discrete case, projections are taken on a finite set of  $N$  angles. Writing this set of projection angles as  $\{\theta_n : n = 0, N - 1\}$ , the backprojection operator becomes

$$\sum_{n=0}^{N-1} (\theta_{n+1} - \theta_n) p_{\theta_n}(x \cos \theta_n + y \sin \theta_n). \quad (2.4)$$

For  $N$  equiangular projections about the half circle (transmission-tomography case) we have

$$\sum_{n=0}^{N-1} \frac{\pi}{N} p_{\frac{\pi}{N}n} \left( x \cos \frac{\pi}{N}n + y \sin \frac{\pi}{N}n \right). \quad (2.5)$$

In the fully-discrete case each projection  $p_{\theta_n}(r)$  has been sampled along the radial variable  $r$ .

Naturally, the sampled-data model begs questions concerning accuracy and resolution. The Shannon sampling theorem answers these questions by specifying the sampling grid mesh size in terms of the bandwidth of  $f(x, y)$ . Assume that  $f(x, y)$  is spatially limited (compact) such that  $f(x, y)$  is negligible for all  $|(x, y)| \geq \mathcal{R}$ . Furthermore, assume that the Fourier transform  $[\mathcal{F}f](f_x, f_y)$  is also negligible in the spatial frequency domain for  $|(f_x, f_y)| \geq b$  ( $f(x, y)$  is  $b$ -bandlimited). Note by the Fourier slice theorem that each projection of  $f(x, y)$  must also be spatially limited and  $b$ -bandlimited.

In the fully discrete case each projection is represented by a set of samples along the  $r$ -axis. According to the Shannon sampling theorem, the spatial sampling interval must be less than the reciprocal of the Nyquist spatial frequency  $2b$ . Therefore, since each projection is spatially limited, these projections may be fully recovered from a minimum of  $2q + 1$  samples where  $q = \mathcal{R}/(2b)^{-1}$ . This sets the sampling requirements for each projection.

We will now consider the overall two-dimensional sampling requirements for reconstructing an image of  $f(x, y)$  from a set of  $N$  projections. Proceeding with a heuristic argument, this will lead to a lower bound on  $N$  in terms of  $\mathcal{R}$  and  $b$ .

Assume that we are dealing with the equiangular-projection transmission-tomography case, i.e., projections are equally spaced such that  $\theta_n = n\pi/N$ . By the Fourier slice theorem, the Fourier space of  $f(x, y)$  has been sampled in a radial pattern like

the spokes of a wheel. These spoke sampling angles in the spatial frequency domain are identical to the projection angles. Therefore, we must select a radial sampling grid which approximates the rectangular sampling grid specified by the two-dimensional Shannon sampling theorem.

In the spatial frequency domain, the sampling mesh size of the radial grid increases with distance from the origin. The largest mesh occurs at the edge of the frequency sample space and has a size of  $\pi b/N$ . This sample size must be the upper limit of the corresponding mesh size of the rectangular *spatial frequency* sampling grid ( $1/2\mathcal{R}$ ) specified by the two-dimensional sampling theorem. Therefore, for a spatially and frequency limited function, we have

$$\frac{1}{2\mathcal{R}} > \frac{\pi b}{N} \quad (2.6)$$

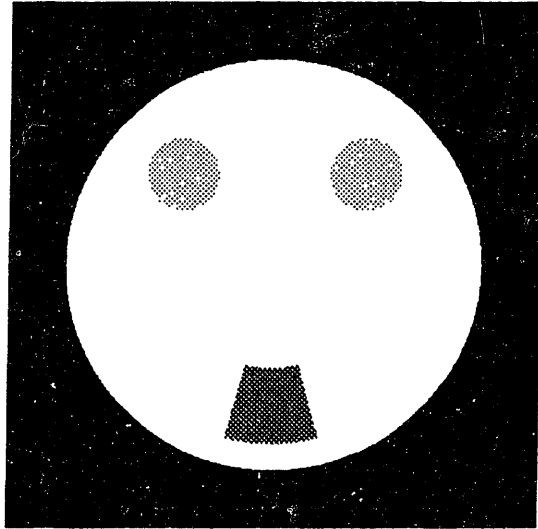
or

$$N > \pi q. \quad (2.7)$$

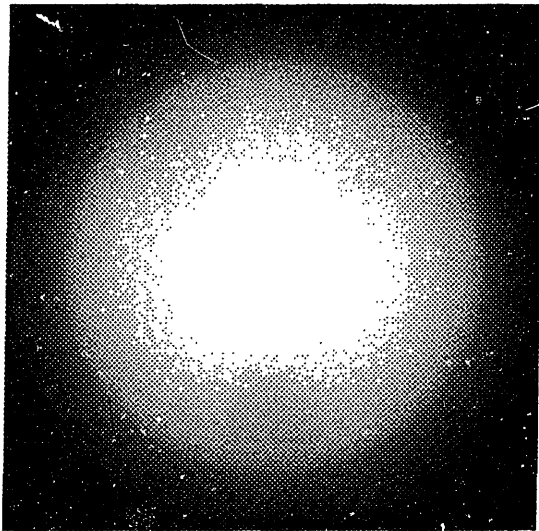
Thus, if we are required to sample projections  $2q + 1$  times to satisfy the bandwidth constraints of  $f(x, y)$ , then we must use at least  $\pi q$  projections to recover  $f(x, y)$ .

## 2.5 Reconstruction Example

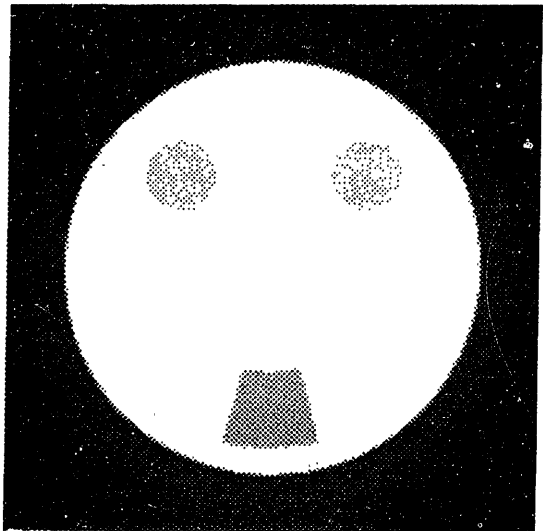
To put these concepts into perspective, Figure 2.2 displays a demonstration of back-projection and filtered backprojection reconstruction. Transmission projections were numerically computed at  $1^\circ$  increments for the two-dimensional gray scale phantom shown in Figure 2.2 (a). Backprojection and filtered backprojection reconstruction was applied to this set of projections, resulting in the gray scale Figures 2.2 (b) and (c), respectively. Note that the backprojection reconstruction has a “washed-out” or



(a)



(b)



(c)

Figure 2.2: Phantom Reconstructions: (a) Original Phantom, (b) Backprojection Reconstruction, (c) Filtered Backprojection Reconstruction.

smearing appearance typical of this approach, while the filtered backprojection reconstruction restores the original phantom with little degradation.





## Chapter 3

# Two-Dimensional Speckle Field Tomography

As a prelude to an investigation of laser radar tomography, we now examine a two-dimensional speckle field tomography problem which incorporates some of the aspects of the more complex laser radar model. Here, we propose constructing projections of a two-dimensional object by intensity detecting the back-scatter of a penetrating beam of *coherent* radiation. Since the field impinging on the detector will be the superposition of the back-propagated fields from all the scattering sites illuminated by the probe beam, each projection will be corrupted by speckle-like noise. Our investigation will center on describing the first and second moment behavior of the image reconstructed from these speckled projections using semi-discrete tomographic methods.

### 3.1 Tomographic Speckle Model

Imagine a transparent test cell filled with a fine aerosol of randomly sized and haphazardly placed particles which scatter light. Suppose we wish to use a narrowly collimated beam of coherent laser light to determine the two-dimensional distribu-

tion of the reflectance density over a plane passing through the test cell. Conceivably, this could be accomplished by measuring the optical backscatter striking a light detector pointed into the test cell and focused along the laser's line-of-sight. The laser-photodetector pair could be used to form a reflectance projection of the cell's contents by sampling along the cross-range axis at a fixed orientation. Projections could be taken over a number of aspect angles about the plane and combined through tomographic techniques to form an estimate of the reflectance density. It is the impact of speckle upon this simplified scenario that we wish to investigate.

Ultimately, we will want to characterize the performance of this imaging scheme in terms of the resolution and signal-to-noise of the reconstructed density. The statistics of these quality measures will be driven by the aerosol's scattering characteristics. Therefore, we begin our investigation by specifying the tomographic scanning geometry and the objects's scattering statistics.

Let the circulo-complex Gaussian random process  $\mathbf{s}(x, y)$  represent the scattering coefficient of a bounded two-dimensional object resting in the  $x$ - $y$  plane. The squared magnitude of  $\mathbf{s}(x, y)$  is understood to be the intensity ratio of the scattered radiation to the incoming illumination at the point  $(x, y)$ . The phase of  $\mathbf{s}(x, y)$  accounts for random and uncontrollable variations in the optical round trip path length to the scattering site.

Assume  $\mathbf{s}(x, y)$  has the following first and second moment statistics:

- $\langle \mathbf{s}(x, y) \rangle = \mathbf{0}$
- $\langle \mathbf{s}(x_1, y_1) \mathbf{s}(x_2, y_2) \rangle = \mathbf{0}$
- $\langle \mathbf{s}(x_1, y_1) \mathbf{s}^*(x_2, y_2) \rangle = f(x_1, y_1) \delta(x_1 - x_2) \delta(y_1 - y_2)$

where the object's reflectance is modelled by the deterministic two-dimensional function  $f(x, y)$ .

The above expectations are justified as follows. The first expectation is simply the average of a circulo-complex Gaussian random variable. Therefore, the mean of this phasor will be  $\mathbf{0}$ . The second expectation is over the product of two of these random phasors, which will likewise have a mean of  $\mathbf{0}$ . The final expectation is the complex phase correlation with respect to the spatial coordinates. Since scattering sites are assumed to be statistically independent, this correlation was chosen to be a delta function weighted by the scattering site's reflectivity  $f(x, y)$

We propose estimating  $f(x, y)$  by applying tomographic methods to scans of the object by a penetrating beam of coherent radiation. Assume the beam axis lies on the line  $(r, \theta)$  in the standard two-dimensional tomographic geometry shown in Figure 3.1. We assume the narrow probe beam maintains perfect collimation throughout penetration of the object. Furthermore, let the field profile  $b_r(x', y')$  of the probe beam be Gaussian shaped such that the total beam illumination is constant regardless of the beam width:

$$b_r(x', y') = \frac{1}{\sqrt{\pi r_{\perp}^2}} e^{-(x'-r)^2/r_{\perp}^2}. \quad (3.1)$$

This formulation of the beam profile is expressed in the rotated projection Cartesian coordinate system  $(x', y')$  where the beam axis (scan line) is perpendicular to the  $x'$ -axis and fixed  $r$  meters from the  $y'$ -axis. The parameter  $r_{\perp}$  controls the beam width, and in some sense, models the finite size of the scanner's transmitter/receiver optics. In other words, the profile of  $b_r(x', y')$  along the  $x'$ -axis is the instrument function of the coherent optical scanner. At the outset  $r_{\perp}$  should be chosen smaller than the smallest detail to be imaged in the distribution of  $s(x, y)$ .

Suppose the probe signal is received by an intensity detector located  $R$  meters

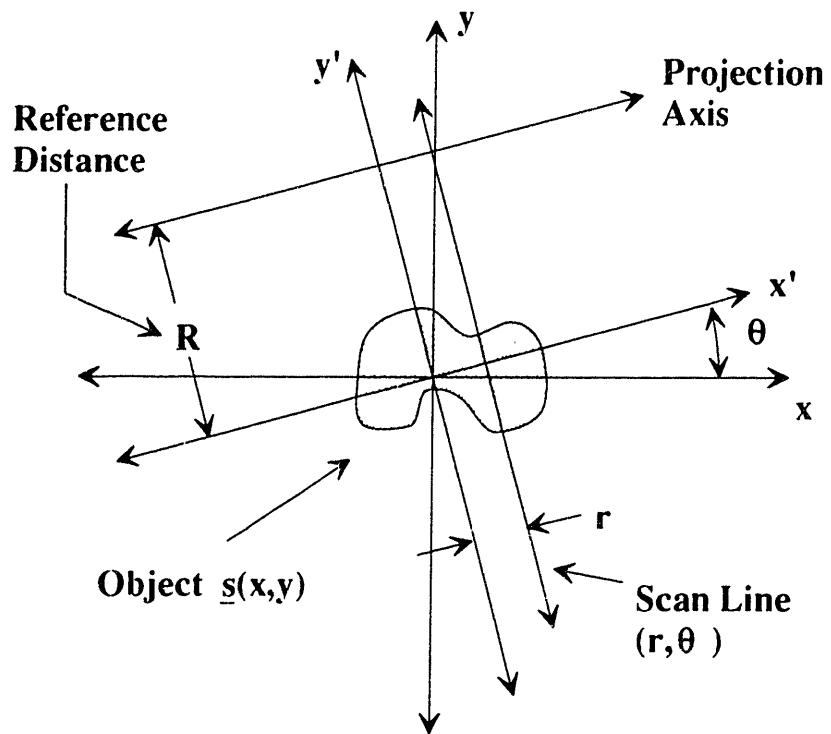


Figure 3.1: Two-Dimensional Speckle Tomography Geometry.

from the  $x'$  axis. Assuming negligible beam attenuation, we can write the *complex* signal field envelope at the infinite extent detector as

$$\mathbf{R}(r, \theta) = \int_{-\infty}^{\infty} \int_{-\infty}^{\infty} dx' dy' s(x(x', y'), y(x', y')) b_r(x', y') e^{2jk(R+y')} \quad (3.2)$$

where  $k \equiv 2\pi/\lambda$  is the wavenumber. Note that we have reformulated the scattering distribution  $s(x(x', y'), y(x', y'))$  upon the rotated coordinate system  $(x', y')$  by specifying the following transform:

$$\begin{aligned} x(x', y') &= x' \cos \theta - y' \sin \theta \\ y(x', y') &= x' \sin \theta + y' \cos \theta. \end{aligned}$$

Since individual points lying in the probe beam's path reflect waves back to the intensity detector with random phase, the output signal will be corrupted by speckle noise.

## 3.2 Projection Statistics

Using the fact that  $|\mathbf{R}(r, \theta)|^2 = \mathbf{R}(r, \theta) \cdot \mathbf{R}^*(r, \theta)$  where the  $*$  denotes complex conjugate, the first moment of the detector response is then

$$\langle |\mathbf{R}(r, \theta)|^2 \rangle = \left\langle \int_{-\infty}^{\infty} \int_{-\infty}^{\infty} dx'_1 dy'_1 s(x_1(x'_1, y'_1), y_1(x'_1, y'_1)) b_r(x'_1, y'_1) e^{2jk(R+y'_1)} \int_{-\infty}^{\infty} \int_{-\infty}^{\infty} dx'_2 dy'_2 s^*(x_2(x'_2, y'_2), y_2(x'_2, y'_2)) b_r(x'_2, y'_2) e^{-2jk(R+y'_2)} \right\rangle.$$

Exchanging the expectation and integration operators, and substituting  $f(x_1, y_1) \cdot \delta(x_1 - x_2) \delta(y_1 - y_2)$  for the reflectivity correlation  $\langle s(x_1, y_1) s^*(x_2, y_2) \rangle$ , we find

$$\langle |\mathbf{R}(r, \theta)|^2 \rangle = \int_{-\infty}^{\infty} \int_{-\infty}^{\infty} dx'_1 dy'_1 f(x_1(x'_1, y'_1), y_1(x'_1, y'_1)) \frac{1}{\pi r_{\perp}^2} e^{-2(x'_1 - r)^2 / r_{\perp}^2}. \quad (3.3)$$

Recalling that  $r_\perp$  is small compared to the object's spatial detail, we make the approximation  $\frac{1}{\pi r_\perp^2} e^{-2(x'_1-r)^2/r_\perp^2} \approx \frac{1}{\sqrt{2\pi r_\perp^2}} \delta(x_1 - r)$  resulting in

$$\begin{aligned} \langle |\mathbf{R}(r, \theta)|^2 \rangle &\approx \int_{-\infty}^{\infty} \int_{-\infty}^{\infty} dx'_1 dy'_1 f(x_1(x'_1, y'_1), y_1(x'_1, y'_1)) \frac{1}{\sqrt{2\pi r_\perp^2}} \delta(x_1 - r) \\ &= \frac{1}{\sqrt{2\pi r_\perp^2}} \int_{-\infty}^{\infty} dy'_1 f(x_1(r, y'_1), y_1(r, y'_1)) \\ &= \frac{1}{\sqrt{2\pi r_\perp^2}} [\mathfrak{R}f](r, \theta). \end{aligned}$$

Thus, for small  $r_\perp$ ,  $\langle |\mathbf{R}(r, \theta)|^2 \rangle$  behaves like the Radon transform of the object's reflectance  $f(x, y)$  within a scale factor. Thus, within an approximation, it seems reasonable to regard  $\langle |\mathbf{R}(r, \theta)|^2 \rangle$  as a projection of the scattering object  $s(x, y)$ . While this result is intuitively pleasing because it makes physical sense, this analysis can be extended to explicitly include the effects of the Gaussian beam profile (instrument function) upon the Radon transform formulation.

Intuition tells us that features smaller than the probe beam's width will be lost or suffer from a smearing type of distortion. Starting with (3.3) and the definition of the Radon transform, it is easy to back out the result

$$\langle |\mathbf{R}(r, \theta)|^2 \rangle = \frac{1}{\sqrt{2\pi r_\perp^2}} g(r) \star [\mathfrak{R}_\theta f](r) \quad (3.4)$$

where  $g(r)$  has the Gaussian form

$$g(r) = \frac{1}{\sqrt{\pi r_\perp^2/2}} e^{-2r^2/r_\perp^2}. \quad (3.5)$$

Thus, each projection  $\langle |\mathbf{R}(r, \theta)|^2 \rangle$  is proportional to the true Radon transform  $[\mathfrak{R}_\theta f](r)$  convolved with a narrow Gaussian window. Using the fact that  $[\mathfrak{R}_\theta h](r) \star [\mathfrak{R}_\theta f](r) = [\mathfrak{R}_\theta (h(x, y) \star f(x, y))](r)$  we realize that we can extend the above result to

$$\langle |\mathbf{R}(r, \theta)|^2 \rangle = \frac{1}{\sqrt{2\pi r_\perp^2}} \mathfrak{R}[g(x, y) \star f(x, y)] \quad (3.6)$$

where

$$g(r) = \{\Re_{\theta}\{g(x, y)\}\}(r) \quad (3.7)$$

and

$$g(x, y) = \frac{\sqrt{2}}{\pi r_{\perp}^2} e^{-2(x^2+y^2)/r_{\perp}^2}. \quad (3.8)$$

Thus, the set of projections  $|\mathbf{R}(r, \theta)|^2$  formed by the above “narrow Gaussian-beam transform” correspond in the mean to the true Radon transform of the *convolution* of the reflectance  $f(x, y)$  and a function  $g(x, y)$  determined by the probe beam profile. The small-scale smearing caused by this effect will fundamentally limit the resolution of any reconstruction algorithm applied to  $|\mathbf{R}(r, \theta)|^2$ .

In addition to the first moment of  $|\mathbf{R}(r, \theta)|^2$ , it is of interest to characterize the cross-correlation between the received signal fields,  $\mathbf{R}(r_1, \theta_1)$  and  $\mathbf{R}(r_2, \theta_2)$ , for the two scan lines  $(r_1, \theta_1)$  and  $(r_2, \theta_2)$  respectively. That is, we wish to compute the cross-correlation  $\langle \mathbf{R}(r_1, \theta_1) \mathbf{R}^*(r_2, \theta_2) \rangle$  in the semi-discrete case. As shown in Figure 3.2, this expectation will be largely determined by the values of the reflectance  $f(x, y)$  within the “footprint” formed by the intersection of the two narrow probe beams along the scan lines  $(r_1, \theta_1)$  and  $(r_2, \theta_2)$ . This realization requires the consideration of two distinct geometrical cases.

First, suppose the projection angles  $\theta_1$  and  $\theta_2$  are equal. In this case, the two scan lines are parallel and the expectation will be nonzero when there is significant overlap between the two narrow probe beams (i.e.,  $r_1 \approx r_2$ ). This expectation can be approximated by

$$\begin{aligned} & \langle \mathbf{R}(r_1, \theta) \mathbf{R}^*(r_2, \theta) \rangle \\ &= \left\langle \int_{-\infty}^{\infty} \int_{-\infty}^{\infty} dx'_1 dy'_1 s(x_1(x'_1, y'_1), y_1(x'_1, y'_1)) b_r(x'_1, y'_1) e^{2jk(R+y'_1)} \right. \\ & \quad \left. \int_{-\infty}^{\infty} \int_{-\infty}^{\infty} dx'_2 dy'_2 s^*(x_2(x'_2, y'_2), y_2(x'_2, y'_2)) b_r(x'_2, y'_2) e^{-2jk(R+y'_2)} \right\rangle \end{aligned} \quad (3.9)$$

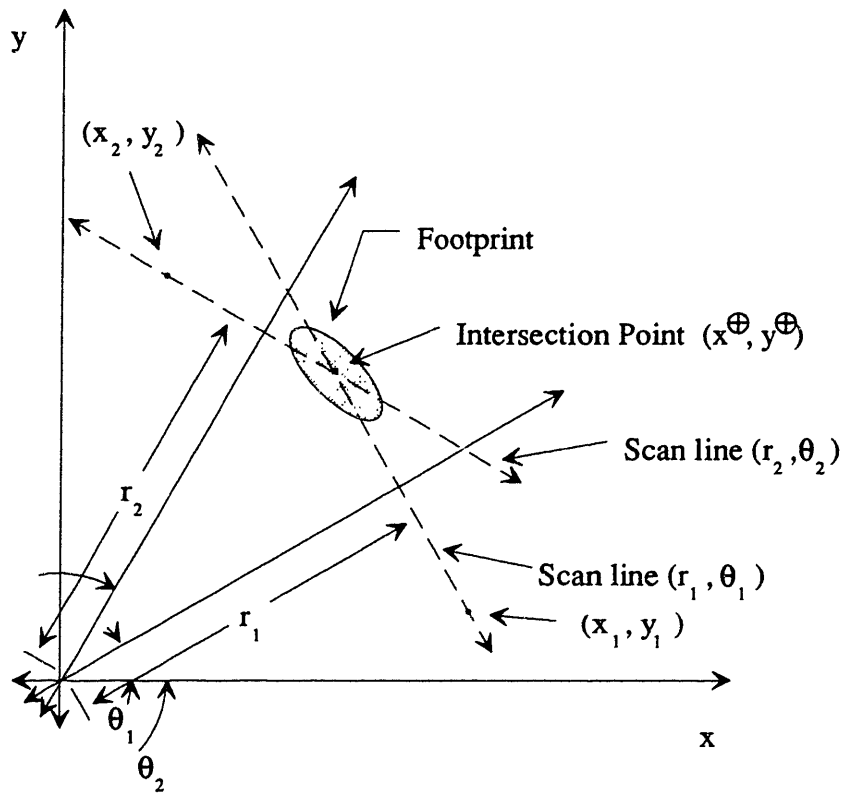


Figure 3.2: Covariance Calculation Geometry.



$$\begin{aligned}
&= e^{-(r_2-r_1)^2/2r_\perp^2} \int_{-\infty}^{\infty} \int_{-\infty}^{\infty} dx'_1 dy'_1 f(x_1(x'_1, y'_1), y_1(x'_1, y'_1)) \frac{1}{\pi r_\perp^2} e^{-2(x'_1-(r_2+r_1)/2)^2/r_\perp^2} \\
&\approx \frac{1}{\sqrt{2\pi r_\perp^2}} e^{-(r_2-r_1)^2/2r_\perp^2} [\mathcal{R}f]\left(\frac{r_2+r_1}{2}, \theta\right), \tag{3.10}
\end{aligned}$$

where the approximation is obtained by retaining the  $r_\perp$  small condition as before and passing to the Radon transform.

Second, consider the case when the two projection angles are unequal. In this scenario the two scan lines  $(r_1, \theta_1)$  and  $(r_2, \theta_2)$  always intersect at a single point  $(x^\oplus, y^\oplus)$  in the  $x$ - $y$  plane. The coordinates of this intersection point are dependent upon the values of  $(r_1, \theta_1)$  and  $(r_2, \theta_2)$  and take the values:

$$x^\oplus(r_1, \theta_1; r_2, \theta_2) = \frac{1}{\sin(\theta_2 - \theta_1)} (r_1 \sin(\theta_2) - r_2 \sin(\theta_1)) \tag{3.11}$$

$$y^\oplus(r_1, \theta_1; r_2, \theta_2) = \frac{1}{\sin(\theta_2 - \theta_1)} (-r_1 \cos(\theta_2) + r_2 \cos(\theta_1)). \tag{3.12}$$

Beginning with equation (3.9), the expectation can be manipulated into a complicated double-integral on a rotated coordinate system centered on the point  $(x^\oplus, y^\oplus)$  with an integrand of  $f$  and a complex phase factor windowed with the Gaussian profiles of the two probe beams. At this point, if we assume that the most significant contribution comes from the region of the intersection footprint of the two narrow probe beams, then the two beam profiles can be replaced with a single a two-dimensional Gaussian window centered on  $(x^\oplus, y^\oplus)$  with major and minor axis lengths a function of the angle of attack,  $\theta_2 - \theta_1$ , of the two scan lines. Again, assuming  $r_\perp$  is small and  $f(x, y)$  varies slowly within the Gaussian window patch, then the double-integral may be approximated by the value  $2f(x^\oplus(r_1, \theta_1; r_2, \theta_2), y^\oplus(r_1, \theta_1; r_2, \theta_2))/|\sin(\theta_2 - \theta_1)|$  times a complex phase factor. The factor of  $1/|\sin(\theta_2 - \theta_1)|$  accounts for the change in the size of the footprint area as the scan line angle of attack varies. Therefore, for

non-identical projection angles, the cross-correlation is approximated by

$$\langle \mathbf{R}(r_1, \theta_1) \mathbf{R}^*(r_2, \theta_2) \rangle = 2\mathcal{C} f(x^\oplus(r_1, \theta_1; r_2, \theta_2), y^\oplus(r_1, \theta_1; r_2, \theta_2)) / |\sin(\theta_2 - \theta_1)| \quad (3.13)$$

where  $\mathcal{C}$  is a complex phase factor. The details of this calculation are disclosed in Appendix A. This result is intuitively pleasing because it formulates the cross-correlation in terms of the scanning geometry. As the angle of attack between two projections decreases, the cross-correlation increases because the probe beams cover a growing common region within the scattering object.

### 3.3 Backprojection Image Statistics

Let us now turn our attention to the first and second moments of the reflectance image formed by applying the discrete backprojection operator to the set of magnitude projections  $|\mathbf{R}(r, \theta)|^2$  of  $s(x, y)$ . In the semi-discrete case let  $A_{bp}(x, y : N)$  be the backprojected image formed by using  $N$  equiangular projections. Thus

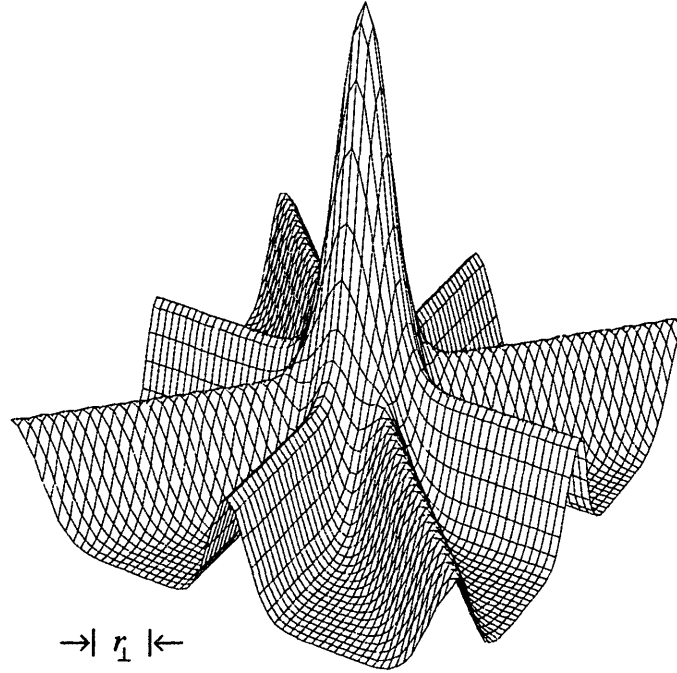
$$A_{bp}(x, y : N) = \sum_{n=0}^{N-1} \frac{\pi}{N} \left| \mathbf{R}\left(x \cos \frac{\pi}{N} n + y \sin \frac{\pi}{N} n, \frac{\pi}{N} n\right) \right|^2. \quad (3.14)$$

The semi-discrete mean image is then

$$\langle A_{bp}(x, y : N) \rangle = \frac{1}{\sqrt{2\pi r_\perp^2}} \sum_{n=0}^{N-1} \frac{\pi}{N} \mathfrak{R}_{\frac{\pi}{N} n} [g(x, y) \star f(x, y)]. \quad (3.15)$$

It would be instructive to write this result in the form of  $f(x, y)$  convolved with a point-spread-function (PSF). By setting  $f(x, y) = \delta(x - x_o, y - y_o)$  and using the property  $\mathfrak{R}_\theta[f \star g] = \mathfrak{R}_\theta f \star \mathfrak{R}_\theta g$  it is easily shown that (3.15) represents a shift-invariant linear system. Thus, we may alternately write

$$\langle A_{bp}(x, y : N) \rangle = \frac{1}{\sqrt{2\pi r_\perp^2}} f(x, y) \star G_{bp}(x, y : N) \quad (3.16)$$

Figure 3.3: Normalized Mean Backprojection Image PSF,  $G_{bp}(x, y : 4)$ 

where

$$\begin{aligned}
 G_{bp}(x, y : N) &= \sum_{n=0}^{N-1} \frac{\pi}{N} [\Re_{\frac{\pi}{N}n} g(x', y')] (x \cos \frac{\pi}{N}n + y \sin \frac{\pi}{N}n) \\
 &= \frac{\pi}{N} \sum_{n=0}^{N-1} \frac{1}{\sqrt{\pi r_{\perp}^2 / 2}} e^{-2(x \cos \frac{\pi}{N}n + y \sin \frac{\pi}{N}n)^2 / r_{\perp}^2} \quad (3.17)
 \end{aligned}$$

represents the  $N$  dependent PSF of the mean image. Figure 3.3 shows a surface plot of the normalized PSF for  $N = 4$  projections.

As  $N$  grows without bound, the semi-discrete backprojection case approaches the continuous case as a limit. Define  $A_{bp}(x, y)$  to be the image produced by the continuous backprojection operator:

$$A_{bp}(x, y) = \mathcal{B}[|\mathbf{R}(r, \theta)|^2]$$

$$= \int_0^\pi d\theta |\mathbf{R}(r, \theta)|^2.$$

The mean of  $A_{bp}(x, y)$  is found to be

$$\begin{aligned} \langle A_{bp}(x, y) \rangle &= \langle \mathcal{B}[|\mathbf{R}(r, \theta)|^2] \rangle \\ &= \mathcal{B}\langle |\mathbf{R}(r, \theta)|^2 \rangle \\ &= \frac{1}{\sqrt{2\pi r_\perp^2}} \mathcal{B}\mathfrak{R}[g(x, y) \star f(x, y)] \\ &= \frac{1}{\sqrt{2\pi r_\perp^2}} \frac{1}{\sqrt{x^2 + y^2}} \star g(x, y) \star f(x, y). \end{aligned} \quad (3.18)$$

Thus, the point-spread-function (PSF) of the mean of this narrow-beam tomographic scheme under backprojection reconstruction is  $g(x, y) \star (x^2 + y^2)^{-1/2}$ . Therefore, continuous backprojection reconstruction alone cannot fully resolve  $f(x, y)$  within the limitations imposed by the narrow-beam approach.

The reconstructed image noise strength is measured by the image covariance. Let  $K_{AA_{bp}}(x_1, y_1; x_2, y_2 : N)$  designate the covariance of the image  $A_{bp}(x, y : N)$  formed by semi-discrete backprojection. Using complex-Gaussian moment factoring the covariance may be simplified to the following form:

$$\begin{aligned} K_{AA_{bp}}(x_1, y_1; x_2, y_2 : N) \\ = \frac{\pi^2}{N^2} \sum_{n=0}^{N-1} \sum_{i=0}^{N-1} \left| \left\langle \mathbf{R}_{\frac{\pi}{N}n}(x_1 \cos \frac{\pi}{N}n + y_1 \sin \frac{\pi}{N}n) \mathbf{R}_{\frac{\pi}{N}i}^*(x_2 \cos \frac{\pi}{N}i + y_2 \sin \frac{\pi}{N}i) \right\rangle \right|^2. \end{aligned} \quad (3.19)$$

This result is equal to the summation of the magnitude-squared values of the cross-correlation between the received signal fields  $\mathbf{R}$  corresponding to the scan lines  $(r_n, \theta_n)$  and  $(r_i, \theta_i)$

Consider the case of identical indices within the double-summation. The double summation will collapse to a sum of the magnitude-squared equiangle cross-

correlations. Hence, this component of the covariance becomes

$$\frac{\pi^2}{N^2} \sum_{n=0}^{N-1} \frac{1}{2\pi r_{\perp}^2} \exp \left\{ -[(x_2 - x_1) \cos \frac{\pi}{N} n + (y_2 - y_1) \sin \frac{\pi}{N} n]^2 / r_{\perp}^2 \right\} \times \\ [\Re f]^2 \left( \frac{x_2 + x_1}{2} \cos \frac{\pi}{N} n + \frac{y_2 + y_1}{2} \sin \frac{\pi}{N} n, \frac{\pi}{N} n \right).$$

For non-identical indices we have the case of unequal projection angle cross-correlations within the double-summation. Thus, the semi-discrete covariance may be approximated by the sum of these two results:

$$K_{AA_{bp}}(x_1, y_1; x_2, y_2 : N) \approx \\ \frac{\pi^2}{N^2} \sum_{n=0}^{N-1} \frac{1}{2\pi r_{\perp}^2} \exp \left\{ -[(x_2 - x_1) \cos \frac{\pi}{N} n + (y_2 - y_1) \sin \frac{\pi}{N} n]^2 / r_{\perp}^2 \right\} \times \\ [\Re f]^2 \left( \frac{x_2 + x_1}{2} \cos \frac{\pi}{N} n + \frac{y_2 + y_1}{2} \sin \frac{\pi}{N} n, \frac{\pi}{N} n \right) + \\ \frac{\pi^2}{N^2} \sum_{n=0}^{N-1} \sum_{i=0, i \neq n}^{N-1} \frac{4}{\sin^2 \frac{\pi}{N} (n-i)} f^2(x^{\oplus}(r_1, \frac{\pi}{N} i; r_2, \frac{\pi}{N} n), y^{\oplus}(r_1, \frac{\pi}{N} i; r_2, \frac{\pi}{N} n)), \quad (3.20)$$

where

$$r_1 = x_1 \cos \frac{\pi}{N} i + y_1 \sin \frac{\pi}{N} i, \quad (3.21)$$

$$r_2 = x_2 \cos \frac{\pi}{N} n + y_2 \sin \frac{\pi}{N} n. \quad (3.22)$$

The reconstructed image variance  $\text{var}_{AA_{bp}}(x, y : N)$  can be easily obtained from the above covariance expression by setting  $(x_1, y_1) = (x_2, y_2) = (x, y)$ . Under this restriction the point  $(x^{\oplus}(r_1, \theta_1; r_2, \theta_2), y^{\oplus}(r_1, \theta_1; r_2, \theta_2))$  reduces to  $(x, y)$  giving

$$\text{var}_{AA_{bp}}(x, y : N) \approx \frac{\pi^2}{N^2} \sum_{n=0}^{N-1} \frac{1}{2\pi r_{\perp}^2} [\Re f]^2 \left( x \cos \frac{\pi}{N} n + y \sin \frac{\pi}{N} n, \frac{\pi}{N} n \right) + \\ \frac{\pi^2}{N^2} f^2(x, y) \sum_{n=0}^{N-1} \sum_{i=0, i \neq n}^{N-1} \frac{4}{\sin^2 \frac{\pi}{N} (n-i)}. \quad (3.23)$$

Hence, the variance of the reconstructed image consists of two terms, one proportional to  $f^2(x, y)$  and the other proportional to the backprojected image of the *square* of the Radon transform of  $f(x, y)$ .

The above covariance and variance expressions are complicated and provide partial insight into the behavior of these quantities in terms of  $f(x, y)$  and  $N$ , the number of projections per reconstruction. Further analysis has not yet yielded simpler forms for arbitrary  $f(x, y)$  and  $N$ . Therefore, we proceed with an analysis in the next section by fixing a bandlimited low-contrast model for  $f(x, y)$  and predicting image signal-to-noise performance in terms of  $N$ . The low-contrast reflectance model is a reasonable approximation for many objects of interest because it separates the reflectance variations which describe distinguishable surface features from the gross base reflectance which accounts for a majority of the speckle induced noise. Thus, to a first order approximation, the signal-to-noise behavior of a reconstructed image can be described.

### 3.4 Backprojection Image Signal-to-Noise Ratio

To place our analysis in perspective, let us calculate the signal-to-noise ratio of the reconstructed image of a scattering object with a low-contrast reflectance function of the form  $f(x, y) = F + \delta f(x, y)$  where  $|\delta f(x, y)| \ll F$ . In this model, the term  $\delta f(x, y)$  describes the variation in reflectivity due to surface features, while the  $F$  term accounts for the overall average reflectance. Since all interesting objects are of limited spatial extent, (i.e., bounded) assume for the sake of simplicity that the object has negligible reflectance outside a  $R_D$  meter radius disk centered at the origin. Furthermore, assume  $\delta f(x, y)$  is a  $b$ -band limited function, viz. the spatial frequency spectrum of  $\delta f(x, y)$  negligible for  $|(f_x, f_y)| > b$ . This is a natural assumption to make

since most objects of interest have surface feature variations which are smooth on a small enough scale. We will find it useful to let  $\chi_f$  designate the indicator function for  $f(x, y)$ , i.e.,

$$\chi_f(x, y) = \begin{cases} 0 & \text{if } f(x, y) = 0 \\ 1 & \text{otherwise.} \end{cases} \quad (3.24)$$

Thus the indicator function for our scattering object is a  $R_D$  meter radius unit height disk.

The signal-to-noise ratio (SNR) under semi-discrete backprojection reconstruction is defined as follows

$$\begin{aligned} \text{SNR} &= \frac{[\text{mean reconstructed signal}]^2}{\text{mean squared noise strength}} \\ &= \frac{\frac{1}{2\pi r_\perp^2} [\delta f(x, y) \star G_{bp}(x, y : N)]^2}{\text{var}_{AA_{bp}}(x, y : N)} \\ &\approx \frac{(\delta f(x, y) \star G_{bp}(x, y : N))^2}{\frac{\pi^2}{N^2} F^2 \sum_{n=0}^{N-1} [\Re_{\frac{\pi}{N}n} \chi_f]^2 (x_1 \cos \frac{\pi}{N}n + y_1 \sin \frac{\pi}{N}n) + \frac{\pi^2}{N^2} 2\pi r_\perp^2 F^2 \sum_{n=0}^{N-1} \sum_{i=0, i \neq n}^{N-1} \frac{4}{\sin^2 \frac{\pi}{N}(n-i)}} \end{aligned}$$

where we have used  $f(x, y) \approx F$  in the expression for the variance. For  $N > 10$  the double summation in the denominator can be approximated by  $\frac{4}{3}N^3$  giving

$$\text{SNR} \approx \frac{[\delta f(x, y) \star G_{bp}(x, y : N)]^2}{\frac{\pi^2}{N^2} F^2 \sum_{n=0}^{N-1} [\Re_{\frac{\pi}{N}n} \chi_f]^2 (x_1 \cos \frac{\pi}{N}n + y_1 \sin \frac{\pi}{N}n) + 2\pi r_\perp^2 \frac{\pi^2}{N^2} \frac{4}{3} N^3 F^2}. \quad (3.25)$$

Recall that  $\delta f(x, y)$  is  $b$ -band limited. Therefore, the appropriate number of projections to fully recover  $\delta f(x, y)$  is  $\pi q$  where  $2q + 1$  is the number of points specified by the one-dimensional Shannon sampling theorem for the proper sampling and recovery of any one projection. For a  $R_D$  meter bandlimited disk,

$$\begin{aligned} q &= (\text{disk radius (m)}) \div (\text{sampling interval (m)}) \\ &= R_D \text{ (m)} / (2b)^{-1} \text{ (m)} \\ &= 2bR_D \text{ (dimensionless)}. \end{aligned}$$

Thus, we set  $N = 2\pi bR_D$ . Furthermore, we fix the beam width equal to the size of the smallest detail on the bandlimited disk, i.e.,  $r_\perp = 1/b$ . Therefore, the signal-to-noise ratio becomes

$$\begin{aligned} \text{SNR} &\approx \frac{[\delta f(x, y) \star G_{bp}(x, y : N)]^2}{\frac{F^2}{2b\mathcal{R}} \left( \sum_{n=0}^{N-1} \frac{\pi}{N} [\Re_{\frac{\pi}{N}n} \chi_f]^2 (x_1 \cos \frac{\pi}{N}n + y_1 \sin \frac{\pi}{N}n) + \frac{4}{3}\pi^4 \right)} \\ &= \frac{2N[\delta f(x, y) \star G_{bp}(x, y : N)]^2/\pi}{F^2 \left( \sum_{n=0}^{N-1} \frac{\pi}{N} [\Re_{\frac{\pi}{N}n} \chi_f]^2 (x_1 \cos \frac{\pi}{N}n + y_1 \sin \frac{\pi}{N}n) + \frac{32}{3}\pi^4 R_D^2 \right)}. \end{aligned} \quad (3.26)$$

Note that the squared term in the numerator and the summation (backprojection) term in the denominator both approach finite limiting values as  $N$  grows without bound.

A computer was used to calculate the above SNR quantity for a  $R_D = 1$  meter radius disk. During the calculation, the bracketed term within the numerator was approximated by  $\delta f(x, y)$  times the area under  $G_{bp}(x, y : N)$ . This is valid under our assumption that  $b$  is less than or equal to the spatial bandwidth of  $G_{bp}(x, y : N)$ . The resulting SNR was found to have a radial profile which did not vary in respect to rotation about the disk center. Therefore, Figure 3.4 presents a radial plot of (3.26) normalized by the factor  $\delta f^2(x, y)/F^2$  for a family of  $N$  values. For a fixed number of projections the above SNR equation scales independently with respect to  $R_D$ . Therefore, this set of curves can be interpreted as the normalized SNR of the backprojection reconstruction of a  $R_D$  meter disk where the abscissa scale is now in terms of  $r/R_D$ .

Note that the SNR performance is nearly constant versus radial distance from the center of the disk. Thus, the disk image SNR is proportional to the number of projections required to fully reconstruct  $f(x, y)$  under our bandwidth constraint. This result stands in contrast to ordinary speckle-imaging systems which coherently combine measurements during pixel formation, achieving SNR's equal to one [28].



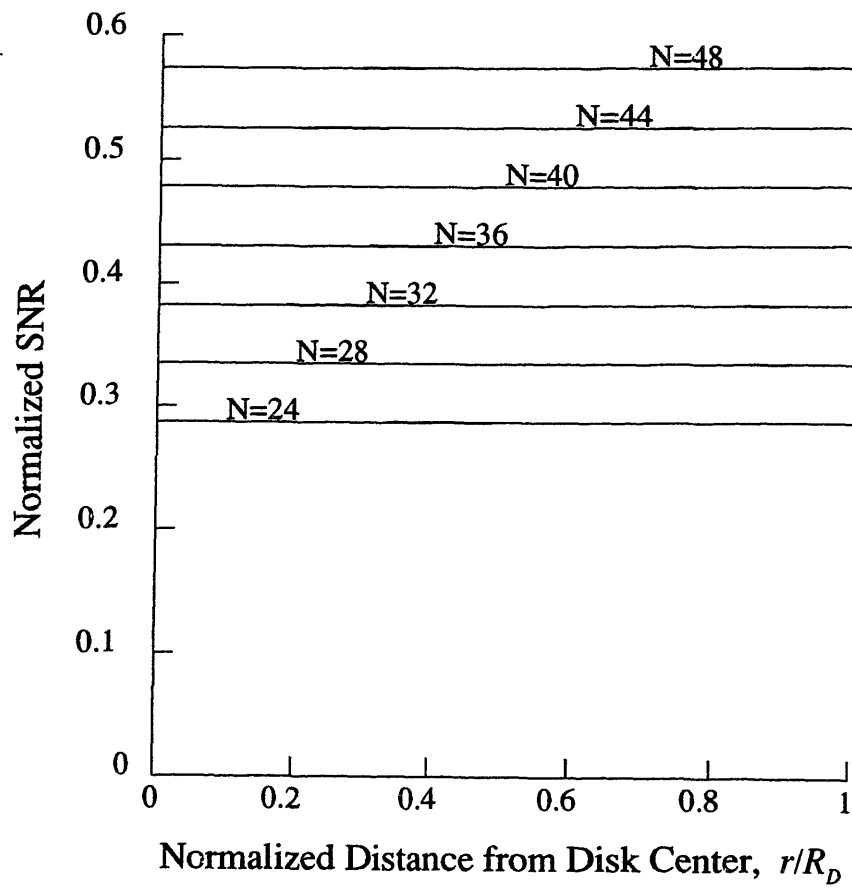


Figure 3.4: Backprojection SNR Performance

However, even in our case at  $\delta f^2(x, y)/F^2 = 1$ , we do not obtain a unity SNR until  $N \geq 84$ . Considering the slow SNR rise vs.  $N$ , and the poor resolving power of backprojection reconstruction, this tomographic speckle-imaging technique offers relatively substandard performance, even for the larger sized projection sets of  $N \approx 200$ , the typical number of projections recorded by a commercial CAT scanner.

### 3.5 Filtered Backprojection Image Statistics

Now consider a similar analysis for semi-discrete filtered backprojection processing. In this case we will prefilter every projection before performing the backprojection sum. Let  $A_{fbp}(x, y : N)$  be the backprojected image of the reflectance formed by using  $N$  equiangular filtered projections. Thus

$$A_{fbp}(x, y : N) = \sum_{n=0}^{N-1} \frac{\pi}{N} \left[ \mathcal{F}^{-1} \left\{ |\varrho| \times \mathcal{F} \left[ |\mathbf{R}(r', \frac{\pi}{N}n)|^2 \right] \right\} \right] (x \cos \frac{\pi}{N}n + y \sin \frac{\pi}{N}n) \quad (3.27)$$

where the expression within the outer brackets represents the filtered backprojections as a function of  $r$ , and  $r$  is then set equal to  $x \cos \frac{\pi}{N}n + y \sin \frac{\pi}{N}n$  under the backprojection sum. In order to simplify the notation during further discussions, let the symbol  $\mathcal{H}[p(r)]$  denote the filtering operation  $\mathcal{F}^{-1} \{ |\varrho| \times \mathcal{F}[p(r)] \}$ . The semi-discrete mean image is then

$$\begin{aligned} \langle A_{fbp}(x, y : N) \rangle &= \frac{1}{\sqrt{2\pi r_{\perp}^2}} \times \\ &\sum_{n=0}^{N-1} \frac{\pi}{N} \left[ \mathcal{F}^{-1} \left\{ |\varrho| \times \mathcal{F} \left[ [\Re_{\frac{\pi}{N}n}(g(x', y') \star f(x', y'))](r')] \right] \right\} \right] (x \cos \frac{\pi}{N}n + y \sin \frac{\pi}{N}n) \\ &= \sum_{n=0}^{N-1} \frac{\pi}{N} \mathcal{H}[\Re_{\frac{\pi}{N}n}(g(x', y') \star f(x', y'))](x \cos \frac{\pi}{N}n + y \sin \frac{\pi}{N}n). \end{aligned} \quad (3.28)$$

As in the case of simple backprojection, the mean image PSF  $G_{fbp}(x, y : N)$  for semi-discrete filtered backprojection can be calculated. Thus, we may alternately

write

$$\langle A_{fbp}(x, y : N) \rangle = \frac{1}{\sqrt{2\pi r_{\perp}^2}} f(x, y) \star G_{fbp}(x, y : N) \quad (3.29)$$

where

$$G_{fbp}(x, y : N) = \sum_{n=0}^{N-1} \frac{\pi}{N} g_f(x \cos \frac{\pi}{N} n + y \sin \frac{\pi}{N} n) \quad (3.30)$$

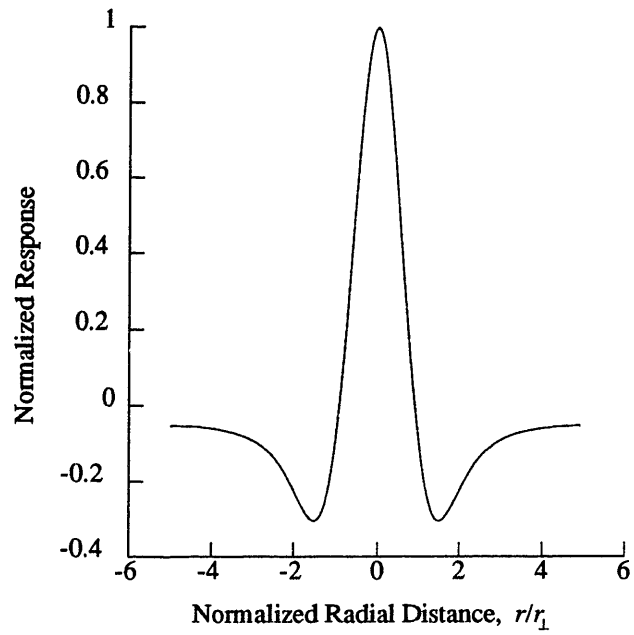
where the function  $g_f(r)$  is equal to

$$\begin{aligned} g_f(r) &= \mathcal{H} \left[ \left[ \mathfrak{R} \frac{\pi}{N} n g(x, y) \right] (r) \right] \\ &= \mathcal{F}^{-1} \left\{ |\varrho| \times \mathcal{F} \left[ \left( 1 / \sqrt{\pi r_{\perp}^2 / 2} \right) e^{-2(r')^2 / r_{\perp}^2} \right] \right\}. \end{aligned} \quad (3.31)$$

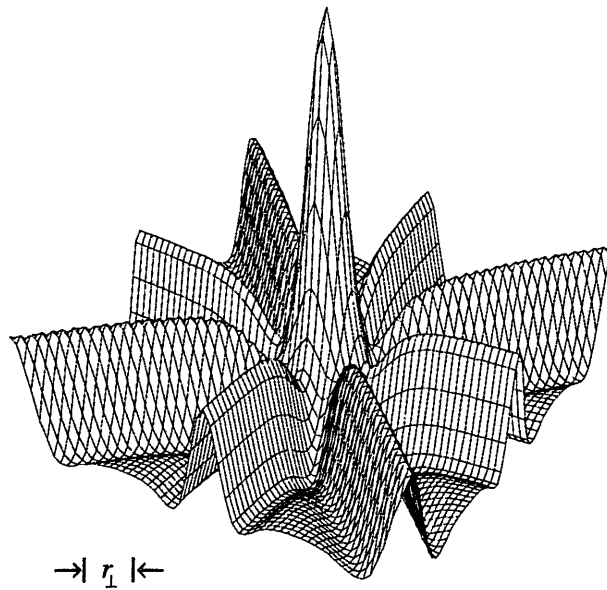
The function  $g_f(r)$  is plotted in Figure 3.5. The width of the central lobe determines the fundamental resolution of the filtered backprojection image reconstruction scheme. Since filtered backprojection is one solution to the inverse Radon transform, as  $N$  grows large and we pass to the continuous case, the PSF for the mean image must be  $g(x, y)$  defined in equation (3.8) within a scale factor. Thus, the fundamental resolution cell size is equal to the width of  $g(x, y)$  which is physically determined by the scanning instrumentation.

The filtered backprojection image noise strength is measured by the reconstructed image covariance. Let  $K_{AA_{fbp}}(x_1, y_1; x_2, y_2 : N)$  designate the covariance of the image  $A_{fbp}(x, y : N)$  formed by  $N$  equiangular semi-discrete filtered backprojection reconstruction. Recalling that the filtering operation  $\mathcal{H}$  is performed with respect to the radial projection variable  $r$ , the filtered backprojection covariance may be written as

$$\begin{aligned} &K_{AA_{fbp}}(x_1, y_1; x_2, y_2 : N) \\ &\approx \frac{1}{2\pi r_{\perp}^2} \frac{\pi}{N} \sum_{n=0}^{N-1} \frac{\pi}{N} \mathcal{H}_{r_2} \left[ \mathcal{H}_{r_1} \left[ e^{-(r_2 - r_1)^2 / r_{\perp}^2} [\mathfrak{R} f]^2 \left( \frac{r_2 + r_1}{2}, \frac{\pi}{N} n \right) \right] \right. \\ &\quad \left. (x_1 \cos \frac{\pi}{N} n + y_1 \sin \frac{\pi}{N} n) \right] (x_2 \cos \frac{\pi}{N} n + y_2 \sin \frac{\pi}{N} n) + \end{aligned}$$



(a)



(b)

Figure 3.5: Filtered Backprojection Mean Image PSF (a)  $g_f(r)$ , (b)  $G_{fbp}(x, y : 4)$

$$\frac{\pi^2}{N^2} \sum_{n=0}^{N-1} \sum_{i=0, i \neq n}^{N-1} \frac{4}{\sin^2 \frac{\pi}{N}(n-i)} \mathcal{H}_{r_2} \left[ \mathcal{H}_{r_1} \left[ f^2(\mathbf{x}^\oplus(r_1, \frac{\pi}{N}i; r_2, \frac{\pi}{N}n), \mathbf{y}^\oplus(r_1, \frac{\pi}{N}i; r_2, \frac{\pi}{N}n)) \right] \right. \\ \left. (\mathbf{x}_1 \cos \frac{\pi}{N}n + \mathbf{y}_1 \sin \frac{\pi}{N}n) \right] (\mathbf{x}_2 \cos \frac{\pi}{N}i + \mathbf{y}_2 \sin \frac{\pi}{N}i) \quad (3.32)$$

where the operators  $\mathcal{H}_{r_1}$  and  $\mathcal{H}_{r_2}$  filter with respect to the variables  $r_1$  and  $r_2$  respectively. This expression is valid because the expectation, backprojection and  $\mathcal{H}$  operators are all linear. Thus, the prescription for finding the covariance is to filter the expression within the inner brackets with respect to variables  $r_1$  and  $r_2$  and then replace  $r_1$  and  $r_2$  with the proper cartesian coordinate expansion before performing the sums. The variance of  $A_{fbp}(x, y : N)$  may be obtained from the above expression by setting  $(x_1, y_1) = (x_2, y_2)$  before computing the sums.

The above covariance and variance approximations are complicated and provide little insight into their behavior as  $f(x, y)$  and  $N$  vary. Further analysis has not yielded a simpler form for arbitrary  $f(x, y)$  and  $N$ . Therefore, as in the case with backprojection reconstruction, we have proceeded with the SNR performance analysis of a bandlimited low-contrast disk-like scattering object.

### 3.6 Filtered Backprojection Signal-to-Noise Ratio

For the reasons cited in §3.4, let us calculate the signal-to-noise ratio of a filtered backprojection image reconstruction of a  $R_D$  meter radius disk with a low-contrast reflectance of the form  $f(x, y) = F + \delta f(x, y)$  where  $|\delta f(x, y)| \ll F$ . As before, let  $\delta f(x, y)$  be a  $b$ -band limited function. Thus, the SNR under filtered semi-discrete

equiangular backprojection reconstruction is:

$$\begin{aligned}
 \text{SNR} &= \frac{(\text{mean reconstructed signal})^2}{\text{mean squared noise strength}} \\
 &= \frac{\frac{1}{2\pi r_{\perp}^2} (\delta f(x, y) \star G_{fbp}(x, y : N))^2}{\text{var}_{AA_{fbp}}(x, y : N)} \\
 &\approx \frac{1}{F^2} \cdot \frac{(\delta f(x, y) \star G_{fbp}(x, y : N))^2}{2\pi r_{\perp}^2 \text{var}_{AA_{fbp}}(x, y : N)/F^2} \tag{3.33}
 \end{aligned}$$

where the second term in the above product represents the SNR of a reconstructed  $R_D$  meter radius unit-height disk. This quantity has been numerically evaluated under our bandwidth restriction of  $b = 1/r_{\perp}$  and found to be radially symmetric about the center of the disk within the resolution capabilities of the calculation. Figure 3.6 shows a radial plot of this second term for a family of  $N$  values. Each plot has been normalized by  $\delta f^2(x, y)/F^2$  and the height of the filtered backprojection impulse response  $G_{fbp}(x, y : N)$  to facilitate direct comparison to the backprojection results of §3.4. The  $b$ -bandwidth restriction has been enforced by windowing the  $1/|\rho|$  spatial frequency filtering with a Gaussian function centered on the frequency origin. Again, we have used the relation  $N = 2\pi b R_D$  to relate the number of projections to the image bandwidth. Since (3.33) scales independently with the disk radius for a fixed  $N$ , Figure 3.6 can be interpreted as the normalized SNR of a filtered backprojection reconstruction of a  $R_D$  meter disk where the abscissa scale is in terms of  $r/R_D$ .

It is intuitively pleasing that the SNR increases with the number of projections in light of projection signal processing which would tend to enhance high frequency noise. Observe that as the number of projections increases, a peak appears to grow in height at the edge of the disk. This seems to indicate that image quality is better at the edge than in the disk interior. However, this phenomenon may be a phantom caused by a large spatial frequency filter response at the disk edge drop-off. Furthermore, slight SNR variations appear near the disk center as the number of projections rises

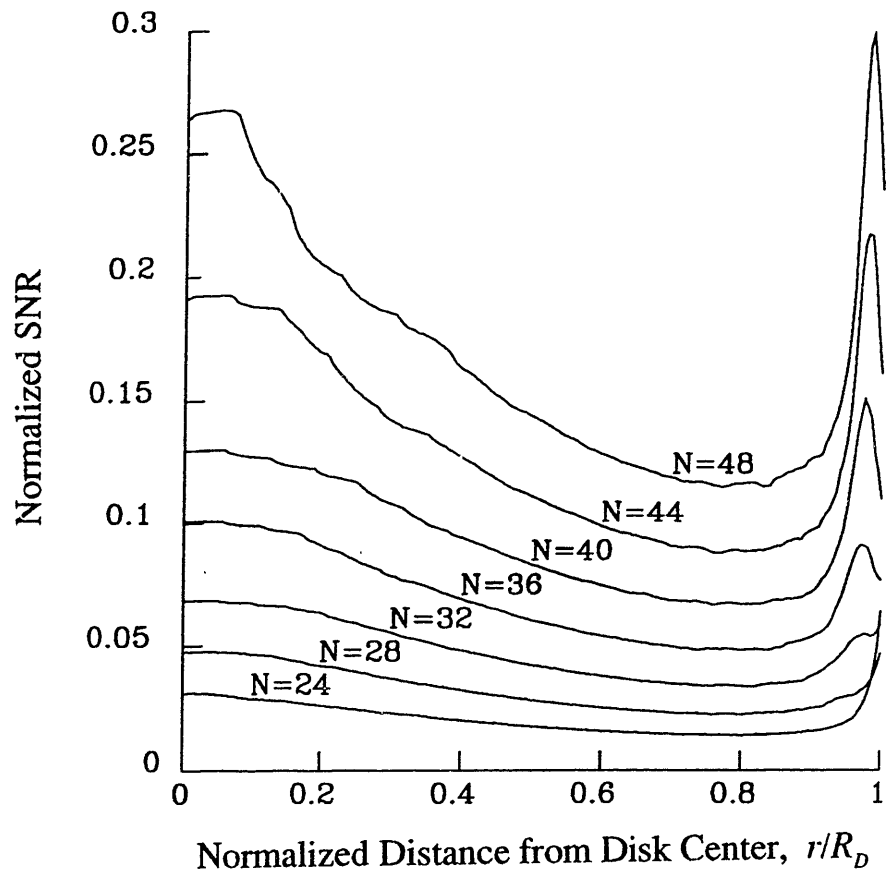


Figure 3.6: Filtered Backprojection SNR Performance

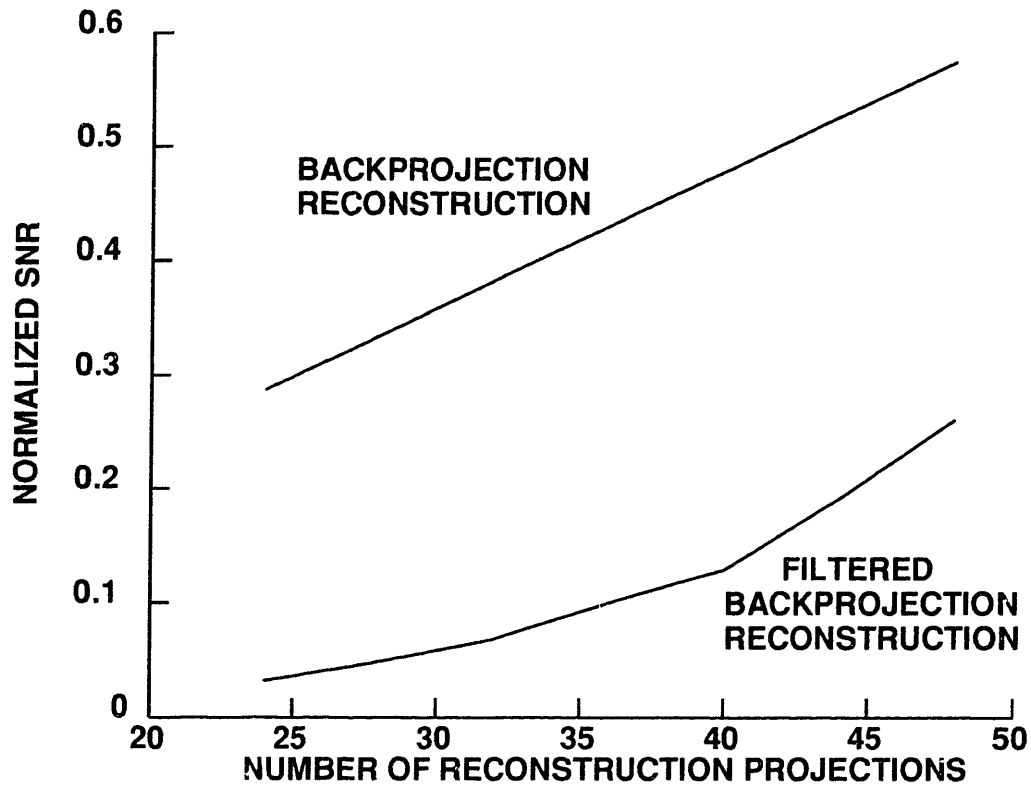


Figure 3.7: SNR Performance Comparison

above 40. This is believed to be caused by resolution limitations within the numerical calculations.

Figure 3.7 plots the normalized disk center SNR for both the backprojected and filtered backprojected reconstructions. Over the set of  $N$ , both reconstructions achieve SNR's of less than one, with filtered backprojection performance lying approximately 8 dB below the backprojection curve. Furthermore, a linear extrapolation carried out upon the central region of the filtered backprojection curve indicates that a unity SNR will be obtained for  $N \approx 480$ , a value much larger than the corresponding backprojection case. However, since both reconstructions have differing resolutions, this



is not a fair comparison. For a non-random  $\delta f(x, y)$ , the image mean squared error (MSE) for both reconstruction techniques breaks down into the variance of the reconstructed low-contrast reflectance,  $\delta \hat{f}(x, y)$ , plus the square of a second bias term. The  $\delta \hat{f}(x, y)$  variance is inversely proportional to  $N$ , while the bias measures the departure of the reconstruction PSF from a delta function, the ideal imaging system PSF. Making the comparison on this basis, the backprojection reconstruction bias term is larger than the corresponding filtered reconstruction term because of the relatively poor backprojection reconstruction resolving power, while the backprojection reconstruction  $\delta \hat{f}(x, y)$  variance is smaller than the corresponding filtered reconstruction contribution because, in this latter quantity, spatial projection filtering emphasizes high frequency noise. Therefore, the SNR advantage of backprojection reconstruction comes at the expense of much poorer resolution (cf. Figure 2.2 (b) and (c) and also [24, Figure 18.]).



## Chapter 4

# RTI Tomographic Imaging Performance

We now turn our attention to the range-resolved laser radar tomography problem originally outlined in chapter 1. In this scenario we use a direct detection laser radar to illuminate a spinning target to obtain a fixed number of range resolved returns which correspond to a set of projections of the target reflectance onto the range axis. Tomographic techniques will then be applied to this semi-discrete range-time-intensity (RTI) record of the target revolution to reconstruct a two-dimensional reflectance image of the three-dimensional target. The goal of this investigation is to examine the performance of this imaging technique.

The discussion in this chapter is organized along three main thrusts. First, we will introduce the concepts necessary to build a mathematical signal model of the imaging problem which will allow us to compute the first and second moments of the reconstructed image. This model incorporates radar-target geometry, electromagnetic propagation, target characteristics, direct detection and finally, tomographic image reconstruction. As in most mathematical models of complex physical processes, we are often forced to adopt approximations during the analysis which degrade accuracy

but provide useful explicit closed-form performance predictions. While such is the case here, we nevertheless hope to develop a theory which will qualitatively satisfy our curiosity concerning the issues and interpretations of the reconstructed RTI images. Here, our ultimate goal in modelling is to quantify the reconstructed image quality in terms of resolution and SNR-like measures.

The second section deals with the calculation of the first and second moments of RTI projections. The emphasis in this chapter will be on the discussion of the assumptions and approximations behind the calculations and a presentation of the results along with their proper interpretation. Full disclosure of every step of the computations is made in Appendix B along with a detailed discussion justifying all assumptions. While this necessitates some duplication in the presentation, it was felt that the reader of this chapter should be spared from the seemingly daunting stream of changes of variables, integrations and transformation operations required to obtain the sought after signal covariances.

In the final section, the results of the two previous sections will be woven together to produce two measures of the reconstructed image quality. The image resolution will be derived from the projection mean, while the image SNR will be fashioned from both the projection mean and variance. A discussion comparing these results with previous experimental results and the companion DTI results of the next chapter will be the scope of a later chapter.

As we begin the process of constructing the RTI imaging model, the most difficult aspect to conceptualize is the specification of a target with arbitrary shape, reflectance and roughness. Therefore, we step back from this general situation and begin by fixing the target shape as spherical. While this action limits the results to a specific case, we still should obtain a qualitative description of the performance in terms of the

laser radar design parameters.

## 4.1 RTI Tomographic Imaging Model

In this section we will construct a model of the RTI imaging system. Model elements and issues will be discussed in the order they are visited by the pulse emitted by the transmitter, beginning with the transmitter beam modulation and propagation, and then, target characterization, direct detection and finally post-detection image processing.

Many features of the direct detection laser radar model are shown in Figure 4.1. The model features a laser radar in which the transmitter and receiver apertures share the same optical axis. We assume the spherical target is at a constant on-axis position in the radar's optical far-field at a distance of  $L$  meters from the transmitter aperture. The rigid target is centered at the origin of the target coordinate frame  $(x, y, z)$  and spinning about the  $z$ -axis at a rate of  $\Omega$  radians/second. On the scale of the transmission wavelength  $\lambda$ , the microscopic surface variations of the target are large and random in nature.

This geometric model is motivated by the tomographic imaging of a rotating satellite from a ground- or space-based laser radar. In this scenario, targets typically 1-10 meters in size spin from 1-60 revolutions per second at range from the radar which can easily exceed 100,000 meters.

### 4.1.1 Transmitter Beam Propagation

The process of measuring a set of target range projections begins with the transmission of a train of short-duration optical illumination pulses. The optical source within the transmitter is a laser which emits a spatially- and temporally-coherent

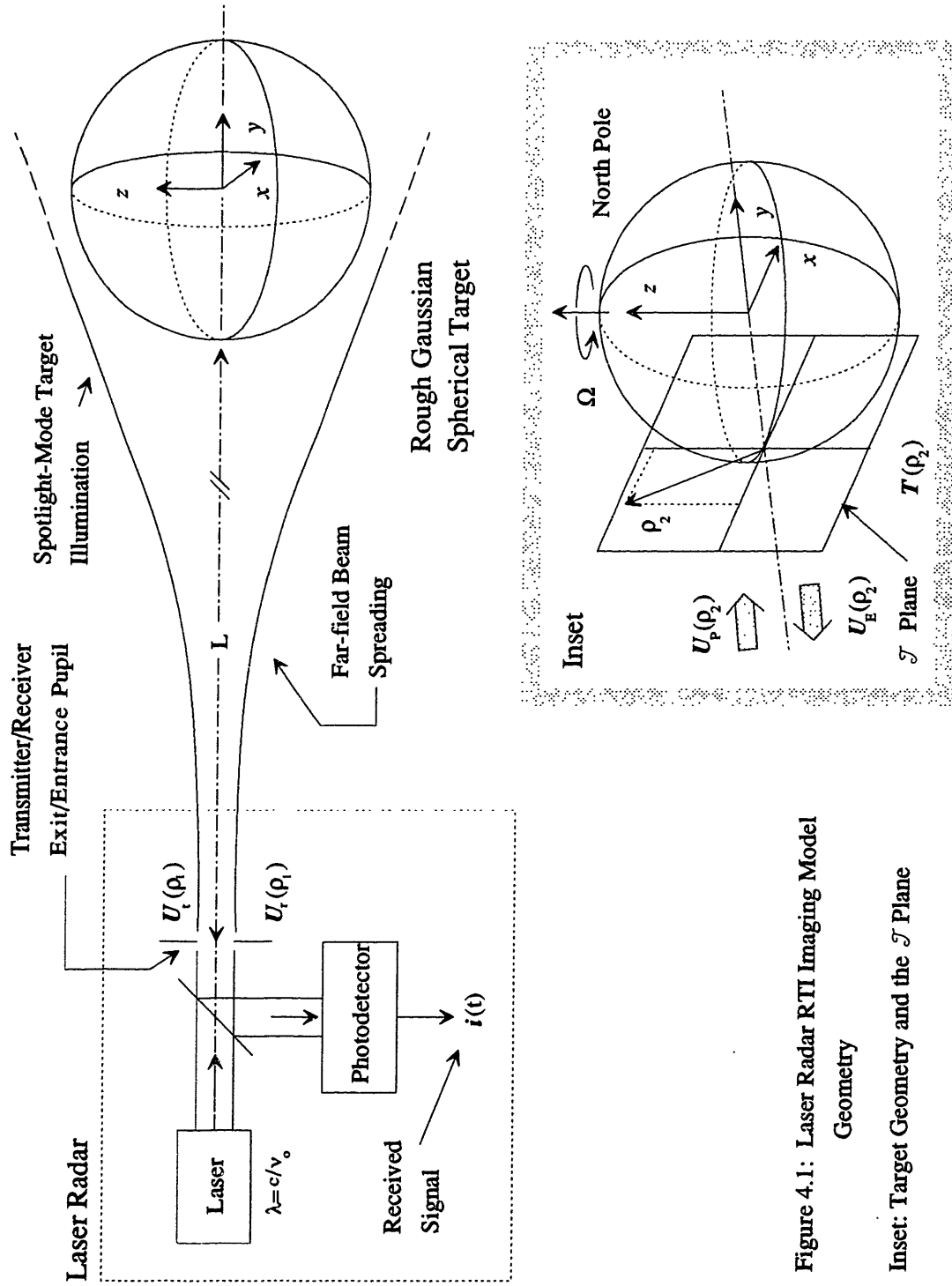


Figure 4.1:

Figure 4.1: Laser Radar RTI Imaging Model

Geometry

Inset: Target Geometry and the  $\mathcal{J}$  Plane

linearly polarized monochromatic beam at the fixed frequency of  $\nu_o = c/\lambda$ . The  $n^{\text{th}}$  pulse arriving at the target at time  $t_n$  is formed at the transmitter exit pupil by amplitude modulating the electric field of the  $+y$ -axis traveling wave by the envelope  $\sqrt{s(t - (t_n - L/c))}$ . The retarded time adjustment term  $L/c$  accounts for the time-of-flight from the laser radar to the target. The envelope  $s(t)$  has a peak value of unity at  $t = 0$  and a very narrow width of  $T$  seconds. Since the range resolution will be proportional to the pulse spatial depth,  $cT$ , systems producing useful resolution will require  $T$  to be less than a nanosecond for meter sized targets.

Under the linear polarization assumption, we may represent the electromagnetic field strength of the  $n^{\text{th}}$  pulse exiting the transmitter pupil by using the complex scalar description [29, Chapter 3]

$$\mathbf{U}_t(\vec{\rho}_1, t) = \sqrt{P_T} \boldsymbol{\xi}_T(\vec{\rho}_1) \sqrt{s(t - (t_n - L/c))} \quad (4.1)$$

where  $\mathbf{U}_t(\vec{\rho}_1, t)$  is proportional to the complex scalar envelope of the outgoing electromagnetic wave,  $P_T$  is the peak transmitter power and  $\boldsymbol{\xi}_T(\vec{\rho}_1)$  is the normalized complex transmitter spatial mode (antenna pattern) within the exit pupil plane spanned by the two-dimensional reference vector  $\vec{\rho}_1$ , i.e.,

$$\int_{\text{Pupil}} d\vec{\rho}_1 |\boldsymbol{\xi}(\vec{\rho}_1)|^2 = 1. \quad (4.2)$$

Therefore, the optical power launched to the target in the  $n^{\text{th}}$  pulse is equal to  $P_T s(t - (t_n - L/c))$ .

Often the large lasers encountered in the laboratory or in an industrial setting have an aperture beam intensity profile which is bell shaped. From the point of view of a tractable mathematical model which approximates the performance of manufactured optical systems, we will assume the illumination produced by the transmitter takes

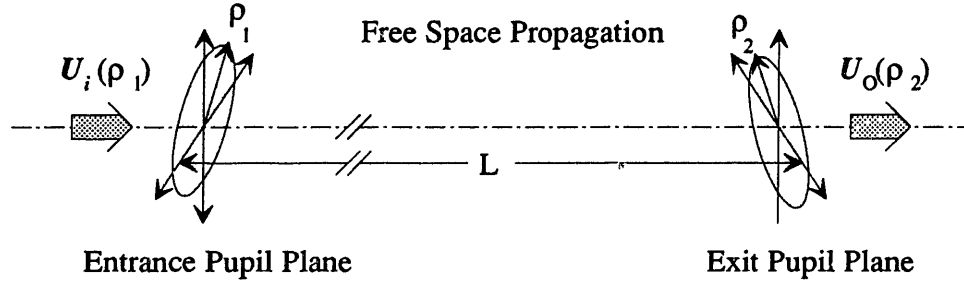


Figure 4.2: Fraunhofer Diffraction Formula Geometry

the form of a collimated Gaussian beam. Therefore, the normalized complex spatial mode at the transmitter exit pupil is

$$\xi_T(\vec{\rho}_1) = \sqrt{\frac{1}{\pi a_o^2}} \exp \left\{ -\frac{|\vec{\rho}_1|^2}{2a_o^2} \right\} \quad (4.3)$$

The beam is considered to have a nominal radius of  $a_o$  meters within the exit pupil plane.

As the laser light propagates through free-space toward the target, the beam characteristics begin to change. In our far-field paraxial case, this evolution in terms of the complex spatial mode can be characterized by the Fraunhofer diffraction formula [29]

$$U_o(\vec{\rho}_2, t) = \underbrace{\sqrt{P_T} \frac{1}{j\lambda L} \exp \left\{ jkL + j\frac{k|\vec{\rho}_2|^2}{2L} \right\}}_{\text{Output Field Spatial Mode}} \hat{\xi}_i(\vec{\rho}_2/\lambda L) \sqrt{s(t - \sqrt{L^2 + |\vec{\rho}_2|^2}/c)} \quad (4.4)$$

where  $ka_o^2/L \ll 1$ . Referring to the entrance-exit pupil diagram of Figure 4.2, we see that the Fraunhofer diffraction formula specifies the output field  $U_o(\vec{\rho}_2, t)$  contained in the exit pupil at time  $t$  in terms of the two-dimensional *spatial* Fourier transform  $\hat{\xi}_i$  of the input spatial mode pattern  $\xi_i(\vec{\rho}_1)$  within the entrance pupil and the time



retarded field modulation  $\sqrt{s(t - \sqrt{L^2 + |\vec{\rho}_2|^2}/c)}$  riding upon the spherical wavefront striking the exit pupil plane. Note that the input field spatial mode  $\xi_i(\vec{\rho}_1)$  is defined as a function of the position vector  $\vec{\rho}_1$  lying in the entrance pupil while the output field  $U_o(\vec{\rho}_2, t)$  is a function of the position vector  $\vec{\rho}_2$  spanning the exit pupil. Both position vectors are understood to be perpendicular to the propagation axis of the electromagnetic wave. The Fraunhofer diffraction formula is only valid when the entrance–exit pupil separation distance,  $L$ , is much greater than the entrance aperture area times the wavenumber. This is certainly the case for imaging system operation at large distances, such as missions performed on earth orbiting satellites from the ground.

Applying this relation to the collimated Gaussian beam at the transmitter exit pupil, we find the probe beam  $U_P(\vec{\rho}_2, t)$  defined on the plane  $\mathcal{T}$  touching the target surface  $L$  meters from the exit pupil to be

$$U_P(\vec{\rho}_2, t) = \sqrt{\frac{P_T}{\pi a_L^2}} \sqrt{s(t - t_n)} \exp \left\{ jkL + j\frac{k|\vec{\rho}_2|^2}{2L} - j\frac{\pi}{2} \right\} \underbrace{\exp \left\{ -\frac{|\vec{\rho}_2|^2}{2a_L^2} \right\}}_{\text{Gaussian Spatial Mode}}. \quad (4.5)$$

Note that the probe beam striking the target is also Gaussian and the parameter  $a_L = L/ka_o$  is the transmitted beam radius at the target site. This parameter is directly proportional to the radar–target separation distance  $L$  and inversely proportional to the transmitter exit pupil size.

In a typical imaging scenario, we will be illuminating a target with spatial dimensions on the order of meters over a radar–target separation distance in excess of 100 kilometers. Therefore, the  $|\vec{\rho}_2|$  dependence within the retarded time term has been neglected in favor of the much larger radar–target separation distance  $L$ . This approximation forces the pulse modulation to apparently propagate to the target

on a plane wave rather than on the nearly flat spherical wavefronts which actually strike the  $T$ -plane. However, after considering the pulse range depth and paraxial propagation, the error is very small.

### 4.1.2 Target Characterization

Consider the scenario of a spatially- and temporally-coherent monochromatic optical wave striking a fixed surface. For a smooth, gently rolling mirror-like surface, the reflected wavefront will suffer from a curvilinear spatial distortion which matches the rolling surface shape. The reflected return from these so called *specular* surfaces maintain spatial- and temporal-coherence. However, in most situations, surfaces are not highly polished but are rather rough when compared to the wavelength of the illuminating laser. These *diffuse* surfaces are characterized by a seemingly random jumble of microscopic surface relief features riding on the gross macroscopic target shape. These diffuse surface characteristics cause spatial decorrelation in target returns.

Imagine then what an observer separated some distance from the diffuse surface sees as he peers at the illuminated target. As long as the microscopic surface roughness is nearly spatially incoherent over the surface, each exposed scattering site will return an optical contribution which has an unpredictable random phase when compared to the return from other sites. The reason for this decorrelation is the variance in the optical path length as the scattering site is relocated over the rough surface. Therefore, since the path length to any individual scattering site will experience a variation of well over a wavelength, the return phase will be uniformly distributed over a wavelength.

The electromagnetic return field from each exposed scattering site will interfere upon reaching the observer's eye. Because the total return is the sum of the electric

fields from a large number of sites with statistically independent propagation path lengths, the distribution of this return will tend toward circulo-complex Gaussian, via the Central limit theorem. Since the human eye senses *intensity*, the observer will experience a return fade if the individual scattered contributions interfere destructively, otherwise, a very bright return will be seen if constructive interference occurs.

A pattern of constructive and destructive interference regions will be spatially distributed over the image plane occupied by the observer. An intensity detector will show this distribution as a haphazard marbled pattern of light and dark patches called speckle. The size, shape and possible movement and evolution of these light or dark patches, or speckle lobes, will depend upon the illumination wavelength, observer-target separation, gross target shape and dynamics, and of course, the microscopic surface roughness characteristics. It is the goal of this subsection to develop a mathematical description of the spherical RTI target which will lead to a statistical characterization of speckle at the laser radar receiver.

Consider the task of calculating the return echo from the illuminated target. The spatial distribution of the surface reflectivity over the target will determine the return magnitude while the target shape and surface roughness will determine the return phase. Thus, the overall return in coherent systems is not only determined by the reflectivity but also by the *macroscopic* target shape and *microscopic* surface roughness. In these situations, the adoption of a *complex* statistical reflectivity satisfies the dual requirements of magnitude and phase.

To develop greater insight into these issues, consider a surface test patch on the illuminated portion of the target. The patch size is chosen small enough so that the target reflectivity  $\rho$  varies little over the patch extent. The entire patch appears to the human eye as have a shading which corresponds to the value of  $\rho$ . Therefore,

the parameter  $\rho$  becomes the power (intensity) ratio of the reflected echo to the illumination strength for any scattering site within the patch.

The joint issues of target shape and surface roughness can be separated by considering the following scenario. We could imagine constructing an actual target by impressing the microscopic surface roughness features onto a thin skin and then wrapping this skin around the nominal target topology the way one would sew a leather skin over the core of a baseball. Let the function  $h(x, y, z)$  be the skin thickness or height above the point  $(x, y, z)$  on the nominal target topology. The set of  $(x, y, z)$  are now understood to define precisely what is meant by the gross target shape and  $h(x, y, z)$  represents the surface roughness. To give a sense of scale,  $h(x, y, z)$  may have a maximum value of no more than a few wavelengths while the target shape reflects the macroscopic target extent. For targets of practical interest, this may be on the order of meters.

The receiver combines the phase contributions from all the exposed scattering sites after the return has travelled to the radar. The phase contribution from each scattering site is computed by simply expressing the round trip distance to the radar in terms of wavelengths. The above target model naturally breaks each phase contribution into two components. The first component is due to the macroscopic distance between the laser radar and the surface defined by the target shape. The second component is due to the intervening material defined by  $h(x, y, z)$  lying above the target shape. In the following model for target reflectivity, we will separately deal with the phase contributions caused by surface roughness and target shape.

Any credible description of target reflectivity must take into account the time dependent issues of intensity reflectance, target shape and target surface roughness as prescribed above. We will deal with these issues by developing an effective multi-

plicative target reflectivity model which is positioned on the  $\mathcal{T}$ -plane, easing future propagation calculations. Note that range depth information will be lost by collapsing the three-dimensional target reflectivity onto the  $\mathcal{T}$ -plane. However, in §4.2, this information will be restored. Therefore, let the complex target reflectivity,  $\mathbf{T}$ , at the point specified by the position vector  $\vec{\rho}_2$  lying in the  $\mathcal{T}$ -plane at time  $t$  be:

$$\mathbf{T}(\vec{\rho}_2, t) \approx \underbrace{\sqrt{\rho(\vec{\rho}_2, t)}}_{\text{1st}} \underbrace{\exp\{-|\vec{\rho}_2|^2/a_T^2\}}_{\text{2nd}} \underbrace{\exp\{jk|\vec{\rho}_2|^2/R_T\}}_{\text{3rd}} \underbrace{\exp\{2jkh(\vec{\rho}_2, t)\}}_{\text{4th}}. \quad (4.6)$$

The first factor accounts for the reflectivity  $\rho(x, y, z)$  of the target surface projected onto the  $\mathcal{T}$ -plane at time  $t$ . At this point, since we are dealing with field strengths and not intensities, the square-root of the reflectivity must be used. The second factor approximates the circular outline of the sphere in the  $\mathcal{T}$ -plane with a Gaussian window function of nominal radius  $a_T/\sqrt{2}$  meters. Here, one's first instinct would be to use a hard-edged window function for this purpose, but the adoption of the Gaussian guarantees the existence of a closed-form solution after Fraunhofer propagation. At this stage, the Gaussian profile does introduce an erroneous darkening of the limb, but in later calculations this approximation will be relaxed. The third factor is a spherical phase factor which accounts for the wavefront round-trip travel from the  $\mathcal{T}$ -plane to the spherical surface, where  $R_T$  is the target radius of curvature. It is this factor which accounts for the influence of the target shape upon the return phase. The last factor models the phase fluctuations caused by the surface roughness. The function  $h(\vec{\rho}_2, t)$  is understood to be the *effective* elevation of the surface roughness features  $h(x, y, z)$  as they depart from a perfectly smooth spherical target. Since this microscopic terrain appears haphazard in nature,  $h(\vec{\rho}_2, t)$  will be chosen to be a random process. It is this last term which gives rise to speckle at the receiver aperture

It seems reasonable to assume that  $h(\vec{\rho}_2, t)$  can be described by a random process [11, 30, §2.7.2]. Since we will be shortly working with the expectations of the RTI record, we must go further, and specify the first and second moments of the random phase factor  $\exp\{2jkh(\vec{\rho}_2, t)\}$ . Note that it is the second moment which will come into play during the mean RTI record calculation because intensity detection is used to form each projection.

Consider the returns from two patches on the surface of the sphere, each of which are on the order of a wavelength or so in size. From the point of view of the incoming electromagnetic radiation, each diffuse patch resembles a flat plateau-like landscape of microscopic “hills and valleys” which represent the seemingly random surface roughness features. Therefore, the field return from each patch will tend toward a circulo-complex Gaussian random variable via the Central limit theorem. If the patches are separated by a distance of many wavelengths, then we would expect the returns to be uncorrelated. However, as we decrease the patch center separation until the patches begin to overlap, the return correlation should increase. Therefore, we adopt the following description for the first and second moments of the the random phase term  $\exp\{2jkh(\cdot, \cdot)\}$  for the coordinate points  $\vec{\rho}_2$  and  $\vec{\rho}_2'$  and the times  $t$  and  $u$  respectively:

- $\langle \exp\{2jkh(\vec{\rho}_2, t)\} \rangle \approx 0$
- $\langle \exp\{2jkh(\vec{\rho}_2, t)\} \exp\{2jkh(\vec{\rho}_2', u)\} \rangle \approx 0$
- $\langle \exp\{2jkh(\vec{\rho}_2, t)\} \exp\{-2jkh(\vec{\rho}_2', u)\} \rangle \approx \exp\left\{-\frac{|\vec{\rho}_2 - \vec{\rho}_2' + \vec{i} R_T \Omega(t - u)|^2}{\rho_T^2}\right\}$

where  $\vec{i}$  is the unit vector lying along the  $x$ -axis in the  $T$ -plane and the parameter  $\rho_T$  is the surface roughness correlation length. This formulation assumes  $\rho_T \ll a_T$

and  $\rho_T \gtrsim \lambda$ , i.e., the surface roughness correlation length is on the order of a few wavelengths.

The above expectations are justified as follows. The first expectation is simply the average complex phase variation due to surface roughness. For fixed position  $\vec{\rho}_2$  and time  $t$ , the surface height shift from one sample to the next in the ensemble of random skin functions  $h(\vec{\rho}_2, t)$  is well over a wavelength. After taking into account phase wrap around, the phase angle will be uniformly distributed from 0 to  $2\pi$ . Therefore, the mean of this phasor will be  $\mathbf{0}$ . The second expectation is over the product of two of these random phasors, which will likewise have a uniform phase angle and therefore also a phasor mean of  $\mathbf{0}$ . For a surface roughness skin function  $h(\vec{\rho})$  positioned on the  $T$ -plane and undergoing uniform motion along the cross-range axis, the final term models the resulting phase decorrelation with respect to time and space. The skin function velocity is set equal to  $\vec{v}R_T\Omega$ , the velocity of the equatorial target surface passing over the radar line-of-sight. Therefore, this term measures decorrelation in terms of  $\rho_T$  by dividing the distance between the points  $\vec{\rho}_2 + \vec{v}R_T\Omega t$  and  $\vec{\rho}_2' + \vec{v}R_T\Omega u$  by  $\rho_T$ . The final structure of this decorrelation term was arbitrarily chosen to be a Gaussian form.

At this point in the discussion, we must draw attention to a subtle weakness in this reflectivity description which involves the specification of the phase component due to the microscopic surface roughness. The reader may have noticed that the above model describes the effects of surface roughness by specifying an equivalent surface roughness skin function  $h(\vec{\rho}_2, t)$  that is stretched over the projection of the target in the  $T$  plane. Note that the random process  $h(\vec{\rho}_2, t)$  has been fixed to be wide sense stationary with respect to the spatial coordinate  $\vec{\rho}_2$ . The function  $h(\vec{\rho}_2, t)$  is meant to behave as a two-dimensional projection of the path length variation caused by

the actual surface roughness skin function  $h(x, y, z)$  covering the target shape. The problem is that this goal is only partially obtained by the above model for  $\mathcal{T}(\vec{\rho}_2, t)$ .

In order to gain insight into how this discrepancy might occur, consider the following observations about the return from a small test patch on the surface of an actual diffuse spherical target. First, let us choose an orientation in which the laser radar is directly overhead of the patch so that the illuminating wavefronts are parallel to the nominal target surface. Under these conditions, a two-dimensional projection of the surface height fluctuations  $h(x, y, z)$  will exactly model the phase variations caused by the difference between the actual scattering surface and the nominal target shape. Now let the target rotate so that the laser radar illuminates our chosen patch partially from the side. In this case, the radar line-of-sight will cut obliquely across  $h(x, y, z)$  to the underlying nominal target surface. Therefore, the projection of  $h(x, y, z)$  does not accurately model the surface variations. This means that the phase statistics will change because the phase is not only dependent upon  $h(x, y, z)$  but also the angle of incidence between the line-of-sight and the patch normal. In fact, we can expect the surface correlation lengths to shorten while the variance of the apparent surface roughness features increases as the patch rotates towards the target limb.

An additional complication comes in at grazing angles of incidence. In these cases significant shadowing occurs as microscopic peaks in the patch foreground obscure background terrain features along the line-of-sight, perhaps requiring a new definition of the surface correlation length in regions near the limb. Finally, for features constructed of tight radii of curvature, multiple reflections of the electromagnetic wave may result. Taking all these effects into account in a comprehensive scattering theory is difficult, but some progress has been cited in the literature [31, 32, 33]. In the case of a spherical target with a stationary  $h(x, y, z)$ , we would expect the line-



of-sight path length correlation function to change as the position of the test patch moves about the exposed face of the target.

In the above equation for complex target reflectivity, the surface roughness issues associated with variable surface aspect, shadowing and multiple reflections are ignored. Proposed theories taking one or more of these concerns into account result in complicated descriptions which make the expectation calculations extremely unwieldy. Instead, since our immediate goal is a qualitative rather than an exact quantitative understanding, we accept the above approximation with this understanding.

### 4.1.3 Direct Detection

The heart of the RTI receiver is the direct or incoherent optical detector. In modern laser radar systems, the return is collected at the receiver aperture and focused by a telescope upon a photodetector whose electrical output is directly proportional to the optical power striking the device's photosensitive surface. System designers usually choose between multidynode photomultiplier tubes (PMT's) or semiconductor photodiodes for detection depending upon the relative merits of operating wavelength, speed, gain, temperature, complexity and optical and electrical noise figure.

Figure 4.3 shows a block diagram of an abbreviated photodetector model which incorporates the bandwidth, gain and noise issues. In this model, incident light at wavelength  $\lambda$  and short-time-average power  $P(t)$  (Watts) strikes the photosensitive surface of the ideal photodetector. According to quantum mechanics, photon arrivals will be described by a Poisson point process with an event rate of  $P(t)/h\nu_o$ , where  $h$  is Planck's constant and  $\nu_o = c/\lambda$ . Every photon will either form an electron-hole pair in the depletion region of a semiconductor device or cause the emission of a photoelectron from the photocathode of a PMT with probability  $\eta$ , the photodetector quantum

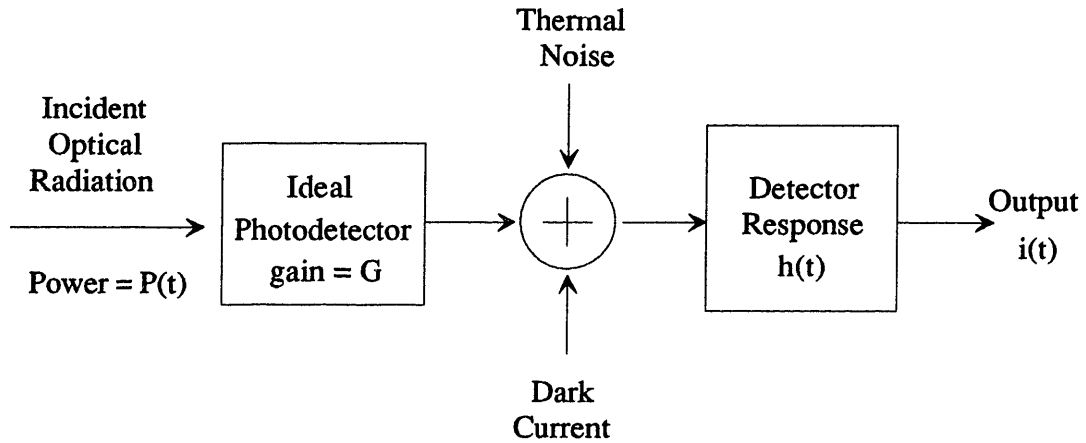


Figure 4.3: Photodetector Model

efficiency. In devices with gain, the avalanche multiplication mechanism produces a randomly sized burst of photoconductors for each photoelectrical conversion event. The number of burst carriers from event to event is statistically independent and has a fixed average of  $G$ . Typically,  $G$  can vary from a few to more than a million over the range of devices available to the radar engineer.

The current output of the ideal photodetector can be imagined as a train of Poisson point process impulses of rate  $\eta P(t)/h\nu_o$  and average weight  $Ge$ , the mean gain times the charge of an electron. The photodetector load resistor  $R_L$  adds a zero mean white noise of spectral level  $2k_B T_L/R_L$  where  $T_L$  is the load temperature and  $k_B$  is Boltzman's constant. A third component is added representing the device's dark current due to unavoidable spontaneous photoconductor generation. The sum of these three processes is passed through a linear time invariant (LTI) detector response filter  $h(t)$  which models the photodetector's overall bandwidth. The photodetector output,  $i(t)$ , is presented at the output of the detector response filter. Thus, the direct detector output  $i(t)$  is fundamentally a shot-noise process, because the driving

photon interarrival times are Poisson distributed, but additional noise accrues because of illumination gain, thermal current and dark current randomness.

The first and second moments of  $i(t)$  are of interest since the photodetector output is the measurement test point for the set of RTI projections. An added complication comes in when we realize that the incident optical power is subject to random speckle fades. However, these moments are shown to be [34, lecture 7, p. 9]

$$\langle i(t) \rangle = \frac{eG\eta}{h\nu_o} \int d\tau h(t - \tau) [\langle P(\tau) \rangle + P_d] \quad (4.7)$$

$$\begin{aligned} K_{ii}(t, s) = & \frac{e^2 G^{2+x} \eta}{h\nu_o} \int d\tau h(t - \tau) h(s - \tau) [\langle P(\tau) \rangle + P_d] \\ & + \left\{ \frac{eG\eta}{h\nu_o} \right\}^2 \int d\tau \int d\mu h(t - \tau) h(s - \mu) K_{PP}(\tau, \mu) \\ & + \frac{2k_B T_L}{R_L} \int d\tau h(t - \tau) h(s - \tau) \end{aligned} \quad (4.8)$$

where  $P_d$  is the equivalent dark current optical power and  $K_{PP}(t, s)$  is the incident optical power covariance.

#### 4.1.4 Post-Detection Image Processing

Having reached the end of the signal path, we now complete the RTI imaging model with a discussion of the post-detection image processing. As the target completes one revolution, our goal is to gather  $N$  reflectance projections. We approach this semi-discrete problem by transmitting a periodic train of short-duration pulses to the target. The resulting set of received returns correspond to projections taken at equiangular increments of the target rotation. For example, to acquire 20 projections of a target spinning at 1 revolution per second, we would transmit a pulse every 50 ms to produce projections separated by 18 degrees in the Radon transform space.

Each sample consists of a short duration record of the received signal  $i(t)$  after correcting for the round trip propagation delay to the target center and back. The  $n^{\text{th}}$  range projection  $p_{\theta_n}(r)$  of the target at time  $t_n$  during the arrival of the illumination pulse is then defined to be:

$$p_{\theta_n}(r) = i(t) \Big|_{t = 2r/c + t_n + L/c + 2R_T/c} \quad (4.9)$$

The retarded time terms are calculated to align each projection with the target center at the range  $r = 0$ . The  $N$  projections will be subjected to standard tomographic reconstruction techniques to form a reflectance image of the spherical target. In the next section we turn our attention to calculating the first and second moments of the projections  $p_{\theta_n}(r)$ .

## 4.2 Projection Statistics

In this section we outline the calculations describing the first and second moment statistics of the projections provided by the above RTI imaging model. We begin by expressing the mean optical return intensity intercepted by the photodetector as a function of both the projected target reflectivity and the pulse propagation over the target surface. After taking into account the photodetection process, this result is rewritten as the range dependent photodetection mean current. This projection first moment result exhibits features which begin to hint at some of the image reconstruction distortion issues. Finally, a similar analysis is performed to determine the second moments of both the filtered and unfiltered projections used in image reconstruction. At this point in the discussion, we begin with the derivation of the projection mean  $\langle p_{\theta_n}(r) \rangle$ .

In section 4.1.1 we determined that the probe beam  $U_P(\vec{\rho}_2, t)$  striking the target  $\mathcal{T}$ -plane was a Gaussian beam with a field modulation written in retarded time

coordinates. In the case of super-range resolution, the short-duration pulse travelling over the target will freeze the surface motion and leave unresolved any Doppler shift in the return. Therefore, the return echo  $\mathbf{U}_E(\vec{\rho}_2, t)$  at the  $\mathcal{T}$ -plane will be formulated by taking the product of probe beam  $\mathbf{U}_P(\vec{\rho}_2, t)$  and the projected target reflectance  $\mathbf{T}(\vec{\rho}_2, t)$  frozen in place at time  $t_n$  while retarding the time variable in an appropriate fashion to account for the round trip delay from the  $\mathcal{T}$ -plane to the underlying target surface. This multiplicative model can be constructed by specifying the probe beam and echo in terms of their time-domain Fourier transforms. Therefore, we model the return echo at the target as:

$$\mathbf{U}_E(\vec{\rho}_2, f) = \mathbf{T}(\vec{\rho}_2, t_n) \mathbf{U}_P(\vec{\rho}_2, f) \exp \left\{ -4\pi j f \left[ R_T - \sqrt{R_T^2 - |\vec{\rho}_2|^2} \right] / c \right\} \quad (4.10)$$

where  $\mathbf{U}_P(\vec{\rho}_2, f)$  and  $\mathbf{U}_E(\vec{\rho}_2, f)$  are the time-domain Fourier transforms of the probe beam and return echo respectively, and  $\mathbf{T}(\vec{\rho}_2, t_n)$  is the target reflectivity evolution frozen for an instant by the short-duration illumination pulse at time  $t_n$ . The exponential delay term restores retarded time as the pulse travels from the  $\mathcal{T}$ -plane to the spherical target surface and back. Note that Doppler shift has been neglected.

In order to calculate the optical power falling on the photodetector, we must take the inverse Fourier transform of  $\mathbf{U}_E(\vec{\rho}_2, f)$  with respect to frequency and then use the Fraunhofer diffraction formula to propagate the target echo to the laser radar. As in section 4.1.1, we will assume with insignificant error that the return field modulation rides a planar wavefront upon arrival at the receiver aperture. This approximation is valid because the spatial depth of the return field modulation is significantly larger than the departure of the curving return wavefront from a flat plane. Therefore, the time retardation from the  $\mathcal{T}$ -plane to the receiver is  $L/c$ , independent of the position within the aperture.

Using the Fraunhofer diffraction formula, the complete retarded time target echo

caused by the illumination pulse reaching the target at time  $t_n$  is propagated back to the laser radar. Taking the expectation of the return field intensity with respect to the surface roughness and integrating over the receiver aperture results in the mean optical power  $\langle P(t) \rangle$  falling on the photodetector, giving the following result:

$$\langle P(t) \rangle = \frac{P_T}{a_L^2} \cdot \pi a_R^2 \cdot \frac{k^2 \rho_T^2}{4\pi^2 L^2} \int d\vec{\rho}_2^+ \rho(\vec{\rho}_2^+, t_n) \exp \left\{ - |\vec{\rho}_2^+|^2 / b^2 \right\} s \left( t - t_n - L/c - 2 \left[ R_T - \sqrt{R_T^2 - |\vec{\rho}_2^+|^2} \right] / c \right) \quad (4.11)$$

where

$$b^2 \equiv \frac{1}{\frac{\rho_T^2 k^2}{R_T^2} + \frac{2}{a_T^2}}. \quad (4.12)$$

The derivation assumes that the surface correlation length  $\rho_T$  is much smaller than the target spatial extent  $a_T$ . The details behind propagating the target surface correlation structure to the optical field present at the receiver aperture during the course of this mean power calculation are covered in Appendix B.

This result has elements in common with standard radar equation for the mean return power from an angle-angle unresolved target [2, §1.2]:

$$\langle P \rangle = \underbrace{\frac{P_T G_T}{4\pi L^2}}_{1^{\text{st}}} \times \underbrace{A_R}_{2^{\text{nd}}} \times \underbrace{\frac{\sigma_{cs}}{4\pi L^2}}_{3^{\text{rd}}}. \quad (4.13)$$

The first factor is the on-axis target irradiance where  $G_T$  is the transmitter antenna gain referenced to an isotropic source. This factor corresponds directly to the RTI on-axis irradiance term  $P_T/\pi a_L^2$  in (4.11). The second factor in the radar equation is the effective reception area of the receiver aperture. This factor, which accounts for the portion of the return power collected by the receiver aperture area  $A_R$ , corresponds to the nominal receiver aperture area  $\pi a_R^2$  in the RTI system. The third factor,  $\sigma_{cs}/4\pi L^2$ , is the effective target cross-section solid angle subtended from the

laser radar aperture. This then matches the remaining integral factor in (4.11) scaled by the wavenumber squared  $k^2$  times the surface correlation area  $\rho_T^2$  and divided by  $4\pi^2 L^2$ . Therefore, in the RTI case, the angle-angle unresolved target cross-section is a function of propagation time or range.

The right-hand-side integral is a two-dimensional integral taken with respect to the  $\mathcal{T}$ -plane spatial variable  $\vec{\rho}_2$ . The integrand factor  $\rho(\vec{\rho}_2, t_n)$  is the two-dimensional  $\mathcal{T}$ -plane projection of the exposed three-dimensional surface reflectivity distribution  $\rho(x, y, z)$  after the target has rotated through an angle of  $\theta_n = \Omega t_n$  radians. The second integrand factor is a circular two-dimensional Gaussian weighting function which serves to spatially window the two-dimensional reflectivity projection  $\rho(\vec{\rho}_2, t_n)$ . The window dimensions depend upon the wavenumber and target parameters. At a fixed time  $t$ , the product of these two factors are weighted by  $\mathcal{T}$ -plane projection of the target surface illumination pattern determined by the time dependent position of the pulse  $s(t)$ .

Let us now begin to interpret the time-of-flight,  $t$ , as equivalent to the target centered range,  $r$ , via the relation  $r = \frac{1}{2}c(t - t_n) - L - R_T$ . Therefore, for a very short duration pulse, the above integral collapses the weighted “side-projected” reflectivity lying along a loop on the target onto the range axis at the point  $r = \frac{1}{2}c(t - t_n) - L - R_T$ . Or, in other words, the return power corresponds to constant range cross-sections of the exposed target surface. This result can be regarded as a Radon transform type operation *taken over a circle* on the target surface at the constant range plane  $r = \frac{1}{2}c(t - t_n) - L - R_T$ . The fact that side-projected reflectivity is windowed by the circular Gaussian factor before Radon transformation means that projections incur some distortion.

In coming to grips with the role of the Gaussian window function in (4.11), let us

digress from our discussion and imagine shining a flashlight on a semi-rough surfaced metal ball. Looking beyond the rear of the flashlight straight towards the ball, we would see the target illuminated by the flashlight beam. The reflection from the center of the ball would be the brightest because the normal orientation of the surface would tend to scatter light directly back to the observer. However, as we move our gaze to the limb, we would see the scattered light diminish. This occurs because the back reflection from semi-diffuse surfaces drops as the angle of incidence increases between the radiation line-of-sight and the surface normal. In the two extreme surface classes of a Lambertian or highly rough surface and a specular or polished surface, the back reflection fall-off is either slow or rapid, respectively, as the angle of incidence increases from zero to  $90^\circ$ . In other words, shiny balls reflect light back from a small region near the center, while very rough balls apparently reflect light from all over the illuminated face. Most surfaces behave somewhere in between.

These same effects are modelled by the Gaussian weighting factor above. The  $\mathcal{T}$ -plane centered Gaussian window causes the target back reflection to fall-off as the reflection point moves away from the perceived target center to the limb. The rate of this fall-off is controlled by the parameter  $b$  which is inversely proportional to the sum of two terms. The first term,  $k^2 \rho_T^2 / R_T^2$ , models the phenomenon of surface roughness-aspect angle dependent back reflection. Different surface classes ranging between specular and Lambertian can be chosen by setting the surface roughness correlation length  $\rho_T$  either as large or small, respectively, in terms of the operating wavelength  $\lambda$ .

The second term,  $2/a_T^2$ , accounts for the finite intensity support that we have assigned to the target. As the reader will recall from the target modelling discussion, this parameter was set in place in order to guarantee a closed-form solution after



Fraunhofer propagation to the receiver. However, this inclusion generates an artifact in each projection by unnecessarily dimming the target limb. This effect can now be removed without any loss in accuracy by letting  $a_T$  grow large and restricting  $\vec{\rho}_2$  lie only within the support of the  $\mathcal{T}$ -plane projection of the target reflectivity.

The received intensity will be directly detected by the RTI laser radar. Using the previous statistical photodetection model, the mean RTI projection can be written as:

$$\begin{aligned}
 \langle p_{\theta_n}(r) \rangle &= \langle i(t) \rangle \Big|_{t=2r/c+t_n+L/c+2R_T/c} \\
 &= \frac{eG\eta}{h\nu_o} h(t) \star \langle P(t) \rangle \Big|_{t=2r/c+t_n+L/c+2R_T/c} \\
 &= \frac{eG\eta}{h\nu_o} \frac{P_T}{4\pi a_L^2} a_R^2 \frac{k^2 \rho_T^2}{L^2} \\
 &\quad \int d\vec{\rho}_2 \rho(\vec{\rho}_2, t_n) [h \star s] \left( 2r/c + 2\sqrt{R_T^2 - |\vec{\rho}_2|^2}/c \right) e^{-|\vec{\rho}_2|^2/b^2} \quad (4.14)
 \end{aligned}$$

where the symbol  $\star$  stands for the convolution operator and the origin of the range coordinate system  $r$  has been shifted to the target center. Note that this formulation demonstrates that RTI projections will be smeared by the finite photodetector response time reinterpreted as the corresponding spatial range depth of the illumination pulse  $s(t)$ .

Let us now turn our attention to the projection covariance. As shown in §2.1 of Appendix B, individual projection measurements will be statistically independent if

$$N \ll \frac{\sqrt{2\pi} R_T}{\rho_T} \quad (4.15)$$

which is always the case for meter-sized rough-surfaced targets at infrared or visible wavelengths. Therefore, the correlation from one projection to the next will be negligible and the second moment of any consequence will be the projection self-covariance. Making the same arguments and assumptions as above in the analysis

of the first moment and applying Gaussian moment factoring, §2.1 of Appendix B demonstrates the projection covariance to be:

$$\begin{aligned}
K_{pp}(r_1, r_2) \approx & \frac{1}{4\sqrt{\pi}} \frac{e^2 G^{2+x} \eta}{h\nu_o} \frac{k^2 a_R^2}{L^2} \frac{P_T \rho_T^2}{a_L^2} \rho B \left(\frac{1}{2}cT\right) \times \\
& \left(-\frac{r_1 + r_2}{2}\right) \exp\left\{-\frac{(r_1 - r_2)^2}{4\pi^2 B^2}\right\} \times \\
& \left[\Phi\left\{\left(\frac{r_1 + r_2}{2} + R_T\right)/\frac{1}{2}cT\right\} - \Phi\left\{\left(\frac{r_1 + r_2}{2}\right)/\frac{1}{2}cT\right\}\right] \\
+ & \left(\frac{eG\eta}{h\nu_o}\right)^2 \left(\frac{ka_r}{L}\right)^4 \left(\frac{P_T \rho_T^2}{a_L^2}\right)^2 \rho^2 \left(\frac{1}{2}cT\right)^2 T B_1 \times \\
& \left(-\frac{1}{2}(r_1 + r_2)\right)^2 \exp\left\{-\frac{(r_1 - r_2)^2}{4\pi^2 B_1^2}\right\} \times \\
& \left[\Phi\left\{\left(\frac{1}{2}(r_1 + r_2) + R_T\right)/\frac{1}{2}cT\right\} - \Phi\left\{\left(\frac{1}{2}(r_1 + r_2)\right)/\frac{1}{2}cT\right\}\right]^2 \\
+ & \sqrt{\pi} B \frac{2k_B T_L}{R_L} \exp\left\{-\frac{(r_1 - r_2)^2}{4\pi^2 B^2}\right\} \quad (4.16)
\end{aligned}$$

where positive values of  $r_1$  and  $r_2$  fall on the far side of the target; the error function,  $\Phi(x)$ , is defined to be

$$\Phi(x) \equiv \frac{1}{\sqrt{\pi}} \int_0^x dt \exp\{-t^2\}$$

and the quantity

$$B_1 \equiv \sqrt{\frac{1}{4\pi^2 T^2 + \frac{1}{B^2}}} \quad (4.17)$$

is the total system bandwidth. This result was obtained by assuming a Gaussian shaped pulse  $s(t) = e^{-\frac{1}{2}t^2/T^2}$  with a nominal pulse width of  $T$  seconds and a Gaussian shaped photodetector frequency response  $h(f) \xleftrightarrow{\mathcal{F}} e^{-\frac{1}{2}f^2/B^2}$  with a bandwidth of  $B$  Hertz. Furthermore, a low-contrast model for the target reflectivity was adopted, i.e.,  $\rho(x, y, z) = \rho + \delta\rho(x, y, z)$  where  $|\delta\rho(x, y, z)| \ll \rho$ . This reflectance model was adopted in order to give closed-form expressions for the spatial integrals over the target surface during Fraunhofer propagation.

Note that the covariance is the sum of three terms. The first term accounts for the effects of photodetector shot-noise driven by the return power, neglecting dark current and background light. Speckle induced variations within the target return contribute the second term. The final term is the thermal noise developed across the photodetector load resistor. The thermal and shot-noise decorrelation distances are on the order of  $c/B$  while the speckle decorrelation distance is proportional to  $c/B_1$ .

Likewise, the variance was calculated in Appendix B §2.2 for projections processed by the inverse Radon transform spatial reconstruction filter  $|f|$ . Assuming the reasonable case of useful spatial resolution (i.e., the so-called super-resolution condition  $c/B_1 \ll R_T$ ), the filtered projection variance is found to be:

$$\begin{aligned}
\text{var}_{p/p'}(r) \approx & \frac{\pi e^2 G^{2+x} \eta}{2 h \nu_o} \left( \frac{k a_r}{L} \right)^2 \frac{P_T \rho_T^2}{a_L^2} \rho \left( \frac{1}{2} c T \right) B^3 / c^2 \times \\
& (-r) \left[ \Phi \left\{ (r + R_T) / \frac{1}{2} c T \right\} - \Phi \left\{ r / \frac{1}{2} c T \right\} \right] \\
& + 2 \left( \frac{e G \eta}{h \nu_o} \right)^2 \left( \frac{k a_r}{L} \right)^4 \left( \frac{P_T \rho_T^2}{a_L^2} \right)^2 \rho^2 \left( \frac{1}{2} c T \right)^2 T B_1^3 / c^2 \times \\
& (-r)^2 \left[ \Phi \left\{ (r + R_T) / \frac{1}{2} c T \right\} - \Phi \left\{ r / \frac{1}{2} c T \right\} \right]^2 \\
& + 2 \sqrt{\pi} \frac{2 k_B T_L}{R_L} \frac{B^3}{c^2}. \tag{4.18}
\end{aligned}$$

This result also assumes the low contrast reflectivity model of the previous result and identical definitions for  $s(t)$  and  $h(t)$ . Again, the contributions from photodetector shot-noise, speckle and load resistor thermal noise are summed in that order.

This final variance will be used in the next section along with the projection mean to formulate a SNR-like figure of merit for filtered backprojection reconstructed images.

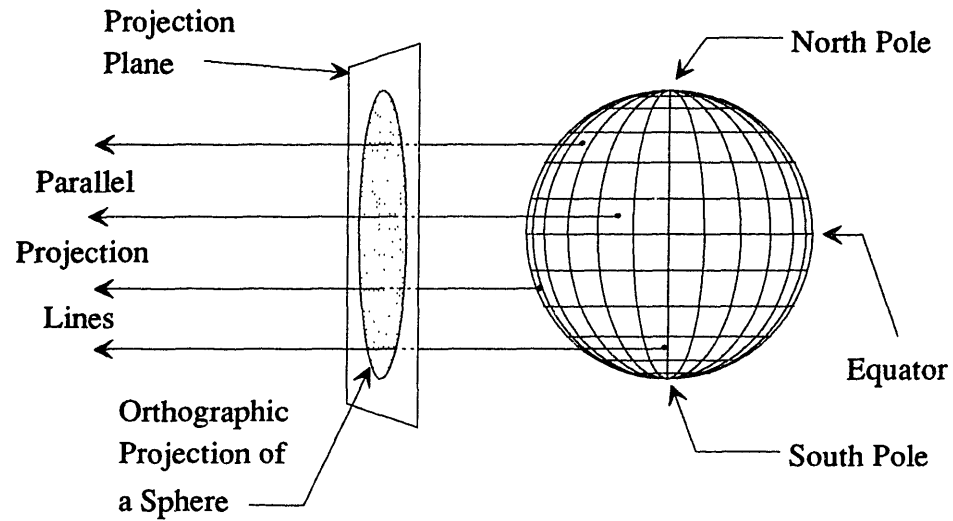
### 4.3 Reconstructed Image Performance

In this final section we will characterize the performance of the RTI imaging system in terms of the various forms of aberrations which cause the reconstructed image to depart from the ideal image. Typically, the analyst will separate aberrations caused by limitations in the system design from those caused by noise sources corrupting the measurements. In this analysis, one of our goals is to understand and quantify the impact of speckle and receiver front-end noise upon system performance by defining and calculating an image signal-to-noise ratio (SNR). Essentially, this quantity will compare the squared mean-image to the image variance with respect to both the shot-, speckle and load resistor noise sources. While this gives an indication of the noise-induced image fluctuations about the expected image vis-á-vis a fixed target reflectivity and radar design parameters, the SNR provides little insight into the deterministic distortions caused by limitations in the system design or imaging technique. The second goal of this section is to conduct an investigation into this other class of distortions which will lead to the construction of the imaging system point spread function (PSF) and ultimately the image resolution. This exercise, which we now begin, will provide us with a comparative interpretation of the RTI imaging scenario in relation to the standard two-dimensional tomographic problem.

Cartographers have never produced a undistorted global map of the earth's surface features. Since the RTI imaging system is attempting to produce a flat two-dimensional image of a three-dimensional surface feature distribution across a sphere, we suspect that the tomographic reconstruction will build in unavoidable distortions in addition to the photodetector response smearing indicated earlier. In modeling the sphere reflectance,  $\mathbf{T}(\vec{\rho})$ , the exposed three-dimensional surface reflectance  $\rho(x, y, z)$

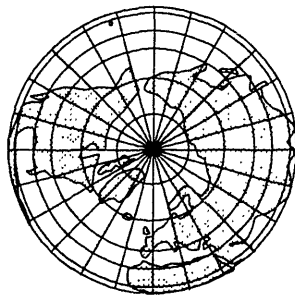
is projected by parallel rays upon the perpendicular  $\mathcal{T}$  plane, with the laser radar observer located at infinity. Cartographers refer to this type of projection as the orthographic projection (see Figure 4.4(a)) [35]. It is precisely these transverse orthographic projections of the reflectance  $\rho(x, y, z)$  on to the  $\mathcal{T}$ -plane upon which the RTI Radon transform operates to produce the set of  $N$  tomographic projections  $p_\theta(r)$ .

Any two-dimensional backprojection reconstruction applied to this set of  $N$  RTI projections will form a flat image. Consider the nature of this image. In the standard tomographic projection of a two-dimensional field, all the points lying on a common range displacement (scan line) contribute to a single projection ordinate value through a line integral construction. This same principle holds true for range projections of rotating three-dimensional targets. The locus of surface scatterers lying in the  $x$ - $z$  plane at a cross-range displacement of  $r$  from the target rotation axis will contribute to the single RTI projection ordinate  $p(r)$  through a line integral expression, albeit a somewhat more complicated formulation which takes into account surface aspect. If we suppress the  $z$  dependence in the three-dimensional problem by choosing a vantage point above the target north pole, the plane  $x = r$  becomes the scan line  $x' \cos \theta + y' \sin \theta = r$  in the  $z$ -axis rotated coordinates. This means that a surface feature located at the *cylindrical* coordinates  $(r, \theta, z)$  within the target frame will be mapped to the *polar* coordinates  $(r, \theta)$  within the image frame by the backprojection-reconstruction process. Therefore, ignoring the issues connected with formulating a line integral surface-aspect dependent metric, the reconstructed two-dimensional image is a projection of the target reflectance  $\rho(x, y, z)$  onto the  $x$ - $y$  plane. In other words, the reconstruction is attempting to reproduce the *two-dimensional* distribution  $\rho_{\text{polar}}(x, y) = \rho\left(x, y, +\sqrt{R_T^2 - x^2 - y^2}\right) + \rho\left(x, y, -\sqrt{R_T^2 - x^2 - y^2}\right)$ . This quantity is the sum of the northern and southern normal (polar) orthogonal projections across



(a)

Normal Projection



(b)

Transverse Projection



(c)

Figure 4.4: (a) Construction of the Orthographic Projection of a Sphere (b) Normal Orthographic Projection of the Globe (c) Transverse Orthographic Projection of the Globe

the  $x$ - $y$  plane (see Figure 4.4(b)).

The above argument forces us to conclude that the polar coordinates of a surface feature are preserved through the process of RTI projection formation and backprojection image reconstruction. However, this does not guarantee that the reconstructed reflectance *values* of a surface feature will compare equally with the bi-hemispherical polar target projection. To see how this discrepancy occurs, consider the transverse orthographic projection of Figure 4.4(c). In any Radon transform of this transverse projection, the contribution from regions near the equator (e.g. Central America) will dominate contributions from higher latitudes (e.g. Canada) when compared on the basis of features with equivalent surface areas on the sphere. The difference between contributions is explained by a change in surface aspect which causes a foreshortening effect in the plane of projection. Note that a similar comparison leads to exactly the opposite conclusion when considering the polar orthogonal projection (Figure 4.4(c)). These considerations lead us to the preliminary conclusion that the broadside nature of the RTI projections will emphasize equatorial over limb-sited features in the reconstructed image.

The above observations indicate that the set of range resolved projections  $p_{\theta_n}(r)$  should be rewritten as a Radon transform of the polar projected reflectivity,  $\rho_{\text{polar}}$ , before attempting to formulate the imaging system PSF. Beginning with the line integral description of the  $\mathcal{T}$ -plane projected reflectivity, this step gives

$$\begin{aligned} \langle p_{\theta_n}(r) \rangle &= \frac{eG\eta}{h\nu_o} \frac{P_T}{a_L^2} \pi a_R^2 \frac{k^2 \rho_T^2}{4\pi L^2} \int dr' [h \star s](2r/c - 2r'/c) \\ &\int_{-\infty}^{+\infty} dx e^{-[R_T^2 - r'^2]/b^2} \underbrace{\frac{r'}{\sqrt{R_T^2 - x^2 - r'^2}}}_{\text{Aspect Metric}} \rho_{\text{polar}}(x'_{\theta_n}(x, r'), y'_{\theta_n}(x, r')) \quad (4.19) \end{aligned}$$

where the polar projection  $\rho_{\text{polar}}$  is written in the  $(x', y')$  coordinate system rotated  $\theta_n$

radians about the  $z$ -axis, the surface aspect metric is introduced through the change of variables from  $\vec{\rho}_2$  to  $x$  and  $z$  on the target surface and the exponential factor accounts for the surface roughness–aspect angle effect upon the optical return. We consider the aspect metric as a two-dimensional function which windows the polar reflectivity before the line integral transform is performed. Thus, this result is a *generalized* Radon transform which weights contributions near the target broadside (equator) over those from the target limb (polar) regions [27, §II.7]. Furthermore, the contribution from individual features decreases as the target rotation moves them away from the  $y$ -axis (radar line-of-sight). This behavior accounts for the change in surface aspect as target rotation draws features across the illuminated exposure.

This formulation gives us the final link in writing the mean reconstructed RTI image in terms of the convolution of a two-dimensional PSF with the polar reflectivity projection  $\rho_{\text{polar}}(x, y)$ . The PSF for a specific point  $(x_o, y_o)$  in the  $(x, y)$  plane is found by placing a two-dimensional delta function at  $(x_o, y_o)$  and calculating the Radon transform of (4.19) and then computing the convolution of (4.14) to give the set of  $N$  RTI projections. This set of projections is then subjected to filtered backprojection reconstruction producing the PSF  $H(x, y, x_o, y_o)$ . Assuming a Lambertian target for simplicity's sake, this set of operations gives:

$$\begin{aligned}
 H(x, y, x_o, y_o) &= \frac{eG\eta}{h\nu_o} \frac{P_T \rho_T^2}{4\pi a_L^2} \frac{k^2}{L^2} a_R^2 \frac{r_o}{\sqrt{R_T^2 - r_o^2}} \times \\
 &\frac{2\pi}{N} \sum_{\substack{n=0, \theta_n \in \\ [-\theta_o, \pi - \theta_o]}}^{N-1} \underbrace{\sin(\theta_n + \theta_o)}_{\text{Aspect Angle}} \underbrace{\mathcal{H}\left[e^{-[r - r_o \cos(\theta_n + \theta_o)]^2 / c^2 / B_1^2}\right]}_{\substack{\text{Reconstruction} \\ \text{Projection} \\ \text{Prefiltering}}}(x \sin \theta_n + y \cos \theta_n) \quad (4.20)
 \end{aligned}$$

where the dependence upon  $(x_o, y_o)$  is expressed through the polar coordinates  $r_o^2 =$



$$x_o^2 + y_o^2 \text{ and } \tan^{-1} \theta_o = y_o/x_o.$$

Let us take a moment to interpret this formulation. The operator  $\mathcal{H}$  is the inverse Radon transform projection prefiltering operator  $\mathcal{F}^{-1}[|f| \times \mathcal{F}(p_\theta(r))]$ . It is applied to the detector response time smeared Gaussian projections of the delta function. The sine function models the projection angle dependent effect of surface aspect change throughout target rotation. Note that as a feature apparently travels from one target limb to the other, the corresponding contribution from this sine term goes from zero to unity on-axis and back down to zero at the far limb. These factors are combined under the backprojection summation sign to produce an unscaled PSF. This result is then scaled by various familiar laser radar engineering parameters and an additional factor which depends upon the original position  $(x_o, y_o)$  of the delta function. This last factor accounts for the latitudinal dependence of the surface aspect surrounding the delta function. Therefore, unlike the formulation developed in chapter 3, the RTI image PSF is *not* position independent, and the mean image must now be recovered through a superposition integral rather than a convolution operation.

The presence of the sine function under the backprojection summation makes a closed form solution of (4.20) difficult to calculate. However, the normalized PSF has been numerically calculated and the result is shown in Figure 4.5. The result is a dumbbell-shaped PSF which has zero amplitude when located at the origin but blows-up at the equator. The PSF minor axis lies along the radial axis protruding from the origin. The major and minor axes lengths of the half-maximum half-width dumbbell contour are approximately 2.1 and 1.4 times  $c/B_1$ . Therefore, the reconstructed RTI image will have finer resolution with respect to the radial axis than along the transverse radial axis. Thus, we define  $c/B_1$  to be the nominal RTI resolution.

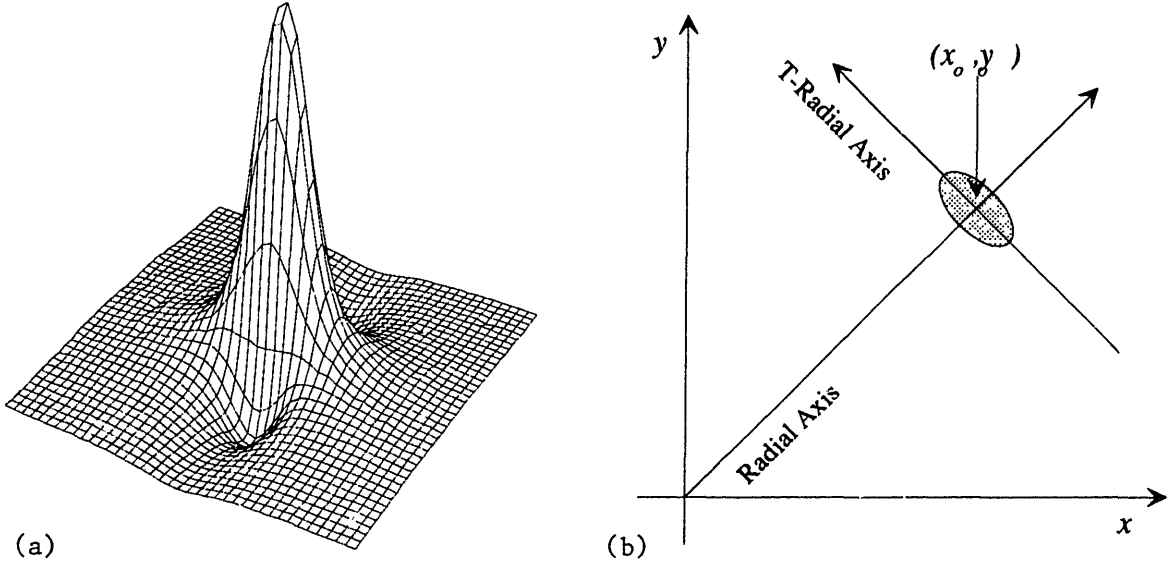


Figure 4.5: (a) PSF Reconstruction for  $N = 144$  Projections. (b) PSF Orientation.

Having demonstrated the resolution of the RTI imaging system, we now begin an investigation of the reconstructed image noise performance via an appropriate formulation of a signal-to-noise ratio. As in chapter 3, we adopt the following SNR definition as a measure of reconstruction quality:

$$\text{SNR}(x_o, y_o) = \frac{(\text{Reconstructed Image Mean at } (x_o, y_o))^2}{\text{var}\{\text{Reconstructed Image at } (x_o, y_o)\}}.$$

On a pointwise basis, this measure contrasts the relative strength of the mean image to the average strength of noise induced fluctuations.

Retaining our assumptions of a low-contrast reflectivity description and sufficient system bandwidth to resolve details smaller than the target, the numerator of the above SNR becomes

$$\text{SNR}(x_o, y_o) = \frac{\delta f^2(x_o, y_o) \left| \int dx \int dy H(x, y, x_o, y_o) \right|^2}{\text{var}\{\text{Reconstructed Image at } (x_o, y_o)\}} \quad (4.21)$$

where we have approximated the mean response by taking the product of the slowly varying low-contrast reflectivity component with the area under PSF. This action is

valid when the PSF spatial bandwidth is much larger than the bandlimited feature component, which is certainly true under our super-resolution assumption.

Since projections are statistically independent, the variance in the denominator can be found by backprojecting the filtered projection variance (4.18) over the entire circle of projection angles. The number of projections required for the image reconstruction in this reflective tomography problem must be greater than  $2\pi q$  where  $q$  is the number of radial resolution cells on the target. Therefore, for a handful of resolution cells across the target, the number of required projections is on the order of 20–25. Under this condition, the semi-discrete variance backprojection summations for the shot-noise and speckle contributions can be closely approximated by the corresponding continuous formulations, resulting in a closed form expression for the SNR.

Taking these approximations results in the following low-contrast super-resolution deep far-field SNR:

$$\text{SNR}(x_o, y_o) = \frac{N \left( \frac{c}{B_1 R_T} \right)^2 \text{CNR} \delta f^2(x_o, y_o) / 16\pi^5}{\underbrace{\sqrt{\frac{\pi}{2}} G^x \frac{B^2}{B_1^2} \left[ \frac{16}{\sqrt{\pi}} \frac{P_{Th} + P_D}{P_{R,peak}} \frac{R_T}{\sqrt{x_o^2 + y_o^2}} + 1 \right]}_{1^{\text{st}}}} + \underbrace{\frac{TB_1 \rho^2 \text{CNR}}{2^{\text{nd}}}}_{2^{\text{nd}}} \quad (4.22)$$

where we have defined the carrier-to-noise ratio (CNR) to be the ratio of the mean projection current squared to the signal shot-noise component, i.e.,

$$\begin{aligned} \text{CNR} &\equiv \frac{\left[ \sqrt{\frac{\pi}{2}} \frac{eG\eta}{h\nu_o} \frac{P_T}{a_L^2} a_R^2 \frac{k^2 \rho_T^2}{L^2} \left( \frac{1}{2}cT \right) \sqrt{x_o^2 + y_o^2} \right]^2}{\sqrt{\frac{\pi}{2}} \frac{e^2 G^2 \eta}{h\nu_o} \frac{P_T}{a_L^2} a_R^2 \frac{k^2 \rho_T^2}{L^2} B \left( \frac{1}{2}cT \right) \rho \sqrt{x_o^2 + y_o^2}} \\ &= \sqrt{\frac{\pi}{2}} \frac{\eta P_T}{h\nu_o B} \frac{a_R^2}{a_L^2} \frac{k^2 \rho_T^2}{L^2} \left( \frac{1}{2}cT \right) \sqrt{x_o^2 + y_o^2} / \rho \quad (4.23) \end{aligned}$$

and we have normalized by the low-contrast reflectivity component present in the numerator mean response. The above SNR result introduces the thermal-noise equivalent power,  $P_{Th}$ , which is the optical power needed to produce a shot-noise component equivalent to the thermal noise contribution, viz.,

$$\frac{2k_B T_L}{RL} = \frac{e^2 G^{2+x} \eta}{h\nu_o} P_{Th}$$

and the peak received power,  $P_{R,peak}$

$$P_{R,peak} = \frac{P_T}{a_L^2} a_R^2 \frac{k^2 \rho_T^2}{L^2} \left(\frac{1}{2} cT\right) \rho R_T$$

corresponding to a range of  $r = -R_T$ . This resulting CNR-dependent SNR formulation conveniently expresses performance in terms of physical measures.

From equation (4.22) we see that the filtered backprojection reconstructed RTI image SNR is directly proportional to the number of projections,  $N$ , and the square of the number or radial resolution cells,  $q = c/B_1 R_T$ . The SNR is inversely proportional to the sum of two terms. The first term combines the contributions from the received power shot-noise, the photodetector dark current shot-noise and the load resistor thermal noise. This term increases as the point  $(x_o, y_o)$  is relocated away from the target boundary toward the image center, eventually dominating the entire denominator. This condition, which will always occur in a region about the image center, corresponds to a combined dark current-thermal noise limit. The second denominator term is the excess speckle noise contribution. It is directly proportional to the CNR and the nominal target reflectivity squared. As the CNR grows with increasing transmission power, the SNR will grow beyond the dark current-thermal noise limit in regions away from the image center and eventually saturate at a new level determined by speckle.

Thus, in the high CNR regime, the speckle-limited SNR takes the following value:

$$\frac{\delta f^2(x_o, y_o)}{\rho^2} N \frac{(c/B_1 R_T)^2}{16\pi^2 T B_1} \approx \frac{\delta f^2(x_o, y_o)}{\rho^2} N \frac{(c/B_1 R_T)^2}{4\sqrt{2}\pi^4} \quad (4.24)$$

where we have introduced the approximation by equating the transmission pulse and photodetector response filter bandwidths. Therefore, presuming the absence of angle-angle resolution, the typical RTI tomographic imaging scenario achieving a handful of radial resolution cells requires a large number of projections, on the order of several thousand or more, to drive the SNR up to  $\delta f^2(x_o, y_o)/\rho^2$ , the conventional low-contrast speckle-limited laser radar resolved-pixel SNR.



## Chapter 5

# DTI Tomographic Imaging Performance

Motivated by the RTI tomography performance analysis, we now turn our attention to the Doppler-resolved laser radar tomography problem originally outlined in chapter 1. In this scenario we use a heterodyne laser radar to illuminate a spinning target to obtain a fixed number of Doppler broadened returns which correspond to a set of projections of the target reflectance onto the cross-range axis. Tomographic techniques will then be applied to this semi-discrete Doppler-time-intensity (DTI) record of the target revolution to reconstruct a two-dimensional reflectance image of the three-dimensional target. The goal of this inquiry is to examine the performance of this imaging technique.

Since both the RTI and DTI investigations share the same goals, as well as many common assumptions and analytical elements, this presentation of the DTI model and performance analysis is organized in a manner similar to the previous chapter. Therefore, when appropriate, we will borrow model elements and analytical treatments from the RTI investigation during the DTI presentation. Again, the emphasis of this chapter is to introduce the reader to the modelling process and the analyt-

ical concepts used to produce the reconstructed DTI image PSF and SNR quality measures. The companion Appendix C documents the details behind many of the complicated first and second moment calculations required to obtain these measures.

## 5.1 DTI Tomographic Imaging Model

In this section we will construct a model of the DTI imaging system. As in the case of the RTI analysis, model elements and issues will be discussed in the order they are visited by the energy emitted by the transmitter.

Many features of the monostatic heterodyne laser radar model are shown in Figure 5.1. We assume the diffuse spherical target is at a constant on-axis position in the radar's optical far-field at a distance of  $L$  meters from the transmitter aperture and spinning at a rate of  $\Omega$  radians per second.

### 5.1.1 Transmitter Beam Propagation

In contrast to the RTI scenario, we assume that the DTI imaging system transmitter will interrogate the target with a collimated *continuous-wave* Gaussian beam of nominal radius  $a_o$  meters. Therefore, adopting the previous beam specification sans intensity modulation, the Fraunhofer diffraction formula gives the following scalar field description for the probe beam  $U_P(\vec{\rho}_2)$  perpendicularly striking the  $T$ -plane at the target:

$$U_P(\vec{\rho}_2) = \sqrt{\frac{P_T}{\pi a_L^2}} \exp \left\{ jkL + j\frac{k|\vec{\rho}_2|^2}{2L} - j\frac{\pi}{2} \right\} \exp \left\{ -\frac{|\vec{\rho}_2|^2}{2a_L^2} \right\}. \quad (5.1)$$

Again, the parameter  $a_L = L/ka_o$  is the transmitted beam radius at the target site.



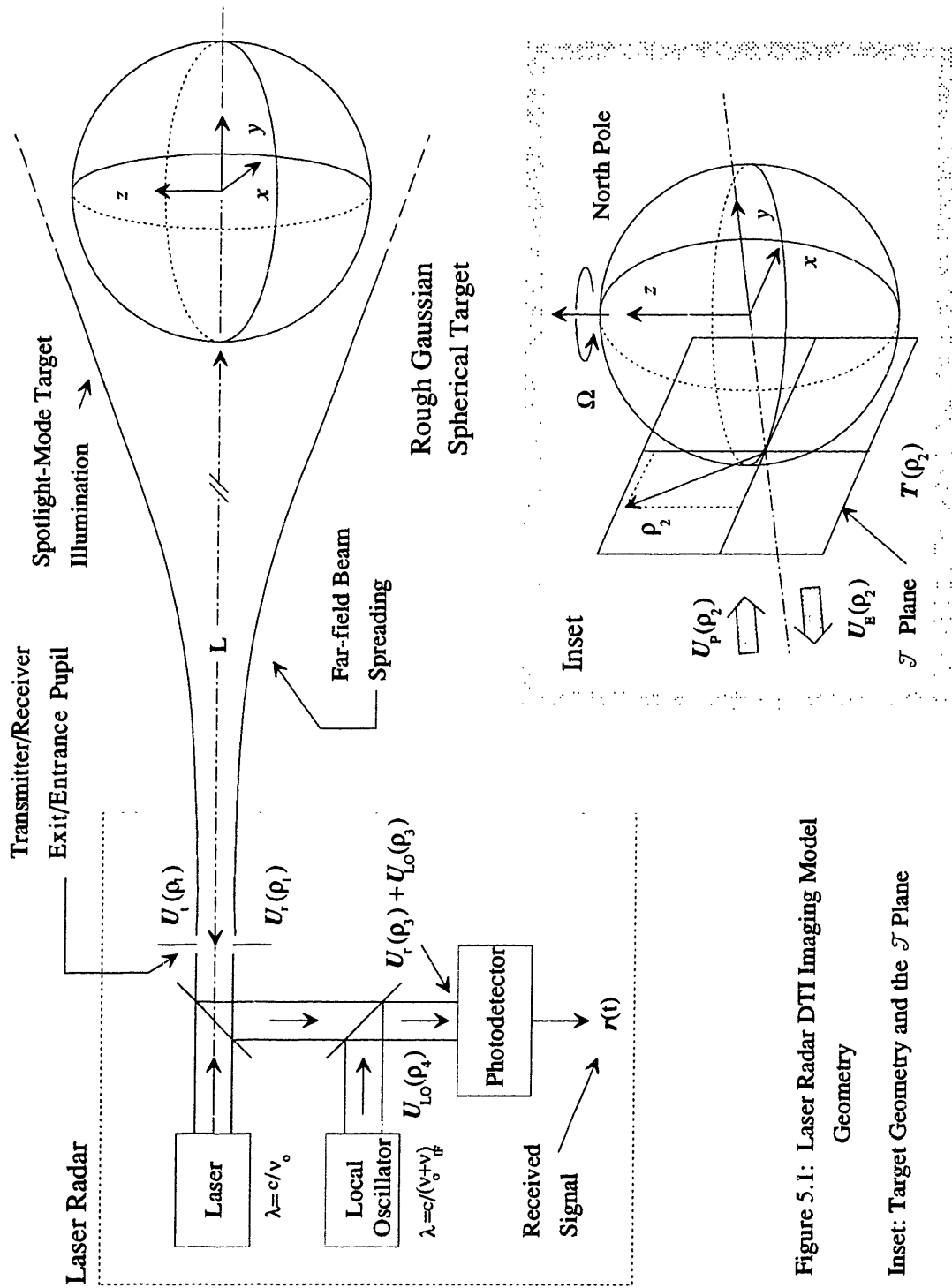


Figure 5.1:

Figure 5.1: Laser Radar DTI Imaging Model  
Geometry

Inset: Target Geometry and the  $\mathcal{S}$  Plane

### 5.1.2 Target Characterization

The time dependent target reflectivity model presented during the RTI discussion satisfies the requirements for the formulation of a DTI multiplicative reflectivity model. Therefore, we specify the complex target reflectivity,  $\mathbf{T}$ , at the point  $\vec{\rho}_2$  lying in the  $\mathcal{T}$ -plane at time  $t$  to be:

$$\mathbf{T}(\vec{\rho}_2, t) \approx \underbrace{\sqrt{\rho(\vec{\rho}_2, t)}}_{1\text{st}} \underbrace{\exp\{-|\vec{\rho}_2|^2/a_T^2\}}_{2\text{nd}} \underbrace{\exp\{jk|\vec{\rho}_2|^2/R_T\}}_{3\text{rd}} \underbrace{\exp\{2jkh(\vec{\rho}_2, t)\}}_{4\text{th}} \quad (5.2)$$

where the four factors take identical roles as in the RTI analysis. Again, we assume that the phase randomness caused by the microscopic surface height random variable  $h(\vec{\rho}_2, t)$  will cause the received fields to tend toward a circulo-complex Gaussian. Therefore, subscribing to the earlier justifications, we adopt the following phase statistics:

- $\langle \exp\{2jkh(\vec{\rho}_2, t)\} \rangle \approx \mathbf{0}$
- $\langle \exp\{2jkh(\vec{\rho}_2, t)\} \exp\{2jkh(\vec{\rho}_2', u)\} \rangle \approx \mathbf{0}$
- $\langle \exp\{2jkh(\vec{\rho}_2, t)\} \exp\{-2jkh(\vec{\rho}_2', u)\} \rangle \approx$   

$$\exp\left\{-\frac{|\vec{\rho}_2 - \vec{\rho}_2' + iR_T\Omega(t - u)|^2}{\rho_T^2}\right\}.$$

As in the RTI case, the same surface roughness issues involving variable surface aspect, shadowing and multiple reflections are ignored. Since our immediate goal is a qualitative rather than an exact quantitative understanding, we accept these approximations.

In contrast to the RTI scenario, we will assume that DTI projections are taken with sampling dwell times of such length to leave range unresolved. Therefore, in

this dual to the RTI system, the following multiplicative time-domain reflectivity formulation describes the evolution of the target echo upon the  $\mathcal{T}$ -plane:

$$\mathbf{U}_E(\vec{\rho}_2, t) = \mathbf{U}_P(\vec{\rho}_2) \mathbf{T}(\vec{\rho}_2, t). \quad (5.3)$$

This expression does not explicitly show Doppler effects; the motion of the target surface as modelled in the above phase correlations will produce the proper spatially dependent frequency shift during subsequent analysis.

### 5.1.3 Heterodyne Mixing Integral

The heart of the Doppler sensitive receiver is the optical heterodyne detector. As in a conventional superheterodyne radio receiver, the output response of the optical heterodyne detector is proportional to the beat frequency component produced by mixing the received signal with a spectrally pure local oscillator (LO) offset by an intermediate frequency (IF). However, in the case of the laser radar scenario, the return and LO signals are electromagnetic waves with carrier frequencies on the order of  $10^{14}$  Hz which corresponds to the infrared or optical portion of the spectrum. Since infrared or optical photodetectors are inherently field intensity or square-law devices, the beat signal is generated by simply focusing the LO and return fields on the light sensitive surface of these devices.

Unlike a superheterodyne radio, the optical counterpart is very sensitive to the relative spatial orientation of the incoming return field to the LO spatial mode. The optical heterodyne detector rejects return fields whose wavefronts are not coplanar with the LO wavefront. In other words, the Doppler laser radar will only respond to the target return spatial mode which matches the LO spatial mode *propagated* to the target far-field.

In practical heterodyne detectors, great care must be taken to temporally and spatially tune the LO to match the transmitted field. These systems are designed with the goal in mind of using relatively inexpensive low frequency electronic components to accomplish the post-optical detection signal processing. In fact, post-detection electronic systems often borrow from the same technology used to construct millimeter and microwave radar IF (10–60 MHz) strips.

Historically, two techniques have been used in practical continuous-wave laser radar systems to produce frequency shifted LO beams. First, the transmitted optical beam is sampled and fed through an acoustic-optic (AO) modulator driven by the IF oscillator. The LO output beam shares the same spatial mode as the transmission beam while experiencing an optical carrier frequency shift equal to the IF. The second approach uses a separate LO laser cavity whose length is adjusted using a piezo-electric (PE) device to produce the desired IF shift. The output beat signal from a second heterodyne detector which samples both the LO and the transmission beam is compared with an IF reference to generate the error signal controlling the PE crystal drive voltage.

In developing a mathematical model of the optical heterodyne detector, one finds that the beat frequency term is proportional to the square-root of the LO power,  $\sqrt{P_{LO}}$ . Therefore, laser radar systems are operated with LO powers as high as possible to maximize return signal sensitivity and minimize background light response. In this mode of operation, the photodetector LO shot-noise component dominates the contributions from both the return signal and background light shot-noise and the detector load resistor thermal noise. Under these assumptions, we now introduce a theoretical model of optical heterodyne reception which assumes perfect LO wavefront matching with the return. As with the previous optical field work, we continue to

express signal envelopes in terms of complex quantities.

In the high local oscillator power ( $P_{LO}$ ) regime, the response of the IF heterodyne detector can be modeled as [9, 10]

$$r(t) = \text{Re} [\mathbf{r}(t) \exp\{2\pi j\nu_{IF}t\}] \quad (5.4)$$

where  $\mathbf{r}(t)$  represents the complex envelope of the received signal. This envelope can be broken down into two components and written in the form  $\mathbf{r}(t) = \mathbf{y}(t) + \mathbf{n}(t)$  where

$$\mathbf{y}(t) = \int_{\text{PD}} d\vec{\rho}_3 \mathbf{U}_r(\vec{\rho}_3, t) \xi_{LO}^*(\vec{\rho}_3, t) \quad (5.5)$$

is the  $P_{LO}$  normalized heterodyne return signal. The return  $\mathbf{y}(t)$  is expressed as a heterodyne mixing integral of the product of the optical return  $\mathbf{U}_r(\vec{\rho}_3, t)$  and the local oscillator field  $\sqrt{P_{LO}} \xi_{LO}(\vec{\rho}_3)$ . These fields are spatially integrated with respect to the position vector  $\vec{\rho}_3$  lying on the photodetector (PD) surface.

The second term  $\mathbf{n}(t)$  is a circulo-complex white Gaussian noise process with the following statistics:

- $\langle \mathbf{n}(t) \rangle = \mathbf{0}$
- $\langle \mathbf{n}(t) \mathbf{n}^*(u) \rangle = \frac{h\nu_o}{\eta} \delta(t - u)$ .

The parameter  $\eta$  is the photodetector's quantum efficiency and  $h$  is Planck's constant. This noise term is the normalized local-oscillator shot-noise at the receiver front-end. The shot-noise contributions from the received optical return and background light are neglected in lieu of the dominant local oscillator field.

Traditionally, the analyst would propagate the return echo  $\mathbf{U}_E(\vec{\rho}_2, t) = \mathbf{U}_P(\vec{\rho}_2) \cdot \mathbf{T}(\vec{\rho}_2, t)$ , back from the target through the receiver aperture to the photodetector

surface (PD) in order to evaluate the heterodyne mixing integral. However, the antenna theorem [36] states that (5.5) maybe evaluated by integrating the product of the return echo  $U_E(\vec{\rho}_2, t)$  at the  $\mathcal{T}$  plane with the local oscillator spatial mode  $\xi_{LO}^*(\vec{\rho}_3)$  propagated to the  $\mathcal{T}$  plane. This back propagation is understood to take place in the sense that the LO spatial mode also travels through free-space alongside the transmitter beam to the target. If we assume the local oscillator spatial mode is matched to the transmitter spatial mode at the transmitter/receiver aperture (that is,  $\xi_{LO}^*(\vec{\rho}_1) = \xi_T(\vec{\rho}_1)$ ), then the back propagated local oscillator field becomes  $\sqrt{P_{LO}}\xi_P(\vec{\rho}_2)$  at the plane  $\mathcal{T}$  and the mixing integral is then

$$\mathbf{y}(t) = \sqrt{P_T} \int_{\mathcal{T}} d\vec{\rho}_2 \xi_P^2(\vec{\rho}_2) \mathbf{T}(\vec{\rho}_2, t). \quad (5.6)$$

This description of heterodyne reception will be used as a starting point for the projection moment calculations in the next section.

#### 5.1.4 Post-Detection Image Processing

Having reached the end of the signal path, we now complete the DTI imaging model with a discussion of the post-detection image processing. The details of projection extraction from the received signal are shown in Figure 5.2.

As the target completes one revolution, our goal is to gather  $N$  reflectance projections. We approach this semi-discrete problem by sampling the received heterodyne output signal  $\mathbf{r}(t)$  at regular time intervals. The set of sampling instants correspond to equiangular increments of the target rotation.

Each sample consists of a short duration record of the received signal  $\mathbf{r}(t)$ . The  $n^{\text{th}}$  record is formed by multiplying the received signal by a window centered on the sampling instant  $t_n = \theta_n/\Omega$  where  $\theta_n$  is the angle of the  $n^{\text{th}}$  projection  $p_{\theta_n}(\nu)$ . To ease the mathematical analysis in the next section where we take projection moments, we

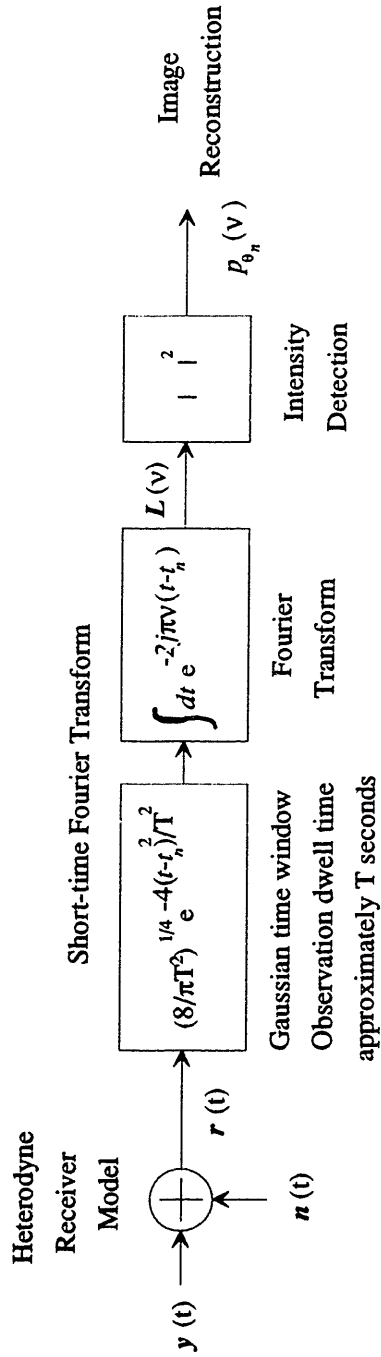


Figure 5.2:

Figure 5.2: Post-Detection Image Processing

have chosen a Gaussian profiled time window. The parameter  $T$  is the projection observation dwell time.

Each projection  $p_{\theta_n}(\nu)$  is then formed by computing the magnitude-squared frequency spectrum of the associated signal record. This results in projections which are proportional to the Doppler return spectrum of the rotating target. Finally, the projection independent variable  $\nu$  (Hz) is transformed into the cross-range variable  $r$  by the Doppler relation  $\nu = 2r\Omega/\lambda$ . Thus, the set of projections is a train of the magnitude-squared Fourier transforms of the Gaussian time windowed signal  $\mathbf{r}(t)$ .

The  $N$  projections will be subjected to standard tomographic reconstruction techniques to form a reflectance image of the spherical target. In the next section we turn our attention to calculating the first and second moments of the projections  $p_{\theta_n}(\nu) \Big|_{\nu=2r\Omega/\lambda}$ .

## 5.2 Projection Statistics

In this section we outline the calculations describing the first and second moment statistics of the projections provided by the above DTI imaging model. An investigation into the time dependent heterodyne return correlation reveals a separable structure, which is exploited in formulating the heterodyne return power spectrum and deriving the projection mean. The resulting projection first moment clearly demonstrates the interplay between dwell time duration and spatial resolution and begins to hint at some of the image distortion issues involved in reconstruction. Finally, a similar analysis is performed to determine the second moments of both filtered and unfiltered projections. At this point in the discussion, we begin with the derivation of the projection mean  $\langle p_{\theta_n}(\nu) \rangle$ .



Referring to Figure 5.2 we see that the projection mean can be written as

$$\begin{aligned} \langle p_{\theta_n}(\nu) \rangle &= \langle \mathbf{L}(\nu) \mathbf{L}^*(\nu) \rangle \end{aligned} \quad (5.7)$$

$$\begin{aligned} &= \left\langle \int_{-\infty}^{\infty} du \left( \frac{8}{\pi T^2} \right)^{\frac{1}{4}} \mathbf{r}(u) e^{-2\pi j\nu(u-t_n)} e^{-4(u-t_n)^2/T^2} \times \right. \\ &\quad \left. \int_{-\infty}^{\infty} dv \left( \frac{8}{\pi T^2} \right)^{\frac{1}{4}} \mathbf{r}^*(v) e^{+2\pi j\nu(v-t_n)} e^{-4(v-t_n)^2/T^2} \right\rangle \\ &= \int_{-\infty}^{\infty} du \int_{-\infty}^{\infty} dv \langle \mathbf{y}(u) \mathbf{y}^*(v) \rangle e^{-2\pi j\nu(u-v)} \left( \frac{8}{\pi T^2} \right)^{\frac{1}{2}} e^{-4((u-t_n)^2+(v-t_n)^2)/T^2} + \\ &\quad \int_{-\infty}^{\infty} du \int_{-\infty}^{\infty} dv \langle \mathbf{n}(u) \mathbf{n}^*(v) \rangle e^{-2\pi j\nu(u-v)} \left( \frac{8}{\pi T^2} \right)^{\frac{1}{2}} e^{-4((u-t_n)^2+(v-t_n)^2)/T^2} \end{aligned} \quad (5.8)$$

$$= \langle p_{\theta_n}(\nu) \rangle_y + \langle p_{\theta_n}(\nu) \rangle_n \quad (5.9)$$

where we have used the statistical independence of the return  $\mathbf{y}(t)$  and the noise  $\mathbf{n}(t)$ . The second double-integral in (5.8) is the local oscillator shot noise contribution to the projection mean. Recalling that we have normalized by the local oscillator power, a straightforward calculation reveals this contribution to be  $h\nu_o/\eta$ . This constant value provides no information about the target, and therefore, will be neglected in our theoretical analysis. However, in actual image reconstruction systems, the effect of this bias can be removed by subtracting  $h\nu_o/\eta$  from each projection. It is the first double-integral that formulates the target return component of the projection mean. The challenge is to evaluate and interpret this double-integral involving  $\langle \mathbf{y}(u) \mathbf{y}^*(v) \rangle$ .

Substituting equation (5.6), the heterodyne return component, this inner expectation can be written as

$$\langle \mathbf{y}(u) \mathbf{y}^*(v) \rangle = \int_T d\vec{\rho}_2 \int_T d\vec{\rho}_2' P_T \xi_P^2(\vec{\rho}_2) [\xi_P^*(\vec{\rho}_2')]^2 \langle \mathbf{T}(\vec{\rho}, u) \mathbf{T}^*(\vec{\rho}_2', v) \rangle \quad (5.10)$$

where the expectation is taken over the random microscopic surface fluctuations of the sphere.

Before evaluating the above covariance, let us consider the relationship between the different physical processes which give rise to the return signal  $\mathbf{y}(t)$ . Intuitively, the *statistical* behavior of this signal can be broken down into two largely independent factors which correspond to physical processes which take place over relatively short- and long-term time scales, respectively. This separation is natural when one realizes that return variations, rising from the passing of speckle lobes over the receiver aperture, have nearly stationary statistics over time scales in which there is little apparent motion of the surface reflectivity distribution over the target. In other words, under super-Doppler resolution conditions in which the dwell time  $T$  is chosen sufficiently small to render negligible surface feature motion over the expose face of the target, the heterodyne signal statistics are stationary during the dwell time, with first and second moments which depend upon the target aspect or projection angle. Therefore, on the longer time scale stretching over an inter-projection sampling period, we would expect each average DTI projection to match with some type of Radon transform of the target reflectivity taken at an aspect corresponding to the projection angle.

This approach is formalized by applying the Schell approximation to the heterodyne component covariance formulation [40]:

$$\langle \mathbf{y}(u) \mathbf{y}^*(v) \rangle \equiv K\left(\frac{1}{2}(u+v), u-v\right) \approx \text{var}\left(\frac{1}{2}(u+v)\right) \cdot k(u-v)$$

where the speckle decorrelation modelled by  $k(u-v)$  falls off much more quickly than  $\langle |\mathbf{y}(\frac{1}{2}(u+v))|^2 \rangle \equiv \text{var}\left(\frac{1}{2}(u+v)\right)$  which accounts for the return fluctuations caused by the motion of the reflectivity distribution.

For the sake of convenience, we separate the short- and long-term time scales by adopting the following sum and difference time coordinates according to our standard

pattern

$$u = t_n + \tau/2$$

$$v = t_n - \tau/2$$

where the time coordinate  $t_n$  now accounts for long-term projection evolution while  $\tau$  describes short-term speckle return variations. Defining the return power spectrum to be the Fourier transform of the Schell approximation with respect to the small time scale changes,  $\tau$ , we have, at time  $t_n$ :

$$\begin{aligned} S(t_n, f) &= \int_{-\infty}^{+\infty} d\tau \langle \mathbf{y}(t_n + \frac{1}{2}\tau) \mathbf{y}^*(t_n - \frac{1}{2}\tau) \rangle e^{-2\pi j f \tau} \\ &= \frac{P_T k^2 a_o^2}{4\pi L^2} \times \pi a_o^2 \times \frac{1}{4\pi L^2} \\ &\quad \frac{16\pi k \rho_T^2}{\Omega} \int_{-\infty}^{+\infty} d\rho_z \rho\left(\left(\frac{\lambda}{2\Omega} f, \rho_z\right), t_n\right) \underbrace{\exp\left\{-\left(\rho_z^2 + \left(\frac{\lambda}{2\Omega} f\right)^2\right)/b^2\right\}}_{\text{Two-Dimensional Gaussian Window Function}} \end{aligned} \quad (5.11)$$

where we have defined

$$b^2 = \frac{1}{\frac{2}{a_T^2} + \frac{k^2 \rho_T^2}{R_T^2}}. \quad (5.12)$$

The missing details behind the derivation of the above result are supplied in §1 and §2 of Appendix C. As in the RTI case, this result assumes the assumptions of spotlight mode target illumination,  $R_T \ll L$  and  $\rho_T \ll a_T$ .

Recalling the RTI mean projection discussion, the right-hand-side of the above result is written in the standard radar equation formulation where the first factor is the on-axis target irradiance, the second is the effective aperture area of the monostatic heterodyne receiver and the third factor is the Doppler frequency  $f$  resolved target cross-section divided by  $4\pi L^2$ . The integral component is single-dimensional and

taken with respect to the  $T$ -plane spatial variable  $\rho_z$  lying parallel to the target rotation axis. Just as in the RTI analysis,  $\rho(\vec{\rho}_z, t_n)$  is the transverse orthographic  $T$ -plane projection of the exposed three-dimensional surface reflectivity distribution  $\rho(x, y, z)$  after the target has rotated through an angle of  $\Omega t_n$  radians. The spatial coordinates of this two-dimensional projection are written in terms of the dimension  $\rho_z$  and the cross-range dimension  $\frac{\lambda}{2\Omega} f$  which corresponds to  $\rho_x$ . The second integrand factor is the same circular two-dimensional Gaussian weighting function discovered during the course of the RTI investigation which serves to model the effects of surface roughness-aspect angle as modelled through the parameter  $b$ . The interpretation of the role of this factor is identical to that of the RTI case.

Piecing these observations together, the integral collapses the weighted “side-projected” reflectivity onto the cross-range axis, and must, therefore, be some type of Radon transform. The transform line integral is taken along the  $\rho_z$ -axis giving one-dimensional projections which are a function of the cross-range dimension  $\frac{\lambda}{2\Omega} f$  and time,  $t_n$ , which directly corresponds to the projection angle,  $\theta_n$ . Therefore, the return power spectrum is directly proportional to a radar line-of-sight cross-range reflectivity projection. This set of variable metric projections is called a generalized Radon transform [27, §II.7].

Returning to the projection mean analysis, we substitute the inverse Fourier transform of the statistical power spectrum into the initial expression (5.8) for the projection first moment and, by performing the indicated operations, we find the first moment to be:

$$\begin{aligned} \langle p_{\theta_n}(\nu) \rangle_y \Big|_{\nu = \frac{2r\Omega}{\lambda}} &= \left[ \sqrt{\frac{\pi T^2}{2}} \exp \left\{ -\frac{1}{2} r^2 / \frac{1}{k^2 \Omega^2 T^2} \right\} \right] \star \\ &\left[ \frac{P_T \rho_T^2}{\pi a_L^4} \int_{-\infty}^{\infty} d\rho_z \rho_{t_n}(r, \rho_z) \exp \{ -(\rho_z^2 + r^2)/b^2 \} \right]. \end{aligned} \quad (5.13)$$

This result assumes that the exposed distribution of the target reflectivity suffers from little apparent motion during the observation dwell time. Note that we have expressed the mean as a convolution of two functions with respect to the cross-range variable  $r$ . The first function is a one-dimensional Gaussian form whose width is inversely proportional to the product of the laser wavenumber  $k$ , the target rotation rate  $\Omega$  and the observation dwell time  $T$ . The second function is the generalized Radon transform of the projected reflectivity as formulated within the power spectrum expression. (The reflectivity subscript  $t_n$  denotes the projection's time dependence.) Recalling the flashlight-ball *gedanken* experiment, this is a cross-range projection of a "net" reflectivity distribution which takes into account the joint issues of aspect and surface roughness. The convolution then smears this projection with an instrument function whose spatial resolution is inversely proportional to the observation dwell time. It is the width of this instrument function which will ultimately determine the final resolution of the reconstructed image.

Let us turn our attention now to the projection covariance. As mentioned previously, the receiver aperture speckle coherence time is a fraction of the observation dwell time. Therefore, the correlation from one projection to the next will be negligible and the second moment of any consequence will be the projection self-covariance. Making the same arguments and assumptions as above in the analysis of the first moment and applying Gaussian moment factoring, §3 of Appendix C demonstrates the projection covariance to be:

$$K_{pp}(r_1, r_2) \approx \left[ \frac{h\nu_o}{\eta} + \sqrt{\frac{\pi T^2}{2}} \frac{P_T \rho_T^2 b^2}{a_L^4 k \Omega T \sigma} \rho \exp \left\{ -\frac{1}{2} \frac{(r_1 + r_2)^2}{4\sigma^2} \right\} \right]^2 \times \exp \left\{ -(r_1 - r_2)^2 / \frac{4}{k^2 \Omega^2 T^2} \right\} \quad (5.14)$$

where

$$\sigma^2 = \frac{b^2}{2} + \frac{1}{k^2\Omega^2T^2}. \quad (5.15)$$

This result was obtained by assuming a low contrast model for the target reflectivity, i.e.,  $\rho(x, y, z) = \rho + \delta\rho(x, y, z)$  where  $|\delta\rho(x, y, z)| \ll \rho$ . This simplification was adopted in order to give closed-form expressions for the spatial integrals over the target surface during Fraunhofer propagation.

Note that this result is the product of two factors. The first factor is the square of the sum of two terms. The first term  $h\nu_o/\eta$  accounts for the LO shot-noise contribution to the projection covariance while the second term adds in the target's speckle contribution. The non-negligible support of this last term is equal to the parameter  $\sigma$ , the radar resolved target extent. This implies that  $\sigma^2$  is proportional in some manner to the unresolved target cross-section. The second factor in the above product is written as a function of the spatial coordinate difference,  $r_1 - r_2$ . Therefore, the projection decorrelation length is equal to  $\sqrt{2}/k\Omega T$ .

The variance for projections processed by the inverse Radon transform reconstruction filter  $H(f) = |f|$  is also calculated in Appendix C §2. Assuming the reasonable case of useful spatial resolution (i.e., the super-resolution condition  $1/k\Omega T \ll \sigma$ ), the filtered projection variance is found to be:

$$\text{var}_{p'p'}(r) \approx \frac{k^2\Omega^2T^2}{8\pi^2} \left[ \frac{h\nu_o}{\eta} + \sqrt{\frac{\pi T^2}{2}} \frac{P_T \rho_T^2 b^2}{a_L^4 k \Omega T \sigma} \rho \exp \left\{ -\frac{1}{2} \frac{(r_1 + r_2)^2}{4\sigma^2} \right\} \right]^2. \quad (5.16)$$

This result also assumes the low contrast reflectivity model of the previous result.

As in the RTI analysis, the first and second moments will be used in the next section to formulate a SNR-like figure of merit for reconstructed images.

### 5.3 Reconstructed Image Performance

In this final section, as in the case of the RTI analysis, we will find it convenient to characterize the reconstructed image distortion performance in terms of a PSF and the image noise performance in terms of a SNR.

In defining an appropriate PSF, we must deal with the same issues encountered during the RTI discussion in working with the  $\mathcal{T}$ -plane transverse orthographic projections of the target reflectance in the course of taking Radon transforms. Therefore, the set of Doppler resolved projections  $p_{\theta_n}(r)$  should be rewritten as a Radon transform of the polar projected reflectivity,  $\rho_{\text{polar}}$ , before attempting to formulate the imaging system PSF. This action places both the RTI and DTI PSF analysis on a common basis, which will then allow direct performance comparisons. Beginning with the line integral description of the  $\mathcal{T}$  plane projected reflectivity, this step gives the mean as

$$\begin{aligned} \langle p_{\theta_n}(r) \rangle &= \frac{P_T \rho_T^2}{\pi a_L^4} \sqrt{\frac{\pi T^2}{2}} \exp \left\{ -r^2 / \frac{2}{k^2 \Omega^2 T^2} \right\} * \\ &\int_{-\infty}^0 dy \underbrace{\frac{y}{\sqrt{R_T^2 - r^2 - y^2}}}_{\text{Aspect Metric}} e^{-[R_T^2 - y^2]/b^2} \rho_{\text{polar}}(x'_{\theta_n}(r, y), y'_{\theta_n}(r, y)) \quad (5.17) \end{aligned}$$

where the polar projection  $\rho_{\text{polar}}$  is written in the  $(x', y')$  coordinate system rotated  $\theta_n$  radians about the  $z$ -axis, the surface aspect metric is introduced through the change of variables from  $\rho_z$  to  $y$  on the target surface and the exponential factor accounts for the surface roughness–aspect angle effect upon the optical return. Thus, this integral is a generalized Radon transform which weights contributions near the equator over those from the polar regions.

This formulation gives us the means to write the average reconstructed DTI image in terms of the convolution of the PSF with the polar reflectivity projection. Applying

the same PSF construction prescription as in the RTI analysis for the response at the point  $(x_o, y_o)$  assuming a Lambertian target, we find:

$$\begin{aligned}
 H(x, y, x_o, y_o) = & \sqrt{\frac{\pi T^2}{2}} \frac{P_T \rho_T^2}{\pi a_L^4} \frac{r_o}{\sqrt{R_T^2 - r_o^2}} \times \\
 & \frac{2\pi}{N} \sum_{\substack{n=0, \theta_n \in \\ [-\theta_o, \pi - \theta_o]}}^{N-1} \underbrace{\sin(\theta_n + \theta_o)}_{\text{Aspect Angle}} \underbrace{\mathcal{H}\left[e^{-[r - r_o \cos(\theta_n + \theta_o)]^2 / \kappa^2 \bar{n}^2 T^2}\right]}_{\text{Reconstruction Projection Prefiltering}} (x \cos \theta_n + y \sin \theta_n) \quad (5.18)
 \end{aligned}$$

where the dependence upon  $(x_o, y_o)$  is expressed through the polar coordinates  $r_o^2 = x_o^2 + y_o^2$  and  $\tan^{-1} \theta_o = y_o/x_o$ .

The interpretation of this result is very similar to the RTI result. The operator  $\mathcal{H}$  is the inverse Radon transform projection prefiltering operator  $\mathcal{F}^{-1}[|f| \times \mathcal{F}(p_\theta(r))]$ . It is applied to the dwell time smeared Gaussian projections of the delta function. The sine function models the projection angle dependent effect of surface aspect change throughout target rotation. Note that as a feature apparently travels from one target limb to the other, the corresponding contribution from this sine term goes from zero to unity on-axis and back down to zero at the far limb. These factors are combined under the backprojection summation sign to produce an unscaled PSF. This result is then scaled by various familiar laser radar engineering parameters and an additional factor which depends upon the original position  $(x_o, y_o)$  of the delta function. This last factor accounts for the latitudinal dependence of the surface aspect surrounding the delta function. Therefore, these observations lead to the same conclusion drawn for the RTI PSF, namely, that the DTI PSF is *not* position independent and the mean image must be recovered by a superposition integral rather than through the convolution operation.



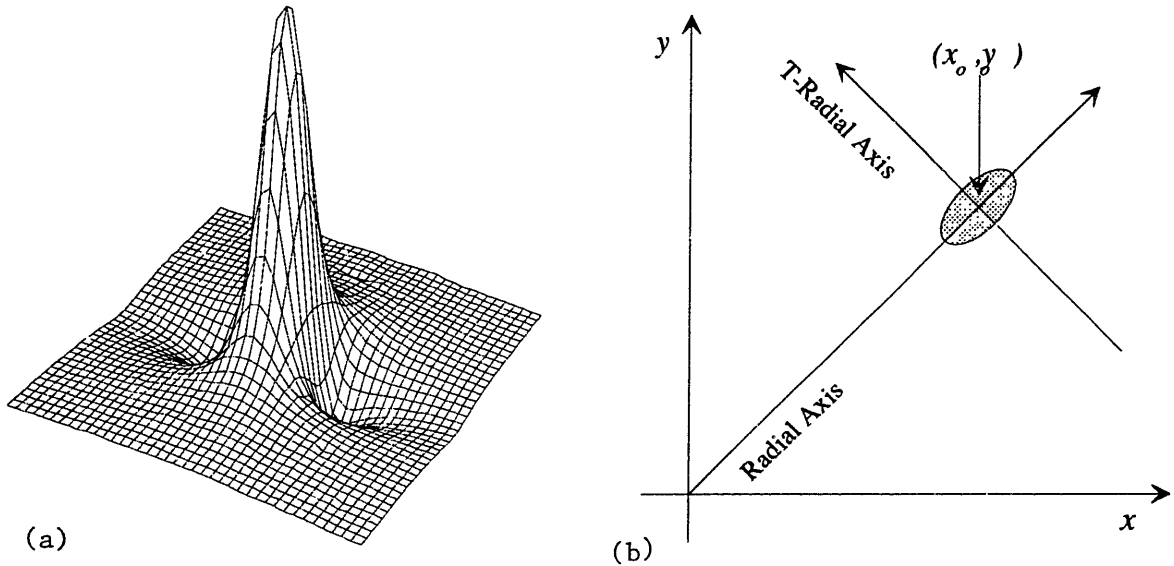


Figure 5.3: (a) PSF Reconstruction for  $N = 144$  Projections. (b) PSF Orientation.

The presence of the sine function under the backprojection summation makes a closed form solution of (5.18) difficult to calculate. However, the normalized PSF has been numerically calculated and the result is shown in Figure 5.3. The result is a dumbbell-shaped PSF which has zero amplitude when located at the origin but blows-up at the equator. The PSF major axis lies along the radial axis protruding from the origin. The major and minor axes lengths of the half-maximum half-width dumbbell contour are approximately 1.5 and 1.0 times  $1/k\Omega T$ . Therefore, the reconstructed DTI image will have finer resolution with respect to the transverse radial axis than along the radial axis. Thus, we define  $1/k\Omega T$  to be the nominal DTI resolution.

Having demonstrated the resolution of the DTI imaging system, we now begin an investigation of the reconstructed image noise performance via an appropriate formulation of a signal-to-noise ratio. As in the previous chapter, we adopt the same

SNR definition as a measure of reconstruction quality:

$$\text{SNR}(x_o, y_o) = \frac{\delta f^2(x_o, y_o) \left| \int dx \int dy H(x, y, x_o, y_o) \right|^2}{\text{var} \{ \text{Reconstructed Image at } (x_o, y_o) \}} \quad (5.19)$$

On a pointwise basis, this measure contrasts the relative strength of the mean image to the average strength of noise induced fluctuations for a low-contrast target under super-resolution conditions which adequately resolve the bandlimited surface feature distribution  $\delta f(x_o, y_o)$ .

As demonstrated in Appendix C §3, projections are statistically independent, the variance in the numerator can be found by backprojecting the filtered projection variance (5.16) over the entire circle of projection angles. As in the RTI case, for a handful of resolution cells across the target, the number of required projections is on the order of 20–25. Under this condition, the semi-discrete variance backprojection summations for the shot-noise cross speckle and the speckle cross speckle contributions can be closely approximated by a factor proportional to  $N e^{-r_o^2/2\sigma^2} I_0(r_o^2/2\sigma^2)$  and  $N e^{-r_o^2/\sigma^2} I_0(r_o^2/\sigma^2)$ , respectively, resulting in a closed form expression for the SNR, where  $I_0$  is the zeroth order modified Bessel function.

Taking these approximations results in the following low-contrast super-resolution SNR:

$$\text{SNR}(x_o, y_o) = \frac{\delta f^2(x_o, y_o) N \left( \frac{1}{k\Omega T} \frac{b^2}{\sigma} \right)^2 \text{CNR} \cos^2 \psi / 16\pi^3}{\underbrace{e^{-r_o^2/\sigma^2} / \text{CNR}}_{1^{\text{st}}} + \underbrace{2\rho e^{-3r_o^2/4\sigma^2} I_0(r_o^2/4\sigma^2)}_{2^{\text{nd}}} + \underbrace{\rho^2 \text{CNR} e^{-r_o^2/2\sigma^2} I_0(r_o^2/2\sigma^2)}_{3^{\text{rd}}}} \quad (5.20)$$

where we have defined the carrier-to-noise ratio (CNR) to be the ratio of the mean

projection to the LO shot-noise spectrum, i.e.,

$$\begin{aligned} \text{CNR} &\equiv \frac{|\langle p(r_o) \rangle|}{(h\nu_o/\eta)} \\ &= \sqrt{\frac{\pi}{2}} \frac{\eta}{h\nu_o} \frac{P_T \rho_T^2}{a_L^4} \frac{b^2}{k\Omega\sigma} e^{-r_o^2/2\sigma^2} \end{aligned} \quad (5.21)$$

where we have normalized by the low-contrast reflectivity component present in the CNR numerator mean response. In the above SNR formulation we have assigned  $\psi$  as the equivalent target latitude of the point  $(x_o, y_o)$ . This resulting CNR dependent SNR formulation conveniently expresses performance in terms of physical measures.

Thus, the filtered backprojection reconstructed DTI image SNR is directly proportional to the number of projections,  $N$ , the square of the number of radial resolution cells,  $q = b^2/k\Omega T\sigma$  and the cosine squared of the latitude  $\psi$ . The SNR is inversely proportional to the sum of three terms, the shot-noise  $\times$  shot-noise, the shot-noise  $\times$  speckle and the speckle  $\times$  speckle in that order. As the CNR grows with increasing transmission power, the SNR will grow beyond the shot-noise limit imposed by the first two denominator terms and eventually saturate at a new level determined by speckle.

Thus, in the high CNR regime, the speckle-limited SNR takes the following value:

$$\frac{\delta f^2(x_o, y_o) N \left( \frac{1}{k\Omega T} \left/ \frac{b^2}{\sigma} \right. \right)^2 \text{CNR} \cos^2 \psi / 16\pi^3}{\rho^2 \text{CNR} e^{-r_o^2/2\sigma^2} I_0(r_o^2/2\sigma^2)} \quad (5.22)$$

This speckle limit rises from a value of zero at the reconstructed image center to a peak value at the image boundary. As in the RTI case, presuming the absence of angle-angle resolution, the typical DTI imaging scenario achieving a handful of radial resolution cells across a Lambertian target requires a large number of projections, on the order of several thousand, to drive the SNR up to  $\delta f^2(x_o, y_o)/\rho^2$ , the conventional low-contrast speckle-limited laser radar resolved-pixel SNR.



## Chapter 6

# Comparison with Experimental Results

This chapter discusses a comparison between the theoretical PSF performance predictions of the past two chapters and the RTI and DTI work performed at the Laser Radar Measurements group at the M.I.T. Lincoln Laboratory.

Researchers at this facility have noted that reconstructed RTI images tend to emphasize target boundaries, leaving interior regions unresolved, while DTI images take on a target silhouette-like appearance where, to the contrary, boundaries have been de-emphasized and smoothed [37]. Kulkarni, *et al*, investigated these effects by reconstructing simulated RTI and DTI images of a cylindrical target rotating about the major axis ( $z$ -axis). Their results, reproduced in Figure 6.1, are RTI ((a), (c)) and DTI ((b), (c)) images for both a Lambertian surface ((a), (b)) and a second surface ((c), (d)) which only exhibits strong reflectance a grazing angles of incidence (i.e., their “non-physical BRDF” target). These figures plainly show for Lambertian surfaces that indeed RTI resolves target outlines while DTI produces smoothed target silhouettes.

Even though our analysis used a number of approximations during the devel-

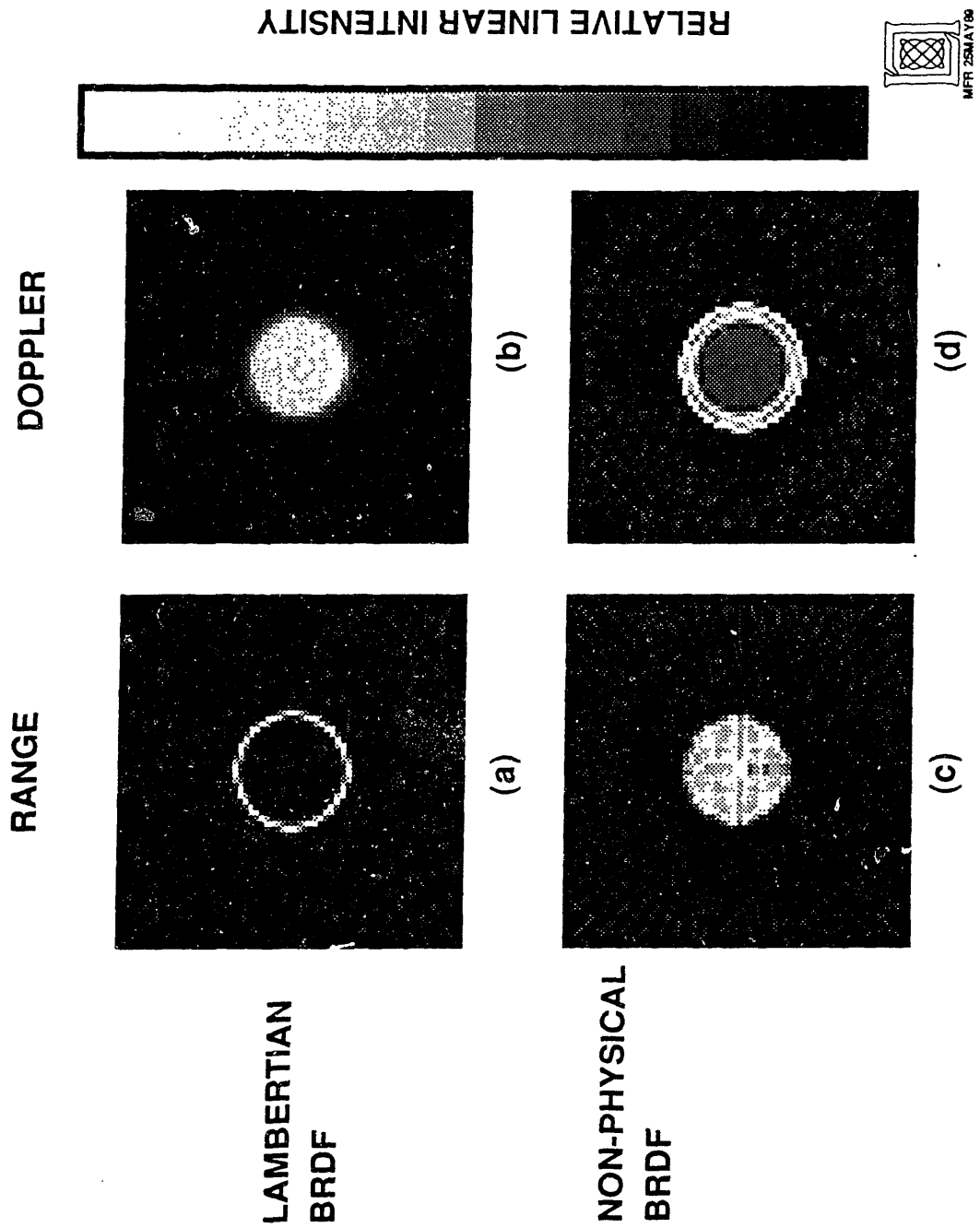


Figure 6.1: Comparison of RTI and DTI Reconstructions

opment of the RTI and DTI results, the above patterns can now be qualitatively explained in light of the analysis of the previous two chapters. For the case of RTI, the *trans-radial* orientation of the dumbbell-shaped PSF means that details along the radial axis will be resolved. Therefore, RTI imaging will highlight the target outline. On the other hand, the *radial* orientation of the similarly dumbbell-shaped DTI PSF will tend to smear radial details. Therefore, DTI imaging will soften the projected target boundary and fill the reconstruction interior. In our imaging model, if we assume that a non-negligible uniform reflectance confined to an equatorial belt about the spherical target approximates the simulated cylindrical target in [37], then on a qualitative basis, the above RTI and DTI reconstruction behavior is confirmed by the results of Figure 6.1.

Note that RTI and DTI performance is reversed for the “non-physical” target. Again, this dual behavior is predicted by our PSF formulations. The strong return at grazing angles of incidence corresponds to responses taken along the trans-radial axis of the RTI and DTI PSF’s. At these orientations, the RTI and DTI PSF’s are respectively, relatively wide and narrow. Therefore, we would expect the DTI reconstruction to resolve the target boundary while the RTI image would approximate a silhouette. Again, this prediction is supported qualitatively by the simulated reconstructions in Figure 6.1.





# Chapter 7

## Conclusions

This dissertation analyzes the statistical performance of both direct-detection RTI and heterodyne detection DTI tomographic laser radar imaging systems in the presence of speckle and photodetector shot-noise. This was accomplished by constructing dual mathematical models for each system when interrogating a rotating diffuse spherical target sited in the radar's optical far-field, and then calculating first and second projection moments. These moments were used to develop two measures of reconstructed image quality: the point-spread-function (PSF) and the pointwise signal-to-noise ratio (SNR), which characterized distortion and noise performance, respectively.

The resolution capabilities of both RTI and DTI are indicated by the contours of their associated PSF's. In each case, the dumbbell-shaped PSF response peaked on the equator of the spherical target and then fell to zero at the poles. This behavior is readily explained by the effect of surface foreshortening as one moves from the equator toward either pole. The nominal half-height half-width resolution cell size is on the order of  $c/B_1$  and  $1/k\Omega T$  for RTI and DTI, respectively. The cross orientation of the RTI and DTI PSF's predicts that range-resolved imaging will reconstruct target boundaries while Doppler-resolved imaging will produce smoothed target silhouettes.

These predictions are in agreement with the simulations performed by others.

The noise performance of both RTI and DTI systems was written in terms of a carrier-to-noise (CNR) formulation of the reconstructed image SNR. In each case the CNR was conveniently defined as a measurable physical quantity which entailed many of the model parameters. For RTI, performance was limited at low transmission power levels by presence of photodetector thermal noise and dark current. Local-oscillator shot-noise limited DTI SNR performance at low transmission levels. However, in the high transmitter power regime, radially dependent speckle SNR limits were identified for both RTI and DTI. In both cases, this speckle limit was found to be directly proportional to the number of projections and inversely proportional to the square of the number of radial resolution cells across the target. Therefore, in the speckle limit, these imaging techniques incoherently average speckle noise via tomographic backprojection reconstruction while retaining all of the inherent resolution capabilities of their underlying range- or cross-range-resolving systems. However, in scenarios achieving a handful of radial resolution cells with a modest number of projections, the SNR performance of both imaging systems was found to be below both unity and the conventional low-contrast speckle-limited laser radar resolved-pixel SNR.

Beyond the results presented here, this work may be an appropriate foundation for proceeding with a more general analysis. As implied during the error analysis at the end of chapter 3, a projection gathering system in which the target reflectance is regarded as a deterministic function could be modelled by attempting to meld the distortion and noise issues by adopting a mean-squared-error (MSE). This quantity would sum an image bias term, a measure of the departure of the system PSF from the ideal two-dimensional delta function PSF, and a second variance term which would account for the reconstruction noise strength. We could then imagine generalizing this

model by relaxing the deterministic restriction on the target reflectance and assuming an appropriate random model. In this case, one could compute the MSE over the reflectance ensemble by taking conditional expectations of the bias and variance terms and then minimize this quantity over the system filters to produce an minimum error imaging system design. Finally, one could approach the problem by developing a more general model which removes the tomographic reconstruction assumption to allow optimization over all possible image reconstruction algorithms and target observation strategies.



# Appendix A

This appendix presents the details of the projection cross-correlation calculation discussed in §3.2 for the case of unequal projection angles (i.e.,  $\theta_1 \neq \theta_2$ ). Beginning with equation (3.9) we have

$$\begin{aligned}
 & \langle \mathbf{R}(r_1, \theta) \mathbf{R}^*(r_2, \theta) \rangle \\
 &= \left\langle \int_{-\infty}^{\infty} \int_{-\infty}^{\infty} dx'_1 dy'_1 s(x_1(x'_1, y'_1), y_1(x'_1, y'_1)) b_r(x'_1, y'_1) e^{2jk(R+y'_1)} \right. \\
 & \quad \left. \int_{-\infty}^{\infty} \int_{-\infty}^{\infty} dx'_2 dy'_2 s^*(x_2(x'_2, y'_2), y_2(x'_2, y'_2)) b_r(x'_2, y'_2) e^{-2jk(R+y'_2)} \right\rangle \quad (3.9), \quad (\text{A.1}) \\
 &= \int_{-\infty}^{\infty} \int_{-\infty}^{\infty} dx'_1 dy'_1 f(x_1(x'_1, y'_1), y_1(x'_1, y'_1)) \\
 & \quad \exp(2jk y'_1) \exp(-2jk[-x'_1 \sin(\theta_1 - \theta_2) + y'_1 \cos(\theta_1 - \theta_2)]) \\
 & \quad \frac{1}{\pi r_{\perp}^2} \exp\left(-\frac{(x'_1 - r_1)^2}{r_{\perp}^2}\right) \exp\left(-\frac{(x'_1 \cos(\theta_1 - \theta_2) + y'_1 \sin(\theta_1 - \theta_2) - r_2)^2}{r_{\perp}^2}\right) \\
 & \hspace{20em} (\text{A.2})
 \end{aligned}$$

where the cross-correlation is now written in terms of the  $(x'_1, y'_1)$  Cartesian coordinate system (cf. Figure 3.2 and Figure A.1). Suppose that in the  $(x'_1, y'_1)$  coordinate system the scan lines  $(r_1, \theta_1)$  and  $(r_2, \theta_2)$  intersect at the point denoted as  $(x'_x, y'_x)$ . Solving for these coordinates,

$$\begin{aligned}
 x'_x &= r_1 \\
 y'_x &= r_2 \csc(\theta_1 - \theta_2) - r_1 \cot(\theta_1 - \theta_2).
 \end{aligned}$$

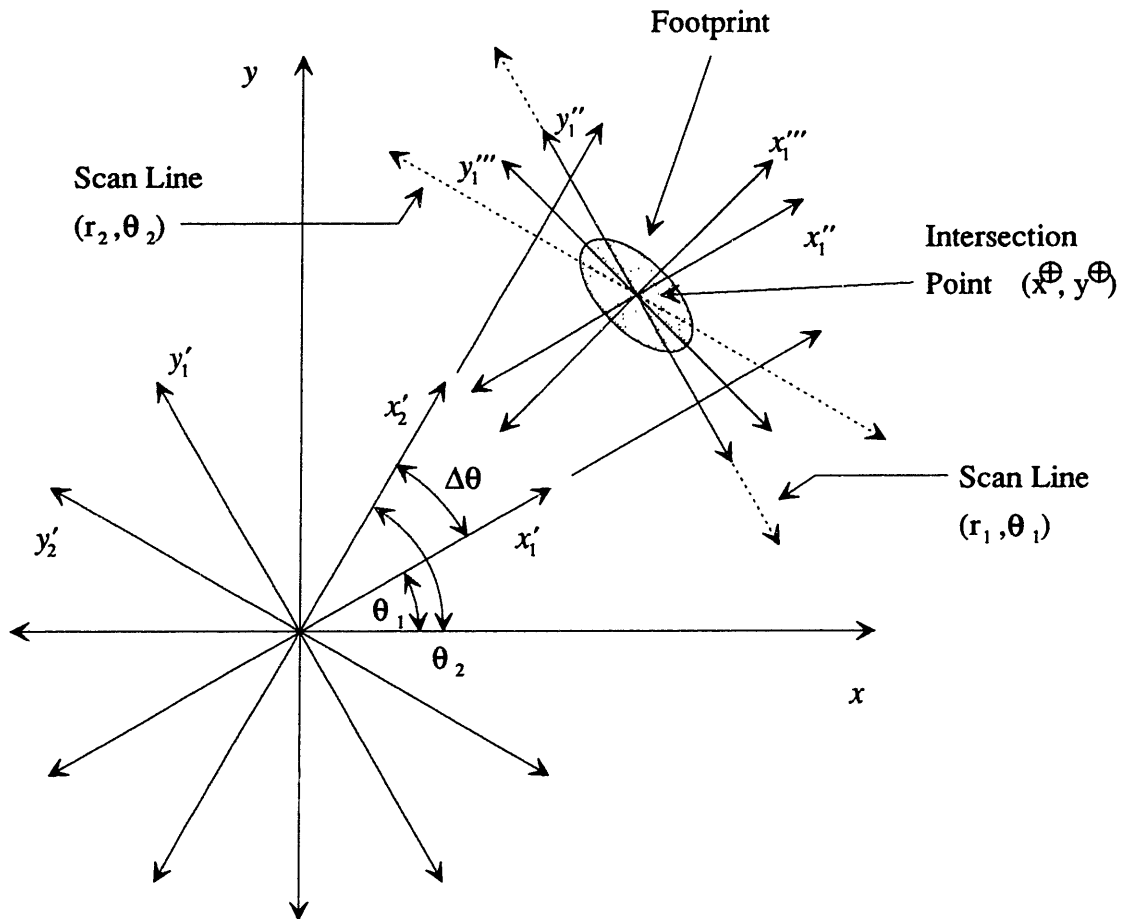


Figure A.1: Placement of the  $(x, y)$ ,  $(x'_1, y'_1)$ ,  $(x''_1, y''_1)$ , and  $(x'''_1, y'''_1)$  Coordinate Systems with respect to the Scan Lines.

We now choose a new Cartesian coordinate system  $(x_1'', y_1'')$  whose axes are parallel to the  $(x_1', y_1')$  coordinate frame and whose origin lies on the scan line intersection point  $(x_x', y_x')$ . This axis translation is thus

$$\begin{aligned} x_1'' &= x_1' - x_x' \\ y_1'' &= y_1' - y_x'. \end{aligned}$$

Expressing the cross-correlation in terms of this new coordinate system:

$$\begin{aligned} &\langle \mathbf{R}(r_1, \theta) \mathbf{R}^*(r_2, \theta) \rangle \\ &= \int_{-\infty}^{\infty} \int_{-\infty}^{\infty} dx_1'' dy_1'' f(x_1(x_1'' + x_x', y_1'' + y_x'), y_1(x_1'' + x_x', y_1'' + y_x')) \\ &\quad \exp(2jk(y_1'' + y_x')) \exp(-2jk[-(x_1'' + x_x') \sin(\theta_1 - \theta_2) + (y_1'' + y_x') \cos(\theta_1 - \theta_2)]) \\ &\quad \frac{1}{\pi r_{\perp}^2} \exp\left(-\frac{(x_1'')^2}{r_{\perp}^2}\right) \exp\left(-\frac{(x_1'' \cos(\theta_1 - \theta_2) + y_1'' \sin(\theta_1 - \theta_2))^2}{r_{\perp}^2}\right). \end{aligned} \quad (\text{A.3})$$

Note the simplified the Gaussian forms. Finally, we rotate the  $(x_1'', y_1'')$  coordinate axes through an angle of  $\Delta\theta/2 = -(\theta_1 - \theta_2)/2$  to form the  $(x_1''', y_1''')$  Cartesian coordinate frame. The origin of  $(x_1''', y_1''')$  lies on the intersection point  $(x_x', y_x')$ ; the  $y_1'''$  axis bisects the two scan lines  $(r_1, \theta_1)$  and  $(r_2, \theta_2)$  at the  $(x_x', y_x')$  intersection point. Rewriting the formulation of the cross-correlation in this final coordinate system, we have

$$\begin{aligned} &\langle \mathbf{R}(r_1, \theta) \mathbf{R}^*(r_2, \theta) \rangle \\ &= \int_{-\infty}^{\infty} \int_{-\infty}^{\infty} dx_1''' dy_1''' \\ &\quad f(x_1(x_1'''(x_1''', y_1''') + x_x', y_1'''(x_1''', y_1''') + x_x'), y_1(x_1'''(x_1''', y_1''') + x_x', y_1'''(x_1''', y_1''') + x_x')) \\ &\quad \exp(2jk(y_1'''(x_1''', y_1''') + y_x')) \\ &\quad \exp(-2jk[-(x_1'''(x_1''', y_1''') + x_x') \sin(\theta_1 - \theta_2) + (y_1'''(x_1''', y_1''') + y_x') \cos(\theta_1 - \theta_2)]) \\ &\quad \frac{2}{|\sin(\theta_1 - \theta_2)|} \left[ \frac{|\sin(\theta_1 - \theta_2)|}{2\pi r_{\perp}^2} \exp\left(-\frac{(x_1''')^2}{r_{\perp}^2 / \cos^2(\Delta\theta/2)}\right) \exp\left(-\frac{(y_1''')^2}{r_{\perp}^2 / \sin^2(\Delta\theta/2)}\right) \right]. \end{aligned} \quad (\text{A.4})$$

Note that the term in brackets on the last line is a two-dimensional Gaussian probability density function (PDF) form centered on the intersection point with major and minor axes lengths which vary with the angle of attack  $\theta_2 - \theta_1$ . The argument of  $f(\cdot, \cdot)$  within the *original*  $(x, y)$  Cartesian coordinate system defined in Figure 3.2 is simply the point  $(x^\oplus, y^\oplus)$ . The rest of the integrand is a complex phase factor. Therefore, asserting the same argument in passing to the Radon transform, if  $r_\perp$  becomes small enough such that  $f$  is smooth under the significant part of the Gaussian PDF footprint, then the cross-correlation may be approximated by

$$\langle \mathbf{R}(r_1, \theta) \mathbf{R}^*(r_2, \theta) \rangle = \frac{2\mathcal{C}}{|\sin(\theta_1 - \theta_2)|} f(x^\oplus, y^\oplus) \quad (\text{A.5})$$

which in magnitude squared becomes

$$|\langle \mathbf{R}(r_1, \theta) \mathbf{R}^*(r_2, \theta) \rangle|^2 = \frac{4}{\sin^2(\theta_1 - \theta_2)} f^2(x^\oplus, y^\oplus). \quad (\text{A.6})$$



# Appendix B

This appendix details the assumptions and approximations behind the development of the RTI mean projection optical power (4.11) and both the RTI projection variance (4.18) and covariance (4.16) for filtered and unfiltered projections, respectively, produced by a Gaussian illumination pulse originating from a radar sited in the target deep far-field and reflecting from a low-contrast surface. These calculations also provide a convenient framework for demonstrating inter-projection statistical independence under typical RTI imaging scenarios. The essence of these derivations is the determination of the return optical field covariance by propagating the target surface covariance via the Fraunhofer diffraction formula.

## B.1 RTI Mean Projection Formulation

In this section we compute the time dependent optical power falling on the receiver photodetector due to the illumination pulse reaching the  $\mathcal{T}$ -plane at time  $t_n$ .

The power  $P(t)$  striking the photodetector is equal to the return electromagnetic field intensity summed over the receiver aperture. Thus, we write

$$P(t) = \int_{\substack{\text{Receiver} \\ \text{Aperture}}} d\vec{\rho}_3 |\mathbf{U}_r(\vec{\rho}_3, t)|^2 \approx \int d\vec{\rho}_3 e^{-|\vec{\rho}_3|^2/a_R^2} |\mathbf{U}_r(\vec{\rho}_3, t)|^2$$

where we have approximated the receiver aperture outline with a circular two-dimen-

sional Gaussian window function of nominal radius  $a_R$  in the aperture plane spanned by the position vector  $\vec{\rho}_3$ .

The return at the receiver plane,  $\mathbf{U}_r(\vec{\rho}_3, t)$ , is found by using the Fraunhofer diffraction formula to propagate the inverse time domain Fourier transform of the  $\mathcal{T}$ -plane echo,  $\mathbf{U}_E(\vec{\rho}_2, f)$ , as formulated in equation (4.10). Since the radar-target separation distance  $L$  is on the order of 100,000 m or more, the typical 10–100 cm receiver objective subtends a very small portion of the spherical paraxial wavefront radiating from any point on the target surface. Under this condition, the incoming wavefront is relatively flat over the aperture as compared to the range variations of interest in the return magnitude. Therefore, we will neglect the  $\vec{\rho}_3$  spatial dependence of the return field magnitude across the receiver aperture while keeping the spatial dependence of the optical phase intact. Furthermore, we will assume that the sub-nanosecond pulse duration will freeze the apparent motion of both the target reflectivity and surface roughness distributions and leave the return Doppler component unresolved.

Applying these assumptions and approximations to the return field calculation and then substituting into the above expression for the return power and taking the mean with respect to the surface roughness randomness results in the following expectation:

$$\begin{aligned}
\langle P(t) \rangle &\equiv \int d\vec{\rho}_3 e^{-|\vec{\rho}_3|^2/a_R^2} \langle \mathbf{U}_r(\vec{\rho}_3, t) \mathbf{U}_r^*(\vec{\rho}_3, t) \rangle \\
&= \int d\vec{\rho}_3 e^{-|\vec{\rho}_3|^2/a_R^2} \left\langle \frac{1}{j\lambda L} \sqrt{\frac{P_T}{\pi a_L^2}} \exp \left\{ jkL + j\frac{k|\vec{\rho}_3|^2}{2L} - j\frac{\pi}{2} \right\} \right. \\
&\quad \left. \frac{-1}{j\lambda L} \sqrt{\frac{P_T}{\pi a_L^2}} \exp \left\{ -jkL - j\frac{k|\vec{\rho}_3|^2}{2L} + j\frac{\pi}{2} \right\} \right\rangle \\
&\int d\vec{\rho}_2 \sqrt{\rho(\vec{\rho}_2, t_n)} s^{1/2} \left( t - t_n - L/c - 2 \left[ R_T - \sqrt{R_T^2 - |\vec{\rho}_2|^2} \right] / c \right)
\end{aligned}$$

$$\begin{aligned}
& e^{jk|\vec{\rho}_2|^2/2L} e^{jk|\vec{\rho}_2|^2/R_T} e^{2jkh(\vec{\rho}_2,t)} e^{-|\vec{\rho}_2|^2/a_T^2} e^{-|\vec{\rho}_2|^2/2a_L^2} e^{-2\pi j\vec{\rho}_3 \cdot \vec{\rho}_2/\lambda L} \\
& \int d\vec{\rho}_2' \sqrt{\rho(\vec{\rho}_2', t_n)} s^{1/2} \left( t - t_n - L/c - 2 \left[ R_T - \sqrt{R_T^2 - |\vec{\rho}_2'|^2} \right] / c \right) \\
& \left. e^{-jk|\vec{\rho}_2'|^2/2L} e^{-jk|\vec{\rho}_2'|^2/R_T} e^{-2jkh(\vec{\rho}_2',t)} e^{-|\vec{\rho}_2'|^2/a_T^2} e^{-|\vec{\rho}_2'|^2/2a_L^2} e^{+2\pi j\vec{\rho}_3 \cdot \vec{\rho}_2'/\lambda L} \right\rangle
\end{aligned}$$

where the quantity  $\rho(\vec{\rho}_2, t_n)$  is the exposed target surface reflectivity frozen in place at time  $t_n$ , and then projected back along the laser radar line-of-sight to the  $T$  plane.

Collecting common terms and exponents, exchanging the order of integration and expectation, we now obtain

$$\begin{aligned}
\langle P(t) \rangle &= \frac{k^2}{4\pi^2 L^2} \frac{P_T}{\pi a_L^2} \int d\vec{\rho}_3 e^{-|\vec{\rho}_3|^2/a_R^2} \int d\vec{\rho}_2 \int d\vec{\rho}_2' \\
& \sqrt{\rho(\vec{\rho}_2, t_n)} s^{1/2} \left( t - t_n - L/c - 2 \left[ R_T - \sqrt{R_T^2 - |\vec{\rho}_2|^2} \right] / c \right) \\
& \sqrt{\rho(\vec{\rho}_2', t_n)} s^{1/2} \left( t - t_n - L/c - 2 \left[ R_T - \sqrt{R_T^2 - |\vec{\rho}_2'|^2} \right] / c \right) \\
& \underbrace{\langle \exp\{2jkh(\vec{\rho}_2)\} \exp\{-2jkh(\vec{\rho}_2')\} \rangle}_{\text{Phase Correlation}} \\
& \exp \left\{ -|\vec{\rho}_2|^2 \underbrace{\left( \frac{1}{2a_L^2} + \frac{1}{a_T^2} \right)}_{\approx 1/a_T^2} \right\} \exp \left\{ -|\vec{\rho}_2'|^2 \underbrace{\left( \frac{1}{2a_L^2} + \frac{1}{a_T^2} \right)}_{\approx 1/a_T^2} \right\} \\
& \exp \left\{ jk(|\vec{\rho}_2|^2 - |\vec{\rho}_2'|^2) \underbrace{\left( \frac{1}{2L} + \frac{1}{R_T} \right)}_{\approx 1/R_T} \right\} \exp\{-jk\vec{\rho}_3 \cdot (\vec{\rho}_2 - \vec{\rho}_2')/L\}. \quad (\text{B.1})
\end{aligned}$$

The above expression can be further simplified by applying several reasonable assumptions. First, since the target is unresolved by the transmitted laser beam, the probe beam radius  $a_L$  is much larger than the target radius  $a_T$ . Therefore, the  $1/2a_L^2$  term may be neglected within the two parenthetical expressions on the fifth line of (B.1). Adopting this approximation builds in the assumption that the target is spot-

light mode illuminated by a pulse which has a uniform cross-range intensity pattern. Second, since the target spherical radius  $R_T$  is much smaller than the separation distance  $L$  between the laser radar and target, the  $1/2L$  term may be discarded from the first parenthetical expression on the sixth line of (B.1). By this action, we are assuming that the far-field probe beam wavefront curvature is negligible compared to the target radius of curvature. Finally, the phase correlation term can be replaced by the approximation introduced in §4.1.2, giving

$$\begin{aligned}
\langle P(t) \rangle &= \frac{k^2}{4\pi^2 L^2} \frac{P_T}{\pi a_L^2} \int d\vec{\rho}_3 e^{-|\vec{\rho}_3|^2/a_R^2} \\
&\int d\vec{\rho}_2 \int d\vec{\rho}_2' \sqrt{\rho(\vec{\rho}_2, t_n)} \sqrt{\rho(\vec{\rho}_2', t_n)} \\
&s^{1/2}(t - t_n - L/c - 2[R_T - \sqrt{R_T^2 - |\vec{\rho}_2|^2}]/c) \\
&s^{1/2}(t - t_n - L/c - 2[R_T - \sqrt{R_T^2 - |\vec{\rho}_2'|^2}]/c) \\
&\underbrace{\exp\left\{-\frac{|\vec{\rho}_2 - \vec{\rho}_2'|^2}{\rho_T^2}\right\}}_{\text{Phase Decorrelation}} \exp\left\{-\frac{|\vec{\rho}_2|^2}{a_T^2}\right\} \exp\left\{-\frac{|\vec{\rho}_2'|^2}{a_T^2}\right\} \\
&\exp\left\{\frac{jk}{R_T}(|\vec{\rho}_2|^2 - |\vec{\rho}_2'|^2)\right\} \exp\left\{-\frac{jk}{L}\vec{\rho}_3 \cdot (\vec{\rho}_2 - \vec{\rho}_2')\right\}. \quad (\text{B.2})
\end{aligned}$$

where we have neglected the movement of the target surface within the correlation factor.

Note that the second through sixth lines of this result are written as a double two-dimensional spatial Fourier transform with respect to the variables  $\vec{\rho}_2$  and  $\vec{\rho}_2'$ . Note that the integrand of this result (line 5, B.2) contributes little to the double transform if the two position vectors  $\vec{\rho}_2$  and  $\vec{\rho}_2'$  lie more than a few surface correlation lengths  $\rho_T$  apart. This behavior is not surprising in light of the fact that returns from separate surface patches will be uncorrelated on the frozen target surface.

We will proceed by attempting to separate, evaluate and interpret the effect of a *very* short surface coherence length versus a substantially larger target by rewriting the two transforms in the following sum and difference coordinate systems:

$$\begin{aligned}\vec{\rho}_2^+ &= \frac{1}{2}(\vec{\rho}_2 + \vec{\rho}_2') \\ \vec{\rho}_2^- &= \vec{\rho}_2 - \vec{\rho}_2'\end{aligned}$$

Applying these transformations leads to

$$\begin{aligned}\langle P(t) \rangle &= \frac{k^2}{4\pi^2 L^2} \frac{P_T}{\pi a_L^2} \int d\vec{\rho}_3 e^{-|\vec{\rho}_3|^2/a_r^2} \int d\vec{\rho}_2^+ \rho(\vec{\rho}_2^+, t_n) \exp\left\{-2 \frac{|\vec{\rho}_2^+|^2}{a_T^2}\right\} \\ &\quad s\left(t - t_n - L/c - 2 \left[ R_T - \sqrt{R_T^2 - |\vec{\rho}_2^+|^2} \right] / c\right) \\ &\quad \int d\vec{\rho}_2^- \exp\left\{-\left(\frac{1}{\rho_T^2} + \frac{1}{2a_T^2}\right) |\vec{\rho}_2^-|^2\right\} \exp\left\{\frac{2jk}{R_T} \vec{\rho}_2^+ \cdot \vec{\rho}_2^-\right\} \exp\left\{-\frac{jk}{L} \vec{\rho}_3 \cdot \vec{\rho}_2^-\right\}\end{aligned}$$

where, in the following manner, we have used the assumption that any surface roughness correlation region is much smaller than the target extent. Since the surface maintains phase correlation over distances of only a few wavelengths, it seems reasonable to assume that the spatial distribution of both the surface reflectivity and the pulse illumination varies slowly across any such surface correlation patch. Thus, in preparation for evaluating the integral with respect to  $\vec{\rho}_2^-$  in equation (B.2) above, we have taken the following approximation:

$$\begin{aligned}&\sqrt{\rho(\vec{\rho}_2^+ + \frac{1}{2}\vec{\rho}_2^-, t_n)} s^{1/2}\left(t - t_n - L/c - 2 \left[ R_T - \sqrt{R_T^2 - |\vec{\rho}_2^+ + \frac{1}{2}\vec{\rho}_2^-|^2} \right] / c\right) \times \\ &\sqrt{\rho(\vec{\rho}_2^+ - \frac{1}{2}\vec{\rho}_2^-, t_n)} s^{1/2}\left(t - t_n - L/c - 2 \left[ R_T - \sqrt{R_T^2 - |\vec{\rho}_2^+ - \frac{1}{2}\vec{\rho}_2^-|^2} \right] / c\right) \\ &\approx \rho(\vec{\rho}_2^+, t_n) s\left(t - t_n - L/c - 2 \left[ R_T - \sqrt{R_T^2 - |\vec{\rho}_2^+|^2} \right] / c\right).\end{aligned}$$

Taking the Fourier transform with respect to the variable  $\vec{\rho}_2^-$  results in

$$\begin{aligned} \langle P(t) \rangle &= \frac{P_T \rho_T^2}{4\pi^2 a_L^2} \underbrace{\left/ \left( \frac{1}{\rho_T^2} + \frac{1}{2a_T^2} \right) \right.}_{\approx \rho_T^2} \times \\ &\int d\vec{\rho}_2^+ \rho(\vec{\rho}_2^+, t_n) s\left(t - t_n - L/c - 2 \left[ R_T - \sqrt{R_T^2 - |\vec{\rho}_2^+|^2} \right] / c\right) \exp \left\{ -2 \frac{|\vec{\rho}_2^+|^2}{a_T^2} \right\} \\ &\int d\vec{\rho}_3 e^{-|\vec{\rho}_3|^2/a_R^2} \frac{k^2}{L^2} \exp \left\{ -\frac{1}{4} k^2 \left| 2 \frac{\vec{\rho}_2^+}{R_T} - \frac{\vec{\rho}_3}{L} \right|^2 \right/ \underbrace{\left( \frac{1}{\rho_T^2} + \frac{1}{2a_T^2} \right)}_{\approx \rho_T^2} \right\}. \end{aligned}$$

Since  $\rho_T \ll a_T$ , we will employ the indicated approximations.

Completing the square in the magnitude-squared term in the last line and taking the integral with respect to  $\vec{\rho}_3$  results in:

$$\begin{aligned} \langle P(t) \rangle &= \frac{P_T \rho_T^2}{4\pi^2 a_L^2} \int d\vec{\rho}_2^+ \rho(\vec{\rho}_2^+, t_n) s\left(t - t_n - L/c - 2 \left[ R_T - \sqrt{R_T^2 - |\vec{\rho}_2^+|^2} \right] / c\right) \\ &\exp \left\{ -\left( \frac{2}{a_T^2} + \frac{k^2 \rho_T^2}{R_T^2} \right) |\vec{\rho}_2^+|^2 \right\} \underbrace{\frac{2\pi}{2 \left( \frac{1}{a_R^2} + \frac{k^2 \rho_T^2}{4L^2} \right)}}_{\approx \pi a_R^2} \exp \left\{ \underbrace{\frac{\left( \frac{k^2 \rho_T^2}{2R_T^2} \right)^2 \frac{|\vec{\rho}_2^+|^2}{L^2}}{\frac{1}{a_R^2} + \frac{k^2 \rho_T^2}{4L^2}}}_{\approx 1} \right\}. \end{aligned}$$

Noting that  $|\vec{\rho}_2^+| \ll L$  over the support for 1-10 meter targets allows us to drop the last exponential factor, which results in the following expression for the return power:

$$\begin{aligned} \langle P(t) \rangle &= \frac{P_T \rho_T^2}{4\pi a_L^2} \frac{k^2}{L^2} a_R^2 \int d\vec{\rho}_2^+ \rho(\vec{\rho}_2^+, t_n) \exp \left\{ -\left( \frac{2}{a_T^2} + \frac{\rho_T^2 k^2}{R_T^2} \right) |\vec{\rho}_2^+|^2 \right\} \\ &s\left(t - t_n - L/c - 2 \left[ R_T - \sqrt{R_T^2 - |\vec{\rho}_2^+|^2} \right] / c\right). \end{aligned} \quad (\text{B.3})$$

## B.2 RTI Second Moment Projection Derivations

In this section we will calculate the RTI projection covariance assuming a low-contrast target reflectivity model. The following subsection details the calculation of the

covariance between any two points along the projection taken at time  $t_n$  for a radar lying in the target deep far-field and satisfying a super-range resolution condition by transmitting a sufficiently short Gaussian profiled transmission pulse  $s(t)$ . In deriving this result, this section builds the analytical frame work for demonstrating negligible inter-projection correlation for a typical RTI imaging scenario. The projection covariance will then be used in the second subsection to derive the filtered projection variance under identical assumptions.

### B.2.1 Projection Covariance

As rendered in equation (4.8), the photodetector current covariance  $K_{ii}(t, u)$  is the sum of shot-noise, speckle and thermal noise components. Of these three, the speckle contribution will be the most complicated calculation because the result will depend upon the joint return statistics for the two surface regions illuminated at times  $t - L/c$  and  $u - L/c$ , respectively. However, once this solution is in hand, the thermal and shot-noise contributions easily follow. Therefore, we begin by computing the underlying return power covariance in preparation for final specification of the speckle and shot-noise terms.

We define the power covariance at the time instants  $t$  and  $u$  to be  $K_{PP}(t, u) = \langle [P(t) - \langle P(t) \rangle] \cdot [P(u) - \langle P(u) \rangle] \rangle$ . Expanding this definition, we have

$$\begin{aligned}
K_{PP}(t, u) &= \left\langle \int_{-\infty}^{+\infty} d\vec{\rho}_3 e^{-|\vec{\rho}_3|^2/a_R^2} \mathbf{U}_\tau(\vec{\rho}_3, t) \mathbf{U}_\tau^*(\vec{\rho}_3, t) \times \right. \\
&\quad \left. \int_{-\infty}^{+\infty} d\vec{\rho}_3 e^{-|\vec{\rho}_3|^2/a_R^2} \mathbf{U}_\tau(\vec{\rho}_3, u) \mathbf{U}_\tau^*(\vec{\rho}_3, u) \right\rangle - \langle P(t) \rangle \langle P(u) \rangle \\
&= \int_{-\infty}^{+\infty} d\vec{\rho}_3 \int_{-\infty}^{+\infty} d\vec{\rho}_3' e^{-(|\vec{\rho}_3|^2 + |\vec{\rho}_3'|^2)/a_R^2} \left\langle \mathbf{U}_\tau(\vec{\rho}_3, t) \mathbf{U}_\tau^*(\vec{\rho}_3, t) \mathbf{U}_\tau(\vec{\rho}_3', u) \mathbf{U}_\tau^*(\vec{\rho}_3', u) \right\rangle \\
&\quad - \langle P(t) \rangle \langle P(u) \rangle \tag{B.4} \\
&= \int_{-\infty}^{+\infty} d\vec{\rho}_3 \int_{-\infty}^{+\infty} d\vec{\rho}_3' e^{-(|\vec{\rho}_3|^2 + |\vec{\rho}_3'|^2)/a_R^2}
\end{aligned}$$

$$\begin{aligned}
& \left[ \left\langle \mathbf{U}_r(\vec{\rho}_3, t) \mathbf{U}_r^*(\vec{\rho}_3', u) \right\rangle \left\langle \mathbf{U}_r^*(\vec{\rho}_3, t) \mathbf{U}_r(\vec{\rho}_3', u) \right\rangle \right. \\
& + \underbrace{\left\langle \mathbf{U}_r(\vec{\rho}_3, t) \mathbf{U}_r^*(\vec{\rho}_3, t) \right\rangle}_{\text{Becomes } \langle P(t) \rangle} \underbrace{\left\langle \mathbf{U}_r^*(\vec{\rho}_3', u) \mathbf{U}_r(\vec{\rho}_3', u) \right\rangle}_{\text{Becomes } \langle P(u) \rangle} \\
& + \underbrace{\left\langle \mathbf{U}_r(\vec{\rho}_3, t) \mathbf{U}_r(\vec{\rho}_3', u) \right\rangle}_{=0} \underbrace{\left\langle \mathbf{U}_r^*(\vec{\rho}_3, t) \mathbf{U}_r^*(\vec{\rho}_3', u) \right\rangle}_{=0} \left. \right] \\
& - \langle P(t) \rangle \langle P(u) \rangle \tag{B.5}
\end{aligned}$$

$$= \int_{-\infty}^{+\infty} d\vec{\rho}_3 \int_{-\infty}^{+\infty} d\vec{\rho}_3' e^{-(|\vec{\rho}_3|^2 + |\vec{\rho}_3'|^2)/a_R^2} \left| \left\langle \mathbf{U}_r(\vec{\rho}_3, t) \mathbf{U}_r^*(\vec{\rho}_3', u) \right\rangle \right|^2 \tag{B.6}$$

where complex Gaussian moment factoring was applied to (B.4) producing the expansion of (B.5). Applying the arguments and procedures of the previous section to propagate the surface roughness covariance to the receiver aperture optical field allows us to write the expectation within the magnitude-square as

$$\begin{aligned}
\left\langle \mathbf{U}_r(\vec{\rho}_3, t) \mathbf{U}_r^*(\vec{\rho}_3', u) \right\rangle &= \frac{k^2}{4\pi^2 L^2} \frac{P_T}{\pi a_L^2} \exp \left\{ -\frac{1}{2} \frac{jk}{L} (|\vec{\rho}_3|^2 - |\vec{\rho}_3'|^2) \right\} \\
& \int d\vec{\rho}_2 \int d\vec{\rho}_2' \sqrt{\rho(\vec{\rho}_2, t_n)} \sqrt{\rho(\vec{\rho}_2', t_n)} \exp \left\{ -\frac{|\vec{\rho}_2 - \vec{\rho}_2'|^2}{\rho_T^2} \right\} \\
& s^{1/2} \left( t - t_n - L/c - 2 \left[ R_T - \sqrt{R_T^2 - |\vec{\rho}_2|^2} \right] / c \right) \\
& s^{1/2} \left( u - t_n - L/c - 2 \left[ R_T - \sqrt{R_T^2 - |\vec{\rho}_2'|^2} \right] / c \right) \\
& \exp \left\{ -|\vec{\rho}_2|^2 \underbrace{\left( \frac{1}{2a_L^2} + \frac{1}{a_T^2} \right)}_{\approx 1/a_T^2} \right\} \exp \left\{ -|\vec{\rho}_2'|^2 \underbrace{\left( \frac{1}{2a_L^2} + \frac{1}{a_T^2} \right)}_{\approx 1/a_T^2} \right\} \\
& \exp \left\{ jk(|\vec{\rho}_2|^2 - |\vec{\rho}_2'|^2) \underbrace{\left( \frac{1}{2L} + \frac{1}{R_T} \right)}_{\approx 1/R_T} \right\} \exp \{ -jk(\vec{\rho}_3 \cdot \vec{\rho}_2 - \vec{\rho}_3' \cdot \vec{\rho}_2') / L \}.
\end{aligned}$$



Often, the short-duration mode-locked or Q-switched pulse lasers produce transmission pulses which have a time-intensity profile that is bell shaped. Therefore, we will assume that the pulse modulation can be represented by a Gaussian form,  $s(t) = e^{-\frac{1}{2}t^2/T^2}$ , where  $T$  is the nominal pulse width.

Applying this definition to the above correlation expression and converting both the primed and unprimed  $\vec{\rho}_2$  and  $\vec{\rho}_3$  reference vectors to sum and difference coordinate systems according to our previous pattern, we now write

$$\begin{aligned} \left\langle \mathbf{U}_r(\vec{\rho}_3^+ + \frac{1}{2}\vec{\rho}_3^-, t) \mathbf{U}_r^*(\vec{\rho}_3^+ - \frac{1}{2}\vec{\rho}_3^-, u) \right\rangle = & \\ & \frac{k^2}{4\pi^2 L^2} \frac{P_T \rho_T^2}{\pi a_L^2} \exp \left\{ -\frac{jk}{L} \vec{\rho}_3^+ \cdot \vec{\rho}_3^- \right\} \exp \left\{ -\frac{1}{8}(t-u)^2/T^2 \right\} \\ & \int d\vec{\rho}_2^+ \rho(\vec{\rho}_2^+, t_n) \exp \left\{ -\frac{jk}{2L} \vec{\rho}_3^- \cdot \vec{\rho}_2^+ \right\} \exp \left\{ -\left( \frac{2}{a_T^2} + \frac{\rho_T^2 k^2}{R_T^2} \right) |\vec{\rho}_2^+|^2 \right\} \\ & \exp \left\{ -\frac{1}{2T^2} \left( \frac{t+u}{2} - t_n - L/c - 2 \left[ R_T - \sqrt{R_T^2 - |\vec{\rho}_2^+|^2} \right] / c \right)^2 \right\}. \quad (\text{B.7}) \end{aligned}$$

"Doughnut-shaped" Pulse Overlap Function

Again, we have assumed that the spatial distribution of both the surface reflectivity and the pulse illumination varies slowly across the very small surface correlation region. Therefore, in evaluating the integral with respect to  $\vec{\rho}_2^-$ , we have taken the following approximations:

$$\sqrt{\rho(\vec{\rho}_2^+ + \frac{1}{2}\vec{\rho}_2^-, t_n)} \sqrt{\rho(\vec{\rho}_2^+ - \frac{1}{2}\vec{\rho}_2^-, t_n)} \approx \rho(\vec{\rho}_2^+, t_n)$$

and

$$\begin{aligned} s^{1/2} \left( t - t_n - L/c - 2 \left[ R_T - \sqrt{R_T^2 - |\vec{\rho}_2^+ + \frac{1}{2}\vec{\rho}_2^-|^2} \right] / c \right) \times \\ s^{1/2} \left( u - t_n - L/c - 2 \left[ R_T - \sqrt{R_T^2 - |\vec{\rho}_2^+ - \frac{1}{2}\vec{\rho}_2^-|^2} \right] / c \right) \\ \approx \exp \left\{ -\frac{1}{8}(t-u)^2/T^2 \right\} \times \end{aligned}$$

$$\exp \left\{ -\frac{1}{2T^2} \left( \frac{t+u}{2} - t_n - L/c - 2 \left[ R_T - \sqrt{R_T^2 - |\vec{\rho}_2^+|^2} \right] / c \right)^2 \right\}$$

where the last approximation involving the Gaussian pulse modulation  $s(t) = e^{-\frac{1}{2}t^2/T^2}$  fixes the retarded time over the surface correlation region as a function of the sum coordinate  $\vec{\rho}_2^+$ .

The above expectation (B.7) is a function of both the sum and difference of  $t$  and  $u$ . The reader will recognize that this expression is formulated as a rather complicated two-dimensional spatial Fourier transform with respect to the variable  $\vec{\rho}_2^+$ . The transform is operating on the target reflectivity projection taken at time  $t_n$  and weighted by both the aspect angle-surface roughness limb effect and a "doughnut-shaped" projection of the  $t + u$  time dependent overlap between the two illumination patterns on the target surface corresponding to the two pulse positions at times  $t$  and  $u$ , respectively.

In general, this Fourier transform will not have a closed-form solution. However, a close approximation can be developed for a laser radar sited in the target's deep far-field optical regime. In this case, we restrict the receiver aperture to a range of sizes such that the complex spatial frequency factor under the Fourier transform integral is nearly unity over the target support. This will be accomplished if we choose  $a_R \ll 2\lambda L / \sqrt{\frac{2}{a_T^2} + \frac{\rho_T^2 k^2}{R_T^2}}$ . For the sake of simplicity, we will also assume a low-contrast surface reflectivity model for  $\rho$  and disregard the limb darkening effects of aspect angle-surface roughness. Therefore, the Fourier transform simply becomes the area under the  $\mathcal{T}$ -plane projection of the aforementioned doughnut-shaped illumination overlap function.

Transforming  $\vec{\rho}_2^+$  to a polar coordinate formulation and restricting the radial component to lie within the projected radius of the target,  $R_T$ , gives an overlap

formulation which can be rewritten in terms of the target centered range variable. Integrating with respect to this range variable, the area under the overlap function projection can be shown to be:

$$\begin{aligned}
\text{Area} = & \sqrt{8\pi^3} \frac{1}{2} cT \left( R_T - \frac{1}{2} c \frac{t+u}{2} + \frac{1}{2} ct_n + L/2 \right) \times \\
& \left[ \Phi \left\{ \left( \frac{1}{2} c \frac{t+u}{2} - \frac{1}{2} ct_n - L/2 \right) / \frac{1}{2} cT \right\} - \right. \\
& \quad \left. \Phi \left\{ \left( \frac{1}{2} c \frac{t+u}{2} - \frac{1}{2} ct_n - L/2 - R_T \right) / \frac{1}{2} cT \right\} \right] + \\
& 2\pi \left( \frac{1}{2} cT \right)^2 \left[ \exp \left\{ -\frac{1}{2} \left( \frac{1}{2} c \frac{t+u}{2} - \frac{1}{2} ct_n - L/2 - R_T \right)^2 / \left( \frac{1}{2} cT \right)^2 \right\} - \right. \\
& \quad \left. \exp \left\{ -\frac{1}{2} \left( \frac{1}{2} c \frac{t+u}{2} - \frac{1}{2} ct_n - L/2 \right)^2 / \left( \frac{1}{2} cT \right)^2 \right\} \right] \quad (\text{B.8})
\end{aligned}$$

where the error function,  $\Phi(x)$ , is defined as

$$\Phi(x) \equiv \frac{1}{\sqrt{\pi}} \int_0^x dt \exp\{-t^2\}.$$

Under super-range resolution conditions,  $c/B_1 \ll R_T$ , the term on the last two lines of (B.8) becomes negligible. This action gives an intuitively pleasing result, since the area under the overlap function is now directly proportional to the equivalent sum time range displacement from the target center times the difference between of the two  $\Phi$  functions, which constitutes a range gate from  $L$  to  $L + R_T$  meters from the laser radar. Therefore, we only have significant returns from the illuminated face of the target.

Incorporating this approximation into the expectation of (B.7), we find that

$$\begin{aligned}
\left\langle \mathbf{U}_r(\vec{\rho}_3^+ + \frac{1}{2}\vec{\rho}_3^-, t) \mathbf{U}_r^*(\vec{\rho}_3^+ - \frac{1}{2}\vec{\rho}_3^-, u) \right\rangle \approx \\
\frac{k^2}{4\pi^2 L^2} \frac{P_T \rho_T^2}{\pi a_L^2} \rho \exp \left\{ -\frac{jk}{L} \vec{\rho}_3^+ \cdot \vec{\rho}_3^- \right\} \\
\sqrt{8\pi^3} \frac{1}{2} cT \left( R_T - \frac{1}{2} c \frac{t+u}{2} + \frac{1}{2} ct_n + L/2 \right) \exp \left\{ -\frac{1}{8}(t-u)^2/T^2 \right\} \times
\end{aligned}$$

$$\left[ \Phi \left\{ \left( \frac{1}{2}c \frac{t+u}{2} - \frac{1}{2}ct_n - L/2 \right) / \frac{1}{2}cT \right\} - \Phi \left\{ \left( \frac{1}{2}c \frac{t+u}{2} - \frac{1}{2}ct_n - L/2 - R_T \right) / \frac{1}{2}cT \right\} \right]$$

where the factor on the last three lines is equal to the projected overlap area.

Taking the magnitude-squared of this result and integrating over the aperture within a  $\vec{\rho}_3$  sum and difference coordinate formulation gives the final expression for the received power covariance

$$\begin{aligned} K_{PP}(t, u) = & \frac{1}{2\pi} \frac{k^4 a_R^4}{L^4} \frac{P_T^2 \rho_T^4}{a_L^4} \rho^2 \left( \frac{1}{2}cT \right)^2 \exp \left\{ -\frac{1}{4}(t-u)^2 / T^2 \right\} \times \\ & \left( R_T - \frac{1}{2}c \frac{t+u}{2} + \frac{1}{2}ct_n + L/2 \right)^2 \times \\ & \left[ \Phi \left\{ \left( \frac{1}{2}c \frac{t+u}{2} - \frac{1}{2}ct_n - L/2 \right) / \frac{1}{2}cT \right\} - \right. \\ & \left. \Phi \left\{ \left( \frac{1}{2}c \frac{t+u}{2} - \frac{1}{2}ct_n - L/2 - R_T \right) / \frac{1}{2}cT \right\} \right]^2. \quad (\text{B.9}) \end{aligned}$$

We will now take advantage of the fact that this result is written in sum and difference time coordinates.

As stated in §4.1.3, the quantity

$$\left\{ \frac{eG\eta}{h\nu} \right\}^2 \int d\tau \int d\mu h(t-\tau) h(u-\mu) K_{PP}(\tau, \mu) \equiv K_{ii}^{\text{Speckle}}(t, u) \quad (\text{B.10})$$

is the photodetector current covariance component attributable to received power fluctuations, where  $h(t)$  is the detector impulse response. In this analysis, the impulse response will be modelled by the low-pass Gaussian frequency response  $h(t) \xleftrightarrow{\mathcal{F}} e^{-\frac{1}{2}f^2/B^2}$  where  $B$  is the nominal detector bandwidth.

Before calculating this covariance component, the above double-integral will be rewritten in a power spectrum formulation which contrasts the relative contributions between the sum and difference time-dependent factors. Switching to the sum and

difference time coordinate systems:

$$\begin{aligned}\alpha_+ &= \frac{1}{2}(t + u) \\ \alpha_- &= t - u\end{aligned}$$

and

$$\begin{aligned}\beta_+ &= \frac{1}{2}(\tau + \mu) \\ \beta_- &= \tau - \mu\end{aligned}$$

the double-integral becomes

$$\begin{aligned}K_{ii}^{\text{Speckle}}(\alpha_+ + \frac{1}{2}\alpha_-, \alpha_+ - \frac{1}{2}\alpha_-) &= \left\{ \frac{eG\eta}{h\nu} \right\}^2 \int d\beta_+ \int d\beta_- K_{PP}^{\pm}(\beta_+, \beta_-) \\ &\quad h(\alpha_+ - \beta_+ + \frac{1}{2}(\alpha_- - \beta_-)) h^*(\alpha_+ - \beta_+ - \frac{1}{2}(\alpha_- - \beta_-)) \\ &= \left\{ \frac{eG\eta}{h\nu} \right\}^2 \int d\beta_+ \int d\beta_- K_{PP}^{\pm}(\beta_+, \beta_-) \int df_1 H(f_1) \int df_2 H^*(f_2) \\ &\quad \exp \left\{ +2\pi j \left[ (\alpha_+ - \beta_+)(f_1 - f_2) + \frac{1}{2}(f_1 + f_2)(\alpha_- - \beta_-) \right] \right\}\end{aligned}$$

where  $K_{PP}^{\pm}$  is the sum and difference formulation for the received power covariance and  $H(f) \xleftrightarrow{\mathcal{F}} h(t)$ .

Using the fact from equation (B.9) that  $K_{PP}^{\pm}(\beta_+, \beta_-)$  is separable in the  $(\beta_+, \beta_-)$  sum and difference time coordinates, we now write:

$$K_{PP}^{\pm}(\beta_+, \beta_-) = \text{Var}_P(\beta_+) \cdot k_{PP}(\beta_-)$$

where the corresponding Fourier transform pairs are defined as follows:

$$\begin{aligned}\text{Var}_P(\beta_+) &\xleftrightarrow{\mathcal{F}} \mathcal{V}_P(f) \\ k_{PP}(\beta_-) &\xleftrightarrow{\mathcal{F}} \mathcal{S}_{PP}(f).\end{aligned}$$

Exchanging the time- and frequency-domain integrals, we have:

$$\begin{aligned}
& K_{ii}^{\text{Speckle}}(\alpha_+ + \frac{1}{2}\alpha_-, \alpha_+ - \frac{1}{2}\alpha_-) \\
&= \left\{ \frac{eG\eta}{h\nu} \right\}^2 \int df_1 H(f_1) \int df_2 H^*(f_2) \int d\beta_+ \text{Var}_P(\beta_+) e^{+2\pi j(\alpha_+ - \beta_+)(f_1 - f_2)} \\
&\quad \int d\beta_- k_{PP}(\beta_-) e^{+2\pi j \left[ \frac{1}{2}(f_1 + f_2) \right] (\alpha_- - \beta_-)} \\
&= \left\{ \frac{eG\eta}{h\nu} \right\}^2 \int df_1 H(f_1) \int df_2 H^*(f_2) \mathcal{V}_P(f_1 - f_2) e^{2\pi j \alpha_+ (f_1 - f_2)} \\
&\quad \mathcal{S}_{PP} \left( \frac{1}{2}(f_1 + f_2) \right) e^{2\pi j \alpha_- (f_1 + f_2)/2}.
\end{aligned}$$

Switching to the sum- and difference coordinate system in the frequency domain:

$$\begin{aligned}
f_+ &= \frac{1}{2}(f_1 + f_2) \\
f_- &= f_1 - f_2
\end{aligned}$$

we may finally write our desired formulation for the covariance double-integral in the resulting rotated frequency-plane coordinate system:

$$\begin{aligned}
& K_{ii}^{\text{Speckle}}(\alpha_+ + \frac{1}{2}\alpha_-, \alpha_+ - \frac{1}{2}\alpha_-) \\
&= \left\{ \frac{eG\eta}{h\nu} \right\}^2 \int df_+ \int df_- H(f_+ + \frac{1}{2}f_-) H^*(f_+ - \frac{1}{2}f_-) \\
&\quad \mathcal{V}_P(f_-) e^{2\pi j f_- \alpha_+} \mathcal{S}_{PP}(f_+) e^{2\pi j f_+ \alpha_-} \tag{B.11} \\
&= \left\{ \frac{eG\eta}{h\nu} \right\}^2 \int df_+ \mathcal{S}_{PP}(f_+) e^{-f_+^2/B^2} e^{2\pi j f_+ \alpha_-} \int df_- \mathcal{V}_P(f_-) e^{-f_-^2/4B^2} e^{2\pi j f_- \alpha_+}
\end{aligned}$$

where, in the last line, we have substituted for the photodetector frequency response.

If we retain the assumption that the illumination pulse width  $T$  is sufficiently small to provide meaningful resolution, every factor in the above expression has a relatively large bandwidth except for  $\mathcal{V}_P(f_-)$ . Assuming that  $e^{-f_-^2/4B^2}$  is nearly unity over the bandwidth of  $\mathcal{V}_P(f_-)$  reduces the last integral to  $\text{Var}_P(\alpha_+)$ . Taking the remaining integral with respect to  $df_+$  and converting back to the original  $t$  and  $u$

time coordinates, we then have:

$$\begin{aligned}
 & K_{ii}^{\text{Speckle}}(t, u) \\
 &= \left\{ \frac{eG\eta}{h\nu} \right\}^2 \frac{k^4 a_R^4}{L^4} \frac{P_T^2 \rho_T^4}{a_L^4} \rho^2 \left( \frac{1}{2}cT \right)^2 \\
 & TB_1 \exp \left\{ -(t-u)^2 / \frac{1}{\pi^2 B_1^2} \right\} \left( R_T - \frac{1}{2}c \frac{t+u}{2} + \frac{1}{2}ct_n + L/2 \right)^2 \times \\
 & \left[ \Phi \left\{ \left( \frac{1}{2}c \frac{t+u}{2} - \frac{1}{2}ct_n - L/2 \right) / \frac{1}{2}cT \right\} - \right. \\
 & \quad \left. \Phi \left\{ \left( \frac{1}{2}c \frac{t+u}{2} - \frac{1}{2}ct_n - L/2 - R_T \right) / \frac{1}{2}cT \right\} \right]^2 \quad (\text{B.12})
 \end{aligned}$$

where we have defined the system bandwidth to be

$$B_1 \equiv \sqrt{\frac{1}{4\pi^2 T^2 + \frac{1}{B^2}}} \quad (\text{B.13})$$

A similar analysis results in the following quantities for the thermal and shot-noise contributions:

$$K_{ii}^{\text{Thermal}}(t, u) = \sqrt{\pi} B \frac{2k_B T_L}{R_L} \exp \left\{ -(t-u)^2 / \frac{1}{\pi^2 B^2} \right\} \quad (\text{B.14})$$

and

$$\begin{aligned}
 K_{ii}^{\text{SN}}(t, u) &= \frac{1}{4\sqrt{\pi}} \frac{e^2 G^{2+x} \eta}{h\nu} \frac{k^2 a_R^2}{L^2} \frac{P_T \rho_T^2}{a_L^2} \rho B \left( \frac{1}{2}cT \right) \\
 & \exp \left\{ -(t-u)^2 / \frac{1}{\pi^2 B^2} \right\} \left( R_T - \frac{1}{2}c \frac{t+u}{2} + \frac{1}{2}ct_n + L/2 \right) \times \\
 & \left[ \Phi \left\{ \left( \frac{1}{2}c \frac{t+u}{2} - \frac{1}{2}ct_n - L/2 \right) / \frac{1}{2}cT \right\} - \right. \\
 & \quad \left. \Phi \left\{ \left( \frac{1}{2}c \frac{t+u}{2} - \frac{1}{2}ct_n - L/2 - R_T \right) / \frac{1}{2}cT \right\} \right]. \quad (\text{B.15})
 \end{aligned}$$

By rescaling the time axis to convert to range *measured from the target center* and summing the shot-noise, speckle and thermal noise components in that order,

we have the result cited in (4.16),

$$\begin{aligned}
K_{pp}(r_1, r_2) \approx & \frac{1}{4\sqrt{\pi}} \frac{e^2 G^{2+\alpha} \eta}{h\nu} \frac{k^2 a_R^2}{L^2} \frac{P_T \rho_T^2}{a_L^2} \rho B \left(\frac{1}{2}cT\right) \times \\
& \left(-\frac{r_1 + r_2}{2}\right) \exp\left\{-\frac{(r_1 - r_2)^2}{4\pi^2 B^2} \frac{c^2}{4\pi^2 B^2}\right\} \times \\
& \left[ \Phi\left\{\left(\frac{r_1 + r_2}{2} + R_T\right) / \frac{1}{2}cT\right\} - \Phi\left\{\left(\frac{r_1 + r_2}{2}\right) / \frac{1}{2}cT\right\} \right] \\
+ & \left(\frac{eG\eta}{h\nu_o}\right)^2 \left(\frac{ka_r}{L}\right)^4 \left(\frac{P_T \rho_T^2}{a_L^2}\right)^2 \rho^2 \left(\frac{1}{2}cT\right)^2 T B_1 \times \\
& \left(-\frac{1}{2}(r_1 + r_2)\right)^2 \exp\left\{-\frac{(r_1 - r_2)^2}{4\pi^2 B_1^2} \frac{c^2}{4\pi^2 B_1^2}\right\} \times \\
& \left[ \Phi\left\{\left(\frac{1}{2}(r_1 + r_2) + R_T\right) / \frac{1}{2}cT\right\} - \Phi\left\{\left(\frac{1}{2}(r_1 + r_2)\right) / \frac{1}{2}cT\right\} \right]^2 \\
+ & \sqrt{\pi} B \frac{2k_B T_L}{R_L} \exp\left\{-\frac{(r_1 - r_2)^2}{4\pi^2 B^2} \frac{c^2}{4\pi^2 B^2}\right\} \tag{B.16}
\end{aligned}$$

where positive values of  $r_1$  and  $r_2$  fall on the far side of the target. Note that this result is separable into sum and difference range coordinates.

To demonstrate that inter-projection correlation is negligible, we will show that the speckle coherence time is much shorter than the inter-pulse period in a typical RTI imaging scenario. The speckle coherence time will be estimated by dividing the speckle coherence length by the rate at which speckle lobes travel over the receiver aperture.

We begin by defining the speckle covariance between the two position vectors  $\vec{\rho}_3$  and  $\vec{\rho}_3'$  spanning the receiver plane as  $K_{II}(\vec{\rho}_3, \vec{\rho}_3', t) = \left\langle [I(\vec{\rho}_3, t) - \langle I(\vec{\rho}_3, t) \rangle] \cdot [I(\vec{\rho}_3', t) - \langle I(\vec{\rho}_3', t) \rangle] \right\rangle$  where the received field intensity  $I(\vec{\rho}_3, t)$  is  $\mathbf{U}_r(\vec{\rho}_3, t) \mathbf{U}_r^*(\vec{\rho}_3, t)$ . Expanding this definition and applying complex Gaussian moment factoring, we have  $K_{II}(\vec{\rho}_3, \vec{\rho}_3', t) = \left| \left\langle \mathbf{U}_r(\vec{\rho}_3, t) \mathbf{U}_r^*(\vec{\rho}_3', t) \right\rangle \right|^2$ .

Equation (B.7) implies that the speckle lobe spatial structure will depend upon both the surface reflectivity and roughness distributions as well as the shape of the



illumination pulse striking the target at time  $t_n$ . Since only a rough, order of magnitude estimate of the coherence length is needed to validate our inter-projection decorrelation assertion, for convenience sake, let us assume a constant target reflectivity of  $\rho$  and constant spotlight mode illumination of the target (i.e.,  $s(t) = 1$ ). Under these conditions, (B.7) reduces to

$$\begin{aligned}
 & \left\langle \mathbf{U}_r(\vec{\rho}_3^+ + \frac{1}{2}\vec{\rho}_3^-) \mathbf{U}_r^*(\vec{\rho}_3^+ - \frac{1}{2}\vec{\rho}_3^-) \right\rangle \\
 &= \frac{k^2}{4\pi^2 L^2} \frac{P_T \rho_T^2}{\pi a_L^2} \rho \exp \left\{ -\frac{jk}{L} \vec{\rho}_3^+ \cdot \vec{\rho}_3^- \right\} \\
 & \quad \int d\vec{\rho}_2 \exp \left\{ -\frac{jk}{2L} \vec{\rho}_3^- \cdot \vec{\rho}_2^+ \right\} \exp \left\{ -\left( \frac{2}{a_T^2} + \frac{\rho_T^2 k^2}{R_T^2} \right) |\vec{\rho}_2^+|^2 \right\} \\
 &= \rho \frac{k^2}{2\pi L^2} \frac{P_T \rho_T^2}{\pi a_L^2} \left( \frac{2}{a_T^2} + \frac{\rho_T^2 k^2}{R_T^2} \right)^{-1} \exp \left\{ -\frac{jk}{L} \vec{\rho}_3^+ \cdot \vec{\rho}_3^- \right\} \\
 & \quad \exp \left\{ -|\vec{\rho}_3^-|^2 / \frac{4\lambda^2 L^2}{\pi^2} \left( \frac{2}{a_T^2} + \frac{\rho_T^2 k^2}{R_T^2} \right) \right\}.
 \end{aligned}$$

during the time period when the laser illumination echo reaches the receiver.

Taking the magnitude-square and returning to the original  $\vec{\rho}_3$  and  $\vec{\rho}_3'$  coordinates results in the following time independent speckle spatial covariance:

$$\begin{aligned}
 K_{II}(\vec{\rho}_3, \vec{\rho}_3') &= \rho^2 \frac{k^4}{4\pi^2 L^4} \frac{P_T^2 \rho_T^4}{\pi^2 a_L^4} \left( \frac{2}{a_T^2} + \frac{\rho_T^2 k^2}{R_T^2} \right)^{-2} \\
 & \quad \exp \left\{ -|\vec{\rho}_3 - \vec{\rho}_3'|^2 / \frac{2\lambda^2 L^2}{\pi^2} \left( \frac{2}{a_T^2} + \frac{\rho_T^2 k^2}{R_T^2} \right) \right\}.
 \end{aligned}$$

If we define the speckle decorrelation length to be  $\rho_I \equiv |\Delta\vec{\rho}|$  such that

$$\frac{K_{II}(\vec{\rho}_3 + \frac{1}{2}\Delta\vec{\rho}, \vec{\rho}_3 - \frac{1}{2}\Delta\vec{\rho})}{K_{II}(\vec{\rho}_3, \vec{\rho}_3)} = e^{-1},$$

then we compute the following length:

$$\rho_I = \frac{\sqrt{2}\lambda L}{\pi} \sqrt{\frac{2}{a_T^2} + \frac{\rho_T^2 k^2}{R_T^2}}.$$

The law of reflection implies that the reflected return speckle pattern reaching the laser radar passes by the receiver aperture at an angular rate twice the target's rotation rate of  $\Omega$ . Therefore, speckle lobes transverse the receiver at a velocity of  $2L\Omega$ . Thus, the speckle coherence time,  $\tau_{\text{coh}}$ , is found to be:

$$\tau_{\text{coh}} = \frac{\lambda}{\sqrt{2\pi}\Omega} \sqrt{\frac{2}{a_T^2} + \frac{\rho_T^2 k^2}{R_T^2}} \approx \frac{\sqrt{2}\rho_T}{R_T\Omega} \quad (\text{B.17})$$

where the final approximation comes from assuming  $a_T = R_T$  and  $\rho_T \approx \lambda$ .

Projections will be statistically independent if the inter-projection time,  $2\pi/N\Omega$ , is significantly larger than  $\tau_{\text{coh}}$ . This condition is satisfied if

$$N \ll \frac{\sqrt{2\pi} R_T}{\rho_T}. \quad (\text{B.18})$$

To put this result into perspective, consider a one meter radius spherical satellite orbiting within the laser radar's far-field. In this case, assuming the radar uses a CO<sub>2</sub> laser at a wavelength of 10.6  $\mu\text{m}$  with a corresponding surface roughness correlation length of  $\rho_T = \lambda$  at the target, the right-hand-side of the above relation becomes 419,000. Ignoring the case of an extremely large aperture which collects contributions from many speckle lobes, we conclude that the remaining RTI imaging scenarios will comfortably maintain inter-projection statistical independence over the course of the target revolution.

## B.2.2 Filtered RTI Projection Variance

In this section we will compute the filtered RTI projection variance used to establish the filtered backprojection reconstruction SNR result. We begin by formulating the filtering operation in a standard LTI systems description:

$$p(r) \longrightarrow \boxed{\begin{array}{c} \text{LTI System} \\ h(r) \end{array}} \longrightarrow p'(r)$$

where each projection is filtered by  $h(r) \xleftrightarrow{\mathcal{F}} H(f) = |f|$  to produce a new projection  $p'(r)$  which is then backprojected establishing the inverse Radon transform operation. Since the filtering operation is independent from projection to projection, we will still assume that each  $p'(r)$  is statistically independent of all other filtered projections.

Our approach will build upon the projection covariance result derived in the previous subsection. Again, we will concentrate on the speckle contribution by formulating this sum and difference range separable covariance component in a frequency-domain description which easily allows us to calculate an approximation under super resolution conditions. Then the independent filtered thermal and shot-noise components will be added to complete the filtered projection variance calculation.

The variance reformulation begins with the fact that  $\text{var}_{p'}(r) = K_{p'p'}(r, r)$  and

$$K_{p'p'}(r_1, r_2) = \int dr'_1 \int dr'_2 K_{pp}(r'_1, r'_2) h(r_1 - r'_1) h^*(r_2 - r'_2).$$

For the speckle component, we apply the same covariance transformation procedure as outlined from equation (B.10) to equation (B.11), which produces:

$$\begin{aligned} K_{p'p'}^{\text{Speckle}}(r_+ + \frac{1}{2}r_-, r_+ - \frac{1}{2}r_-) &= \int df_+ \int df_- H(f_+ + \frac{1}{2}f_-) H^*(f_+ - \frac{1}{2}f_-) \\ &\quad \mathcal{V}_p(f_-) e^{2\pi jr_+ f_-} \mathcal{S}_{pp}(f_+) e^{2\pi j f_+ r_-}. \end{aligned}$$

where  $(r_+, r_-)$  and  $(f_+, f_-)$  are the sum and difference range and spatial range frequencies, respectively, defined in our previous pattern, and

$$\begin{aligned} \text{Var}_p(r_+) &\xleftrightarrow{\mathcal{F}} \mathcal{V}_p(f) \\ k(r_-) &\xleftrightarrow{\mathcal{F}} \mathcal{S}_{pp}(f) \end{aligned}$$

are the Fourier transform pairs of the sum and difference range-dependent factors in the separable speckle projection covariance. Thus, the filtered projection variance at

the point  $r$  is

$$\begin{aligned} \text{var}_{p'p'}^{\text{Speckle}}(r) &= K_{p'p'}^{\text{Speckle}}\left(r + \frac{1}{2} \cdot 0, r - \frac{1}{2} \cdot 0\right) \\ &= \int df_+ \int df_- H\left(f_+ + \frac{1}{2}f_-\right) H^*\left(f_+ - \frac{1}{2}f_-\right) \mathcal{V}_p(f_-) e^{2\pi j r f_-} \mathcal{S}_{pp}(f_+) \quad (\text{B.19}) \end{aligned}$$

Now applying the above reformulation result to our specific case of the inverse Radon transform, we have  $H(f) = |f|$  which gives:

$$\begin{aligned} \text{var}_{p'p'}^{\text{Speckle}}(r) &= \int df_+ \int df_- \left|f_+^2 - \frac{1}{4}f_-^2\right| \mathcal{V}_p(f_-) e^{2\pi j r f_-} \mathcal{S}_{pp}(f_+) \quad (\text{B.20}) \end{aligned}$$

$$\begin{aligned} &= \int_{-\infty}^{+\infty} df_+ \int_{-\infty}^{+\infty} df_- \left(f_+^2 - \frac{1}{4}f_-^2\right) \mathcal{V}_p(f_-) e^{2\pi j r f_-} \mathcal{S}_{pp}(f_+) - \\ &2 \times \underbrace{\int_{-\infty}^{+\infty} df_- \int_{-\frac{1}{2}|f_-|}^{+\frac{1}{2}|f_-|} df_+ \left(f_+^2 - \frac{1}{4}f_-^2\right) \mathcal{V}_p(f_-) e^{2\pi j r f_-} \mathcal{S}_{pp}(f_+)}_{\text{Neglect}}, \quad (\text{B.21}) \end{aligned}$$

with the following specifications taken from (B.16),

$$k_{pp}(r_-) = \exp\left\{-r_-^2 / \frac{c^2}{4\pi^2 B_1^2}\right\}$$

$$\begin{aligned} \text{Var}_p(r_+) &= \left(\frac{eG\eta}{h\nu_o}\right)^2 \left(\frac{ka_r}{L}\right)^4 \left(\frac{P_T \rho_T^2}{a_L^2}\right)^2 \rho^2 \left(\frac{1}{2}cT\right)^2 T B_1 \\ &(-r_+)^2 \left[ \Phi\left\{(r_+ + R_T) / \frac{1}{2}cT\right\} - \Phi\left\{r_+ / \frac{1}{2}cT\right\} \right]^2. \end{aligned}$$

Suppose the laser radar is operating with a pulse width  $T$  chosen to provide useful resolution in the range dimension. In the frequency domain, this assumption means that the function  $\mathcal{V}_p$  is much narrower than the function  $\mathcal{S}_{pp}$ . Therefore, in the  $(f_+, f_-)$  Fourier plane, the function  $\mathcal{V}_p(f_-) \mathcal{S}_{pp}(f_+)$  forms a narrow ridge-like feature running along the  $f_+$ -axis. Since the region of integration for the double-integral on the second line of (B.21) overlaps a small part of the footprint of this "ridge," this contribute to the total will be neglected.

Performing the remaining distribution over the parenthetical term in the first line of (B.21) gives:

$$\begin{aligned} \text{var}_{p'p'}^{\text{Speckle}}(r) = & \int_{-\infty}^{+\infty} df_+ f_+^2 \mathcal{S}_{pp}(f_+) \int_{-\infty}^{+\infty} df_- \mathcal{V}_p(f_-) e^{2\pi j r f_-} \\ & - \int_{-\infty}^{+\infty} df_+ \mathcal{S}_{pp}(f_+) \int_{-\infty}^{+\infty} df_- \frac{1}{4} f_-^2 \mathcal{V}_p(f_-) e^{2\pi j r f_-} . \end{aligned} \quad (\text{B.22})$$

Substituting in the expressions for the separable components and their Fourier transforms and performing the indicated integrations, we discover that the expansion of the second double-integral in equation (B.22) is insignificant under super-resolution conditions.

Therefore, neglecting those terms, and adding the filtered thermal and shot-noise variances computed via a similar set of manipulations, we have the result cited in equation (4.18):

$$\begin{aligned} \text{var}_{p'p'}(r) \approx & \frac{\pi e^2 G^{2+x} \eta}{2 h \nu_o} \left( \frac{k a_r}{L} \right)^2 \frac{P_T \rho_T^2}{a_L^2} \rho \left( \frac{1}{2} c T \right) B^3 / c^2 \times \\ & (-r) \left[ \Phi \left\{ (r + R_T) / \frac{1}{2} c T \right\} - \Phi \left\{ r / \frac{1}{2} c T \right\} \right] \\ & + 2 \left( \frac{e G \eta}{h \nu_o} \right)^2 \left( \frac{k a_r}{L} \right)^4 \left( \frac{P_T \rho_T^2}{a_L^2} \right)^2 \rho^2 \left( \frac{1}{2} c T \right)^2 T B_1^3 / c^2 \times \\ & (-r)^2 \left[ \Phi \left\{ (r + R_T) / \frac{1}{2} c T \right\} - \Phi \left\{ r / \frac{1}{2} c T \right\} \right]^2 \\ & + 2\sqrt{\pi} \frac{2k_B T_L}{R_L} \frac{B^3}{c^2} . \end{aligned} \quad (\text{B.23})$$



# Appendix C

Chapter 5 laid the ground work for the formulation of the heterodyne detector output signal  $\mathbf{r}(t)$  covariance. Assuming the limiting case of high local oscillator power, the covariance of  $\mathbf{r}(t)$  was separated into independent contributions from the shot-noise  $\mathbf{n}(t)$  covariance and the return signal  $\mathbf{y}(t)$  covariance. Compared with the return signal, the shot-noise  $\mathbf{n}(t)$  was modelled as a relatively uncomplicated white noise random process and was easily handled in the analysis. It is the goal of this appendix to investigate the much more complicated return covariance,  $\langle \mathbf{y}(u) \mathbf{y}^*(v) \rangle$ , in order to complete the mean and covariance calculations.

At the heart of these calculations is the assumption that the *statistical* behavior of the return signal can be broken down into two largely independent factors corresponding to physical processes which take place over relatively short- and long-term time scales, respectively. These notions will be formalized mathematically by adopting the Schell approximation [40] during the following calculations.

## C.1 Heterodyne Signal Correlation

In this section we detail the assumptions and modelling behind the computation of the return signal correlation. To begin, we restate the return signal covariance expression

derived in chapter 5:

$$\langle \mathbf{y}(u) \mathbf{y}^*(v) \rangle = \int d\vec{\rho} \int d\vec{\rho}' P_T \xi_P^2(\vec{\rho}) [\xi_P^*(\vec{\rho}')]^2 \langle \mathbf{T}(\vec{\rho}, u) \mathbf{T}^*(\vec{\rho}', v) \rangle \quad (\text{C.1})$$

where  $\mathbf{y}(\cdot)$  is the complex target return heterodyne component,  $P_T$  is the transmitter power,  $\xi_P(\cdot)$  is the Gaussian beam complex spatial mode striking the target and  $\mathbf{T}(\cdot, \cdot)$  is the effective target reflectivity projected on to the  $T$ -plane.

As justified in Appendix B §1, we will break apart this double-integral into a sum and difference formulation which exploits the rapid spatial decorrelation of the return phase. Therefore, we reformulate the above integral expression in our standard sum and difference coordinate system:

$$\begin{aligned} \vec{\rho}_+ &= \frac{1}{2}(\vec{\rho} + \vec{\rho}') \\ \vec{\rho}_- &= \vec{\rho} - \vec{\rho}'. \end{aligned}$$

Applying this change of variables, we have

$$\begin{aligned} \langle \mathbf{y}(u) \mathbf{y}^*(v) \rangle &\approx \\ &\int d\vec{\rho}_+ \int d\vec{\rho}_- P_T \left[ \frac{1}{\pi a_L^2} \exp \left\{ \frac{-|\vec{\rho}_+|^2}{a_L^2} \right\} \right]^2 \rho(\vec{\rho}_+, \frac{1}{2}(u+v)) \exp \left\{ \frac{-2|\vec{\rho}_+|^2}{a_T^2} \right\} \\ &\exp \left\{ \frac{2jk\vec{\rho}_+ \cdot \vec{\rho}_-}{R_T} \right\} \exp \left\{ \frac{-|\vec{\rho}_- + iR_T\Omega(t-u)|^2}{\rho_T^2} \right\} \end{aligned} \quad (\text{C.2})$$

where the approximation sign comes about because we have made the following assumptions in addition to coordinate transformation:

- As in the RTI Fraunhofer return calculation, individual returns from  $\approx \rho_T$ -sized surface patches only exhibit significant correlation during patch overlap, and otherwise, make negligible contributions to the double-integral. Therefore, under this condition, we have  $\vec{\rho} \approx \vec{\rho}'$  which leads to  $|\vec{\rho}|^2 + |\vec{\rho}'|^2 \approx \frac{1}{2}|\vec{\rho} + \vec{\rho}'|^2 = 2|\vec{\rho}_+|^2$ .



- Again, in the case of neighboring patches, the size of the regions over which non-negligible contributions are made is on the order of the surface roughness correlation length,  $\rho_T$ . Since the value of this parameter is rather small, on the order of a few wavelengths or so, we will assume that the target reflectivity varies slowly over the patch extent, so that  $\sqrt{\rho(\vec{\rho}, u)} \approx \sqrt{\rho(\vec{\rho}', v)}$ , which gives:

$$\sqrt{\rho(\vec{\rho}, u)}\sqrt{\rho(\vec{\rho}', v)} \approx \rho(\vec{\rho}_+, \frac{1}{2}(u + v)).$$

Since we are interested in investigating the speckle decorrelation behavior, let us adopt the following time coordinates:

$$u = t + \frac{1}{2}\tau \quad (\text{C.3})$$

$$v = t - \frac{1}{2}\tau. \quad (\text{C.4})$$

The dummy time variable  $t$  accounts for the particular target aspect presented to the laser radar during the observation time, while the time variable  $\tau$  will be used to characterize the fast signal variations within the observation dwell time  $T$ . Thus, we have

$$\begin{aligned} & \langle \mathbf{y}(t + \frac{1}{2}\tau) \mathbf{y}^*(t - \frac{1}{2}\tau) \rangle \\ &= \int d\vec{\rho}_+ \frac{P_T}{\pi^2 a_L^4} \rho(\vec{\rho}_+, t) \exp \left\{ \frac{-2|\vec{\rho}_+|^2}{a_T^2} \right\} \underbrace{\exp \left\{ \frac{-2|\vec{\rho}_+|^2}{a_L^2} \right\}}_{\approx 1} \\ & \int d\vec{\rho}_- \exp \left\{ \frac{2j\mathbf{k}\vec{\rho}_+ \cdot \vec{\rho}_-}{R_T} \right\} \exp \left\{ \frac{-|\vec{\rho}_- + \vec{v}R_T\Omega(t - u)|^2}{\rho_T^2} \right\}. \quad (\text{C.5}) \end{aligned}$$

We model spotlight-mode target illumination by assuming the last Gaussian term on the second line is unity over the support of the transversely projected reflectance. This action builds uniform target illumination into the model. Evaluating the second

integral, which the reader will recognize as a two-dimensional Fourier transform with respect to the variable  $\vec{\rho}_-$ , gives the final form of the heterodyne signal correlation,

$$\begin{aligned} \langle \mathbf{y}(t + \frac{1}{2}\tau) \mathbf{y}^*(t - \frac{1}{2}\tau) \rangle = \\ \int d\vec{\rho}_+ \frac{P_T \rho_T^2}{\pi a_T^4} \rho(\vec{\rho}_+, t) \exp\{2jk\Omega \rho_{x+} \tau\} \exp\left\{-\left(\frac{2}{a_T^2} + \frac{k^2 \rho_T^2}{R_T^2}\right) |\vec{\rho}_+|^2\right\}. \end{aligned} \quad (\text{C.6})$$

The above correlation result can be used to back out the speckle coherence time for a uniform featureless spherical target of arbitrary reflectivity. If we define the speckle coherence time to be  $\tau_{\text{coh}}$  such that

$$\frac{\langle \mathbf{y}(t + \frac{1}{2}\tau_{\text{coh}}) \mathbf{y}^*(t - \frac{1}{2}\tau_{\text{coh}}) \rangle}{\langle \mathbf{y}(t) \mathbf{y}^*(t) \rangle} = e^{-1},$$

then the coherence time  $\tau_{\text{coh}}$  becomes

$$\tau_{\text{coh}} = \frac{\sqrt{2}}{k\Omega} \sqrt{\frac{2}{a_T^2} + \frac{k^2 \rho_T^2}{R_T^2}} \quad (\text{C.7})$$

If we assume that the edge of the projected surface reflectance is modelled by the support of such projections in the  $\mathcal{T}$ -plane rather than the Gaussian fall off modelled by the  $\exp\{-|\vec{\rho}|^2/a_T^2\}$  term in the target model, we obtain the following  $\tau_{\text{coh}}$  formula by taking  $a_T \rightarrow \infty$ ,

$$\tau_{\text{coh}} = \sqrt{2} \frac{\rho_T}{\Omega R_T} \quad (\text{C.8})$$

and assuming  $\rho_T \approx \lambda$ .

This result is identical to the speckle coherence time in the RTI scenario (see Appendix B §2.1). Therefore, we conclude that DTI projections are statistically independent if the dwell time  $T$  is smaller than the inter-projection sampling period,  $2\pi/N\Omega$ , by several speckle coherence times (see §3).

## C.2 DTI Projection First Moment Derivation

In this section we will continue our analysis and derive the first moment of the DTI projection by building upon the concepts introduced in the last section. We begin by restating the contribution to the projection mean due to the received signal  $\mathbf{y}(t)$  component as cited in equation (5.8):

$$\begin{aligned} \langle p_{\theta_n}(\nu) \rangle_y = & \\ & \sqrt{\frac{8}{\pi T^2}} \int_{-\infty}^{\infty} du \int_{-\infty}^{\infty} dv \langle \mathbf{y}(u) \mathbf{y}^*(v) \rangle e^{-2\pi j\nu(u-v)} e^{-4((u-t_n)^2+(v-t_n)^2)/T^2} \end{aligned} \quad (\text{C.9})$$

where the variables  $u$  and  $v$  on the right-hand-side are dummy time arguments, the expectation on the left-hand-side is taken with respect to the random process  $\mathbf{y}$ , and the projection angle  $\theta_n$  corresponds to the projection taken during the observation dwell time  $T$  centered on the sampling instant  $t_n$ .

The discussion in chapter 5 suggested that the heterodyne signal correlation can be written in the form

$$\langle \mathbf{y}(u) \mathbf{y}^*(v) \rangle = K\left(\frac{1}{2}(u+v), u-v\right) \approx \text{var}\left(\frac{1}{2}(u+v)\right) \cdot k(u-v)$$

which is called the Schell approximation in the literature [40]. The time sum variable accounts for the slow evolution of target aspect throughout the rotation period while the time difference variable indexes the stationary speckle randomness over a sufficiently short interval. Adopting a sum and difference time coordinate system in our usual manner,

$$u = t + \frac{1}{2}\tau \quad (\text{C.10})$$

$$v = t - \frac{1}{2}\tau, \quad (\text{C.11})$$

we write

$$\langle \mathbf{y}(t + \frac{1}{2}) \mathbf{y}^*(t - \frac{1}{2}) \rangle = K(t, \tau). \quad (\text{C.12})$$

Therefore, using the covariance result derived in the previous section, the Fourier transform of  $K(t, \tau)$  with respect to  $\tau$  is the power spectrum of the heterodyne signal component at time indexed by the dummy variable  $t$  [40, 41]:

$$\begin{aligned}
\mathcal{S}(t, f) &\equiv \int_{-\infty}^{+\infty} d\tau K(t, \tau) e^{-2\pi j f \tau} \\
&= \int_{-\infty}^{+\infty} d\tau \langle \mathbf{y}(t + \frac{1}{2}\tau) \mathbf{y}^*(t - \frac{1}{2}\tau) \rangle e^{-2\pi j f \tau} \\
&= \frac{P_T \rho_T^2}{\pi a_L^4} \int_{R^2} d\vec{\rho}_+ \rho(\vec{\rho}_+, t) \exp \left\{ - \left( \frac{2}{a_T^2} + \frac{k^2 \rho_T^2}{R_R^2} \right) |\vec{\rho}_+|^2 \right\} \\
&\quad \int_{-\infty}^{+\infty} d\tau \exp \{ 2jk\Omega \rho_{z_+} \tau \} \exp \{ -2\pi j f \tau \} \\
&= \frac{P_T \rho_T^2}{\pi a_L^4} \int_{R^2} d\vec{\rho}_+ \rho(\vec{\rho}_+, t) \exp \left\{ - \left( \frac{2}{a_T^2} + \frac{k^2 \rho_T^2}{R_R^2} \right) |\vec{\rho}_+|^2 \right\} \delta \left( f - \frac{2\Omega}{\lambda} \rho_{z_+} \right) \\
&= \frac{P_T \lambda \rho_T^2}{2\pi \Omega a_L^4} \int_{-\infty}^{+\infty} d\rho_{z_+} \rho \left( \left( \frac{\lambda}{2\Omega} f, \rho_{z_+} \right), t \right) \underbrace{\exp \left\{ - \left( \rho_{z_+}^2 + \left( \frac{\lambda}{2\Omega} f \right)^2 \right) / b^2 \right\}}_{\substack{\text{Two-Dimensional} \\ \text{Gaussian Window Function}}} \tag{C.13} \\
&\tag{5.11}
\end{aligned}$$

where we have defined

$$b^2 = \frac{1}{\frac{2}{a_T^2} + \frac{k^2 \rho_T^2}{R_R^2}}. \tag{C.14}$$

Thus, for a fixed Doppler frequency  $f$ , which corresponds to a cross-range displacement of  $r = \lambda f / 2\Omega$  meters, the power spectrum is proportional to a line-integral along the  $\rho_{z_+}$ -axis. This formulation is a generalized Radon transform [27, §II.7] indexed by the Doppler frequency. The integrand for the Radon transform is the surface reflectivity transversely projected at time  $t$  onto the  $\mathcal{T}$ -plane and weighted with the same Gaussian metric discovered during the RTI analysis which models surface roughness-aspect angle roll-off.

Thus, expressing the mean projection in the  $(t, \tau)$  sum and difference time coor-

dinates

$$\begin{aligned}
\langle p_{\theta}(\nu) \rangle_y &= \sqrt{\frac{8}{\pi T^2}} \int_{-\infty}^{\infty} dt \int_{-\infty}^{\infty} d\tau K(t, \tau) e^{-2\pi j\nu\tau} e^{-8(t-t_n)^2/T^2} e^{-2\tau^2/T^2} \\
&= \sqrt{\frac{8}{\pi T^2}} \int_{-\infty}^{\infty} dt \int_{-\infty}^{\infty} d\tau \underbrace{\int_{-\infty}^{+\infty} df S(t, f) e^{2\pi jf\tau}}_{= K(t, \tau)} e^{-2\pi j\nu\tau} e^{-8(t-t_n)^2/T^2} e^{-2\tau^2/T^2} \\
&= \sqrt{\frac{8}{\pi T^2}} \int_{-\infty}^{+\infty} df \int_{-\infty}^{\infty} dt S(t, f) e^{-8(t-t_n)^2/T^2} \int_{-\infty}^{\infty} d\tau e^{2\pi j(f-\nu)\tau} e^{-2\tau^2/T^2} \\
&= 2 \int_{-\infty}^{+\infty} df e^{-\pi^2 T^2 (f-\nu)^2/2} \underbrace{\int_{-\infty}^{\infty} dt S(t, f) e^{-8(t-t_n)^2/T^2}}_{\approx S(t_n, f) \int_{-\infty}^{\infty} dt e^{-8t^2/T^2}} \\
&\approx \sqrt{\frac{\pi T^2}{2}} \int_{-\infty}^{+\infty} df S(t_n, f) \exp\left\{-\frac{1}{2}(f-\nu)^2 \Big/ \frac{1}{\pi^2 T^2}\right\} \tag{C.15}
\end{aligned}$$

where the final step the last integral was evaluated by applying the Schell approximation, i.e., assuming that  $S(t, f)$  varies slowly with respect to  $t$  about the dwell time centered on sampling instant  $t_n$ .

Completing the calculation by substituting (C.13) for  $S(t_n, f)$  and rewriting the above integral as a convolution, we have the final form of the mean projection (equation 5.13):

$$\begin{aligned}
\langle p_{\theta_n}(\nu) \rangle_y \Big|_{\nu=2r\Omega/\lambda} &= \left[ \sqrt{\pi T^2/2} \exp\left\{-\frac{1}{2}r^2 \Big/ \frac{1}{k^2 \Omega^2 T^2}\right\} \right] \star \\
&\quad \left[ \frac{P_T \rho_T^2}{\pi a_L^4} \int_{-\infty}^{\infty} d\rho_z \rho_{t_n}(r, \rho_z) \exp\{-(\rho_z^2 + r^2)/b^2\} \right]. \tag{C.16}
\end{aligned}$$

### C.3 DTI Second Moment Projection Derivations

In this section we will calculate the projection covariance for the DTI imaging system assuming a low-contrast target reflectivity model and super-resolution conditions. The following subsection details the calculation of the projection covariance. This result is used in the second subsection to derive the filtered projection variance under identical assumptions.

Before proceeding with these computations, we will use the results of the previous section to demonstrate inter-projection statistical independence. This will be accomplished by showing that the sum of a typical dwell time  $T$  and speckle coherence time is much shorter than the inter-projection sampling period. The upper bound for  $T$  under permissible smearing conditions is found by setting the cross-range resolution cell dimension equal to the maximum target surface travel during the dwell time. This gives the relation  $T \ll 1/\sqrt{kR_T}\Omega$  for minimal smearing during projection measurement. Therefore, the sum of both the maximum dwell and speckle coherence times gives:

$$\frac{1}{\sqrt{kR_T}\Omega} + \sqrt{2} \frac{\rho_T}{R_T\Omega}. \quad (\text{C.17})$$

At infrared and visible wavelengths where  $\lambda \approx \rho_T$  and  $R_T$  is on the order of meters, this quantity is always smaller than the inter-projection sampling interval,  $2\pi/N\Omega$ , except in cases where thousands of projections are required.

In practical systems, projections will number less than approximately 100, and thus, we will assume negligible inter-projection correlation. Therefore, the variance between any two points along each projection is all that is required to compute the reconstructed image variance.

### C.3.1 Projection Covariance

We begin by defining the projection covariance between the two points corresponding to the Doppler frequencies  $f$  and  $g$  along a DTI projection as  $\langle [|\mathbf{L}(f)|^2 - \langle |\mathbf{L}(f)|^2 \rangle] \cdot [|\mathbf{L}(g)|^2 - \langle |\mathbf{L}(g)|^2 \rangle] \rangle = K_{pp}(f, g)$ . Since the heterodyne signal  $\mathbf{y}$  is a circulo-complex Gaussian random process, the application of complex Gaussian moment factoring results in:

$$K_{pp}(f, g) = \langle \mathbf{L}(f) \mathbf{L}^*(f) \mathbf{L}(g) \mathbf{L}^*(g) \rangle - \langle p(f) \rangle \langle p(g) \rangle \quad (\text{C.18})$$

$$\begin{aligned} &= \langle \mathbf{L}(f) \mathbf{L}^*(g) \rangle \langle \mathbf{L}^*(f) \mathbf{L}(g) \rangle + \\ &\quad \underbrace{\langle \mathbf{L}(f) \mathbf{L}^*(f) \rangle}_{\text{Becomes } \langle p(f) \rangle} \underbrace{\langle \mathbf{L}^*(g) \mathbf{L}(g) \rangle}_{\text{Becomes } \langle p(g) \rangle} + \\ &\quad \underbrace{\langle \mathbf{L}(f) \mathbf{L}(g) \rangle}_{=0} \underbrace{\langle \mathbf{L}^*(f) \mathbf{L}^*(g) \rangle}_{=0} - \langle p(f) \rangle \langle p(g) \rangle \quad (\text{C.19}) \end{aligned}$$

$$= \left| \langle \mathbf{L}(f) \mathbf{L}^*(g) \rangle \right|^2 \quad (\text{C.20})$$

where moment factoring was used to expand equation (C.18) into (C.19), which after simplification, gives the final result of (C.20).

At this point, it is helpful to recall that  $\mathbf{L}(\cdot)$  ultimately represents contributions from local oscillator shot-noise  $\mathbf{n}$  and speckle induced phase variations in the received signal  $\mathbf{y}$ . Since the heterodyne detector model presents these two random processes as statistically independent in the high local oscillator power regime, we may now write the expectation within the above magnitude-squared expression as

$$\begin{aligned} \langle \mathbf{L}(f) \mathbf{L}^*(g) \rangle &= \\ &\underbrace{\int_{-\infty}^{+\infty} du \int_{-\infty}^{+\infty} dv \langle \mathbf{y}(u) \mathbf{y}^*(v) \rangle e^{-2\pi jfu} e^{+2\pi jgv} \left( \frac{8}{\pi T^2} \right)^{1/2} e^{-4(u-t_n)^2/T^2} e^{-4(v-t_n)^2/T^2}}_{\equiv I_1(f, g)} + \end{aligned}$$

$$\underbrace{\int_{-\infty}^{+\infty} du \int_{-\infty}^{+\infty} dv \langle \mathbf{n}(u) \mathbf{n}^*(v) \rangle e^{-2\pi j f u} e^{+2\pi j g v} \left( \frac{8}{\pi T^2} \right)^{1/2} e^{-4(u-t_n)^2/T^2} e^{-4(v-t_n)^2/T^2}}_{\equiv I_2(f, g)}$$

where the covariance of this  $n^{\text{th}}$  projection is calculated for a projection dwell time centered on the instant  $t_n$ . Note that we have defined for the sake of future convenience the first term in the above expansion as  $I_1(f, g)$  and the second term as  $I_2(f, g)$ . Since  $\mathbf{n}(u)$  is a white noise process, we can immediately write the result:

$$I_2(f, g) = \frac{h\nu_o}{\eta} \exp \left\{ -\frac{1}{2} (f - g)^2 \left/ \frac{4}{\pi^2 T^2} \right. \right\} \exp \{ -2\pi j (f - g) t_n \}. \quad (\text{C.21})$$

As with previous calculations involving the covariance of the received signal  $\mathbf{y}(u)$ , we begin by taking expectations after converting to sum and difference time and frequency coordinate systems in order to separate the short- and long-term statistical behavior of the target return. Using the following transformations

$$t = \frac{1}{2}(u + v)$$

$$\tau = u - v$$

$$f_+ = \frac{1}{2}(f + g)$$

$$f_- = f - g.$$

to convert the expression for  $I_1(f, g)$  into an equivalent quantity denoted as  $I'_1(f_+, f_-)$ , we have:

$$\begin{aligned} I'_1(f_+, f_-) &= \int_{-\infty}^{+\infty} dt \int_{-\infty}^{+\infty} d\tau \underbrace{\int_{-\infty}^{+\infty} df' \mathcal{S}(t, f') e^{+2\pi j f' \tau}}_{= K(t, \tau)} \\ &\exp \left\{ -2\pi j \left[ (t + \frac{1}{2}\tau)(f_+ + \frac{1}{2}f_-) - (t - \frac{1}{2}\tau)(f_+ - \frac{1}{2}f_-) \right] \right\} \\ &\left( \frac{8}{\pi T^2} \right)^{1/2} e^{-4(t-t_n+\tau/2)^2/T^2} e^{-4(t-t_n-\tau/2)^2/T^2} \end{aligned} \quad (\text{C.22})$$



where we have formulated the covariance of the received signal  $\langle \mathbf{y}(u)\mathbf{y}^*(v) \rangle$  in sum and difference time coordinates and expressed this quantity,  $K(t, \tau)$ , in terms of the single-dimensional *inverse* Fourier transform of the power spectrum  $S(t, f')$  with respect to  $f'$ , the differential time-scale frequency. Cancelling common terms, exchanging the order of integration and evaluating the resulting integral with respect to the differential time coordinate  $\tau$ , we write:

$$\begin{aligned}
I'_1(f_+, f_-) &= \left(\frac{8}{\pi T^2}\right)^{1/2} \int_{-\infty}^{+\infty} dt \int_{-\infty}^{+\infty} d\tau \int_{-\infty}^{+\infty} df' S(t, f') e^{+2\pi j f' \tau} \\
&\quad \exp\{-2\pi j(f_+ \tau + f_- t)\} e^{-8(t-t_n)^2/T^2} e^{-2\tau^2/T^2} \\
&= \left(\frac{8}{\pi T^2}\right)^{1/2} \int_{-\infty}^{+\infty} df' \int_{-\infty}^{+\infty} dt S(t, f') e^{-2\pi j f_- t} e^{-8(t-t_n)^2/T^2} \\
&\quad \int_{-\infty}^{+\infty} d\tau e^{-2\pi j(f_+ - f')\tau} e^{-2\tau^2/T^2} \\
&= 2 \int_{-\infty}^{+\infty} df' \exp\left\{-\frac{1}{2}(f_+ - f')^2 \Big/ \frac{1}{\pi^2 T^2}\right\} \\
&\quad \underbrace{\int_{-\infty}^{+\infty} dt S(t, f') e^{-8(t-t_n)^2/T^2} e^{-2\pi j f_- t}}_{\approx S(t_n, f') \int_{-\infty}^{+\infty} dt e^{-8t^2/T^2} e^{-2\pi j f_-(t+t_n)}} \quad (C.23)
\end{aligned}$$

where again in the final line, we introduce the assumption that observation dwell time is sufficiently long to provide super-resolution. Evaluating the integral with respect to  $t$  results in the following expression:

$$\begin{aligned}
I'_1(f_+, f_-) &= \sqrt{\frac{\pi T^2}{2}} \exp\left\{-\frac{1}{2} f_-^2 \Big/ \frac{4}{\pi^2 T^2}\right\} \exp\{-2\pi j(f - g)t_n\} \\
&\quad \underbrace{\int_{-\infty}^{+\infty} df' S(t_n, f') \exp\left\{-\frac{1}{2}(f_+ - f')^2 \Big/ \frac{1}{\pi^2 T^2}\right\}}_{\text{Convolution Integral}}. \quad (C.24)
\end{aligned}$$

Except for the presence of the exponential and complex phase factors, the above result is identical in form to equation (C.15) preceding the final projection mean description.

Beginning with the expression for  $S(t, f')$ , equation (C.13), the power spectrum was calculated for a low-contrast target with an overall reflectivity of  $\rho(x, y, z) = \rho$ , giving:

$$S(t_n, f') = \frac{P_T \rho_T^2 b}{\sqrt{\pi} a_L^4} \rho \frac{\lambda}{2\Omega} \exp \left\{ -\frac{1}{2} \left( \frac{\lambda}{2\Omega} \right)^2 (f')^2 / b^2 \right\}. \quad (\text{C.25})$$

Substituting this result into equation (C.24), we have:

$$\begin{aligned} I_1(f_+, f_-) &= \frac{P_T \rho_T^2 b^2}{\sqrt{2\pi} a_L^4} \rho \frac{\lambda/2\Omega}{\sigma} \exp \{-2\pi j(f - g)t_n\} \\ &\quad \exp \left\{ -\frac{1}{2} f_-^2 / \frac{4}{\pi^2 T^2} \right\} \exp \left\{ -\frac{1}{2} \left( \frac{\lambda}{2\Omega} \right)^2 f_+^2 / \sigma^2 \right\} \end{aligned} \quad (\text{C.26})$$

where we have defined

$$\sigma^2 = \frac{b^2}{2} + \frac{1}{k^2 \Omega^2 T^2}. \quad (\text{C.27})$$

The parameter  $\sigma$  in some sense accounts for the *apparent* physical size of the target as seen by the laser radar after taking into consideration the effects of surface roughness—aspect angle and smearing due to finite dwell time  $T$ .

Therefore, the covariance of the random process  $\mathbf{L}$  is obtained by converting back to the original  $(f, g)$  coordinate system and summing both  $I_1$  and  $I_2$ :

$$\begin{aligned} \langle \mathbf{L}(f) \mathbf{L}^*(g) \rangle &= \\ &\quad \exp \left\{ -\frac{1}{2} (f - g)^2 / \frac{4}{\pi^2 T^2} \right\} \exp \{-2\pi j(f - g)t_n\} \times \\ &\quad \left[ \frac{h\nu_o}{\eta} + \frac{P_T \rho_T^2 b^2}{\sqrt{2\pi} a_L^4} \rho \frac{\lambda/2\Omega}{\sigma} \exp \left\{ -\frac{1}{2} \left( \frac{\lambda}{2\Omega} \right)^2 (f + g)^2 / 4\sigma^2 \right\} \right]. \end{aligned} \quad (\text{C.28})$$

Taking the magnitude-squared, we have the projection covariance:

$$\begin{aligned} K_{pp}(f, g) &= \exp \left\{ -(f - g)^2 / \frac{4}{\pi^2 T^2} \right\} \times \\ &\quad \left[ \frac{h\nu_o}{\eta} + \frac{P_T \rho_T^2 b^2}{\sqrt{2\pi} a_L^4} \rho \frac{\lambda/2\Omega}{\sigma} \exp \left\{ -\frac{1}{2} \left( \frac{\lambda}{2\Omega} \right)^2 (f + g)^2 / 4\sigma^2 \right\} \right]^2. \end{aligned} \quad (\text{C.29})$$

Recalling that the Doppler shift from the IF center frequency is directly related to the cross-range displacement via  $f = 2\Omega r/\lambda$ , we write the projection covariance in terms of the cross-range variables as:

$$\mathbf{K}_{pp}(r_2, r_1) = \exp \left\{ - (r_2 - r_1)^2 / \frac{4}{k^2 \Omega^2 T^2} \right\} \times$$

$$\left[ \underbrace{\frac{h\nu_o}{\eta}}_{\substack{\text{Shot} \\ \text{Noise} \\ \text{Term}}} + \underbrace{\frac{P_T \rho_T^2 b^2}{\sqrt{2\pi} a_L^4} \rho \frac{\lambda/2\Omega}{\sigma} \exp \left\{ -\frac{1}{2} (r_2 + r_1)^2 / 4\sigma^2 \right\}}_{\substack{\text{Target} \\ \text{Induced Speckle} \\ \text{Term}}} \right]^2. \quad (\text{C.30})$$

This equation (C.30) is the final projection covariance result cited in equation (5.14). Note that the covariance is the product of two factors. The first factor is a Gaussian term which describes the projection decorrelation. The projection decorrelation length,  $\sqrt{2}/k\Omega T$ , is directly proportional to the laser radar cross-range resolution. The second factor sums the relative contributions from local oscillator shot-noise and speckle resolved over the exposed face of the target. Note that this last term is directly proportional to transmission power,  $P_T$ , and nominal target reflectivity,  $\rho$ , a situation which indicates the presence of signal dependent noise.

### C.3.2 Filtered DTI Projection Variance

In this section we will compute the filtered DTI projection variance used to establish the filtered backprojection reconstruction SNR result. We begin with the observation that the above projection covariance is written in a range sum and difference formulation reminiscent of the companion RTI covariance. Under super-range resolution conditions, the analysis in §2.2 of Appendix B applies, if we make the following covariance separation specification,

$$\mathbf{k}_{pp}(r_-) = \exp \left\{ -r_-^2 / \frac{4}{k^2 \Omega^2 T^2} \right\}$$

$$\text{Var}_p(r_+) = \left[ \frac{h\nu_o}{\eta} + \frac{P_T \rho_T^2 b^2}{\sqrt{2\pi a_L^4}} \rho \frac{\lambda/2\Omega}{\sigma} \exp\left\{-\frac{1}{2} r_+^2 / \sigma^2\right\} \right]^2$$

which gives in the following result cited in equation (5.16):

$$\text{var}_{p'p'}(r) \approx \frac{k^2 \Omega^2 T^2}{8\pi^2} \text{var}_p(r). \quad (\text{C.31})$$

# Bibliography

- [1] M. I. Skolnik, "Fifty years of radar," *Proceedings of the IEEE*, vol. 73, pp. 182–197, February 1985.
- [2] M. I. Skolnik, ed., *Radar Handbook*. New York: McGraw-Hill Publishing Company, 2nd ed., 1990.
- [3] R. J. Doviak, D. S. Zrnić, and D. S. Sirmans, "Doppler weather radar," *Proceedings of the IEEE*, vol. 67, pp. 1522–1553, November 1979.
- [4] "FAA planning to deploy terminal weather radar," *Aviation Week and Space Technology*, vol. 120, pp. 64–65, January 2, 1984.
- [5] D. A. Boutacoff, "Backscatter radar extends early warning times," *Defense Electronics*, vol. 17, pp. 71–83, May 1985.
- [6] D. Hughes, "Maine OTH-B completes development tests; GE to transfer system to USAF," *Aviation Week and Space Technology*, vol. 132, pp. 52–53, April 9, 1990.
- [7] "Magellan's radar images of Venus to unmask cloud-shrouded planet," *Aviation Week and Space Technology*, vol. 131, pp. 113–115, October 9, 1989.
- [8] S. D. Wall, "Venus unveiled," *Astronomy*, vol. 17, pp. 26–32, April 1989.

- [9] R. M. Gagliardi and S. Karp, *Optical Communications*. New York: John Wiley and Sons, 1976.
- [10] J. H. Shapiro, B. A. Capron, and R. C. Harney, "Imaging and target detection with a heterodyne-reception optical radar," *Applied Optics*, vol. 20, pp. 3292-3313, 1981.
- [11] J. C. Dainty, ed., *Laser Speckle and Related Phenomena*. Vol. 9 of *Topics in Applied Physics*, New York: Springer-Verlag, 2nd ed., 1984. Chapter 2.
- [12] J. H. Shapiro, "Target-reflectivity theory for coherent laser radars," *Applied Optics*, vol. 21, pp. 3398-3407, September 15, 1982.
- [13] J. H. Shapiro, "Correlation scales of laser speckle in heterodyne detection," *Applied Optics*, vol. 24, pp. 1883-1888, June 15, 1985.
- [14] D. M. Papurt, J. H. Shapiro, and R. C. Harney, "Atmospheric propagation effects on coherent laser radars," *Proceedings of SPIE*, vol. 300, pp. 86-99, 1981.
- [15] D. M. Papurt, J. H. Shapiro, and S. T. Lau, "Measured turbulence and speckle effects in laser radar target returns," *Proceedings of SPIE*, vol. 415, pp. 166-178, 1983.
- [16] R. C. Harney and R. J. Hull, "Compact infrared radar technology," *Proc. Soc. Photo-Opt. Instrum. Eng.*, vol. 227, pp. 162-170, 1980.
- [17] M. B. Mark, "Multipixel, multidimensional laser radar system performance," Ph.D. thesis, Dept. of Elect. Engr. and Computer Sci., MIT, 1986.
- [18] M. B. Mark and J. H. Shapiro, "Multipixel, multidimensional laser radar system performance," *Proceedings of SPIE*, vol. 783, pp. 109-122, 1987.

- [19] S. M. Hannon, "Detection processing for multidimensional laser radars," Ph.D. thesis, Dept. of Elect. Engr. and Computer Sci., MIT, 1989.
- [20] D. L. Mensa, S. Halevy, and G. Wade, "Coherent Doppler tomography for microwave imaging," *Proceedings of the IEEE*, vol. 71, pp. 254–261, February 1983.
- [21] D. C. Munson, Jr., J. D. O'Brien, and W. K. Jenkins, "A tomographic formulation of spotlight-mode synthetic aperture radar," *Proceedings of the IEEE*, vol. 71, pp. 917–925, August 1983.
- [22] F. K. Knight, S. R. Kulkarni, R. M. Marino, and J. K. Parker, "Tomographic techniques applied to laser radar reflective measurements," *The Lincoln Laboratory Journal*, vol. 2, pp. 143–160, Summer 1989.
- [23] F. K. Knight, D. I. Klick, D. P. Ryan-Howard, J. R. Theriault, Jr., B. K. Tussey, and A. M. Bechman, "Two-dimensional tomographs using range measurements," *Proceedings of SPIE*, vol. 999, pp. 269–280, 1988.
- [24] R. M. Marino, "Tomographic image reconstructions from laser radar reflective projections," *Proceedings of SPIE*, vol. 999, pp. 248–268, 1988.
- [25] G. T. Herman, ed., *Image Reconstructions from Projections*. Vol. 32 of *Topics in Applied Physics*, New York: Springer-Verlag, 1979.
- [26] A. Macovski, *Medical Imaging Systems*. Englewood Cliffs, New Jersey: Prentice-Hall, Inc., 1983.
- [27] F. Natterer, *The Mathematics of Computerized Tomography*. New York: John Wiley and Sons, 1986.

- [28] D. Park, "High-Resolution Laser Radar Performance Analysis," Ph.D. thesis, Dept. of Elect. Engr. and Computer Sci., MIT, 1988.
- [29] J. W. Goodman, *Introduction to Fourier Optics*. New York: McGraw-Hill, 1968.
- [30] D. L. Fried, "Statistics of the laser radar cross section of a randomly rough target," *J. Opt. Soc. Am.*, no. 11, pp. 1150–1160, 1976.
- [31] J. C. Leader, "An analysis of the frequency spectrum of laser light scattered from moving rough objects," *J. Opt. Soc. Am.*, vol. 67, pp. 1091–1098, August 1977.
- [32] N. George, "Speckle from rough, moving objects," *J. Opt. Soc. Am.*, vol. 66, pp. 1182–1194, November 1976.
- [33] J. C. Erdmann and R. I. Gillert, "Speckle field of curved, rotating surfaces of gaussian roughness illuminated by a laser light spot," *J. Opt. Soc. Am.*, vol. 66, pp. 1194–1204, November 1976.
- [34] J. H. Shapiro, "Lecture Notes for 6.453 Optical Detection and Communication," M.I.T. Electrical Engineering and Computer Science Dept., Cambridge, Massachusetts, 1982.
- [35] P. Richardus and R. K. Adler, *Map Projections*. Amsterdam: North-Holland, 1972.
- [36] A. E. Siegman, "The antenna properties of optical heterodyne receivers," *Proc. IEEE*, vol. 54, p. 1350, 1966.
- [37] S. R. Kulkarni, A. S. Lele, and M. F. Reily, "Qualitative Differences Between Tomographic Reconstructions from Range-Resolved versus Doppler-Resolved



- Data," Project Memorandum No. 52PM-ODT-0042, M.I.T. Lincoln Laboratory, Lexington, Massachusetts, 1989.
- [38] A. L. Kachelmyer, "Range Doppler imaging: waveforms and receiver design," *Proceedings of SPIE*, vol. 999, pp. 138-161, 1988.
- [39] A. L. Kachelmyer, "Range-Doppler imaging with a laser radar," *The Lincoln Laboratory Journal*, vol. 3, no. 1, pp. 87-118, 1990.
- [40] A. C. Schell, "A technique for the determination of the radiation pattern of a partially coherent aperture," *IEEE Transactions on Antennas and Propagation*, vol. 15, pp. 187-188, 1967.
- [41] D. L. Snyder, J. A. O'Sullivan, and M. I. Miller, "The use of maximum likelihood estimation for forming images of diffuse radar targets from delay-Doppler data," *IEEE Transactions on Information Theory*, vol. 37, pp. 536-548, May 1989.

## Biographical Note

Bradley Thomas Binder was born in Yankton, South Dakota on April 6, 1960. In 1983 he graduated from the University of Nebraska with a B.S.E.E. degree with high distinction and was named a University Chancellor's Scholar. Entering the Dept. of Electrical Engineering and Computer Science at the Massachusetts Institute of Technology in 1984, he was supported by a National Science Foundation Graduate Fellowship in obtaining his S.M.E.E. and Electrical Engineer's degree in 1987 while a member of the Research Laboratory of Electronics. In the beginning of his graduate education in 1984, and finally in 1988, he was a Dept. Teaching Assistant before accepting an appointment as a Research Assistant with the Laser Radar Measurements Group at the M.I.T. Lincoln Laboratory. His research has appeared in the *IEEE Transactions on Communications*.

Mr. Binder is a staff member with the M.I.T. Lincoln Laboratory Battlefield Surveillance Group in Lexington, Massachusetts. He is engaged to Miss Joellen DiRusso of Dedham, Massachusetts.